

Formation mechanism and resistance fluctuations of atomic sized junctions

Inauguraldissertation

zur
Erlangung der Würde eines Doktors der Philosophie
vorgelegt der
Philosophisch-Naturwissenschaftlichen Fakultät
der Universität Basel

von

ZhengMing Wu Hawellek
aus Shanghai (China)



Basel, 2008

Genehmigt von der Philosophisch-Naturwissenschaftlichen Fakultät
auf Antrag von
Prof. Dr. Christian Schönenberger
Prof. Dr. Sense Jan van der Molen
Dr. Michel Calame

Basel, den 11. November 2008

Prof. Dr. Hans-Peter Hauri
Dekan

Contents

1	Introduction	1
1.1	Electron transport in small conductors	1
1.1.1	Typical length scales in conducting systems	1
1.1.2	Conductance of point-contact	3
1.1.3	Quantum Tunneling	8
1.2	Electromigration	10
1.2.1	Electron wind force	10
1.2.2	Essential parameters in electromigration	13
1.2.3	Electromigration in molecular electronics	15
1.3	Introduction to noise	17
1.3.1	Correlation function and spectral density of noise	17
1.3.2	Thermal noise	19
1.3.3	Generation and Recombination noise	20
1.3.4	1/ f -noise	20
2	Experimental techniques	25
2.1	Sample fabrication	25
2.2	Fabrication of nano-gaps and nano-junctions via electromigration	31
2.2.1	Principle of feedback controlled electromigration in four-terminal nano-junctions	32
2.2.2	Setup	32
2.2.3	Resistance evolution during electromigration	34
2.2.4	Controlling of the junction size with electromigration	36
2.2.5	Electromigration in Co junction	38
2.2.6	Conclusions	40

2.3	Temperature dependence of the junction resistivity	40
2.4	Noise measurement	42
2.4.1	Measurement setup	44
2.4.2	Setup calibration	45
3	Physical properties of nano-junctions	49
3.1	Temperature in nano-junctions during electromigration	49
3.1.1	Temperature in regime I	50
3.1.2	Temperature in regime II	51
3.1.3	Comparison of electromigration in two types of samples	53
3.1.4	Conclusions	56
3.2	Transition from classical to ballistic regime in nano-junctions	56
3.2.1	Evidence from the transport mechanism	56
3.2.2	The fast transition from regime I to regime II	58
3.2.3	I-V characteristics of formed gap	59
3.2.4	Conclusions	60
3.3	Scaling of $1/f$ noise in tunable break-junctions	61
3.3.1	Characteristics of the measured noise spectra	62
3.3.2	Transition from diffusive to ballistic transport regime	66
3.3.3	Hooge's constant α	68
3.3.4	Bulk origin of $1/f$ -noise in nano-contacts	69
3.3.5	Conclusion	70
4	Conclusions and outlook	71
A	Special electronic units for the measurement setup	83
A.1	Four-terminal feedback voltage source	83
A.2	Ground loop killer	84
A.3	Low noise voltage source	85
B	Mechanical controllable break junction	87
C	Complementary Experiments	89
C.1	Electromigration in scanning electron microscope (SEM)	89
C.2	Noise during electromigration	90
D	Parameters during electromigration	91
E	Histogram in log scale	93
	Publication List	95

Preamble

Within a classical length scale, i.e. from millimeter to kilometers, the electrical and mechanical properties of a piece of metal are not much different. The classical rules of physics are applicable in this large range of length scales. As soon as its size approaches the atomic scale, the classical knowledge about material properties becomes invalid. While in the macroscopic world, gold conduct 10 times better than lead; for conduction through a single atom, lead conduct better than gold by factor of three. Also the mechanical properties of a metal become unusual when atomic wires are formed. The development of micro-fabrication techniques in recent decades, such as optical lithography and electron beam lithography, provide the possibility to design and produce metallic structures in much smaller length scale. The invention of the scanning tunneling microscope (STM) in 1986 by Gerd Binnig and Heinrich Rohrer, together with other types of scanning probe techniques, provide the tools for manipulating and characterizing structures at the atomic and molecular scales. This has brought rapid progress in the field of mesoscopic physics, which is devoted to the study of electrical phenomena in small conductors for which the quantum nature of the electrons starts to play a role. In mesoscopic systems, the resistance does not necessarily depend on the length of the conducting wire as described by Ohm's law. A ballistic wire where electron backscattering is absent, still has a finite conductance $G_0 = 2e^2/h$. Whether electrons travel through a conducting wire diffusively or ballistically can be observed not only in conductance measurement, but also in other physical properties such as resistance or current fluctuation (noise). For example the shot noise, which is due to the randomness in the transmission of discrete charge quanta e from source to drain, is present in tunnel junctions but absent in macroscopic metallic wires. The reason is that the inelastic scattering of the electrons smears out the granularity

in the charge flow. There has been an intensive study of noise in metallic films, semiconductors, metallic oxides and inhomogeneous systems such as composites. In atomic point-contacts, two-level resistance fluctuations are observed and its noise spectrums are studied. But the noise behavior in a small conductor under the transition from diffusive to ballistic has not yet been reported.

The increasing attention paid to mesoscopic physics has been strongly encouraged by the ongoing miniaturization in the microelectronics industry. Since the first transistor was invented at Bell Labs by W. Shockley, J. Bardeen, and W. Brattain in December 1947, the miniaturization of semiconductor devices has followed "Moore's Law", which predicts a doubling of circuit density every 18 months. Under the limitation of optical lithography, the smallest size of components in production is 45 nm in 2007, and 32 nm expected in 2009. Further decrease in feature size requires the consideration of physics rules applicable at these length scales. However the dramatic increase in the unit price during scaling down demands new creative concepts. The emerging field of molecular electronics [1; 2] can be a solution to extend this limit. Molecular electronics aim at using molecules as building blocks in the construction of electronic circuits. The classical and quantum molecular transistor are two basic devices under study. The first can be considered as a scaling of a field effect transistor down to the nm-scale. The later, however, additionally makes use of quantum effects in its device operation. Molecules are small (\sim nm), cheap to synthesize, and able to self-assemble on a surface. Furthermore functionalized molecules (which are response to physical environment such as solvent, electrical potential, temperature, light) can be designed and synthesized. All these beneficial characteristics make molecules attractive. However contacting and electronically measuring molecules is a challenging task. There are various methods developed to define small metallic junctions with nano-sized gaps to anchor the molecules. Among these, electromigration induced nano-gaps have been employed for a broad range of molecules, revealing various transport phenomena. However the junction formation is a slow and instable process. The refined electromigration processes are therefore highly desirable.

The following thesis devotes to electromigration and $1/f$ noise behavior in nano-junctions in size from few hundred nanometers to single atomic contact. A successful technique to employ stable electromigration process in nano-junction and finally forming the nano-gap is presented.

This thesis

In this thesis we will focus on

(a) *Feedback controlled electromigration in four-terminal nano-junctions*, where a new technique to control electromigration in Au nano-junction is presented. The observation during electromigration in nano-junction is discussed.

(b) *Scaling of $1/f$ noise in tunable break-junctions*, where $1/f$ voltage noise of gold nano-contacts formed by electromigration and mechanically controlled break-junctions is studied. The voltage noise is measured for resistance value of the nano-contacts from 10Ω (many channels) to $10 \text{ k}\Omega$ (single atom contact).

This thesis is structured as follows:

- Chapter 1 gives a brief review about the conductance of metal in diffusive, ballistic and quantum regimes. The theory background of electromigration and its driving force is introduced. As the basics to understand noise measurements, we discuss two types of noise, i.e. thermal noise and $1/f$ noise, which we measured in our experiment. The mathematic basis for noise analysis is given as well.
- In Chapter 2 we describe first the general sample fabrication methods and processes. As an important technical basis in our experiments, we presents our new technique of feedback controlled electromigration in detail. The setup to perform electromigration and its calibration is described as well. For noise measurements we explain the procedure and setup for noise measurement. The important step of setup calibration is discussed in depth.
- In Chapter 3 we discuss the physical aspects more in depth in nano-junction during the narrowing of the junction cross-section by electromigration. We show the results of noise measurement in electromigrated and mechanically controlled break-junctions. The transition from diffusive to ballistic regime in nano-junction is observed during electromigration and proved by the noise measurement.
- Chapter 4 summarizes this thesis. The ideas and possibilities to explore further experiments based on our current experience are suggested.

Chapter 1

Introduction

1.1 Electron transport in small conductors

The size and geometry can have a strong influence and impact on the electron transport in ‘small’ sample. By comparing the dimensions of the conductor with some typical length scales in electron transport, we can divide the transport mechanisms into diffusive, ballistic and quantum regimes. Following we give a brief overview of various characteristic lengths in conducting systems and the conductance of a constriction in the conductor for those regimes. We define l , the smallest extension of sample, as the typical length scale of the system, on which the relevant processes in this conductor take place.

1.1.1 Typical length scales in conducting systems

In a conducting system one can identify different transport regimes according to how the size of the system is relative to various length scales. A conductor is diffusive if l is much larger than its mean free path. The mean free path L_m is the distance that an electron travels before its initial momentum is destroyed. It is defined as $L_m = v_F \times \tau_m$, where v_F is the Fermi velocity and τ_m is the momentum relaxation time. τ_m is related to the collision time τ_c in the form

$$\frac{1}{\tau_m} \rightarrow \frac{1}{\tau_c} \alpha_m$$

where the factor α_m has the value between 0 and 1 denoting the ‘effectiveness’ of an individual collision in destroying momentum. In a diffusive

conductor electrons incident to the transport channel are scattered at impurities or the wall. Electrons move in the conduction in a random walk manner with an average step size L_m (Figure 1.1a). L_m is around 50 nm in Au at 25°C. When the size l of a conductor reduced to be smaller than its elastic mean free path L_m , it enters ballistic regime. Electrons pass through the conductor with only scattering on the boundary of the conductor.(Figure 1.1b). The wave character of electrons becomes essential for electronic transport process, when the size l of a conductor is similar to electron Fermi wavelength λ_F , which is the de Broglie wavelength of electrons at fermi energy, i.e. $\lambda_F = h/\sqrt{2mE_F}$. The Fermi wavelength is about 35 nm for an electron density of $5 \times 10^{11}/cm^2$. At low temperatures the current is mainly carried by electrons with energy close to the Fermi energy. Electron transport in such conductor has to be treated quantum mechanically.

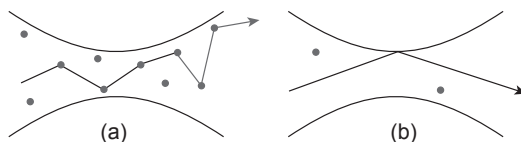


Figure 1.1: Schematic illustration of a diffusive (a) and ballistic (b) conductor.

If the size of the conductor l is smaller than its phase relaxation length, the conductor enters into mesoscopic regime. The phase-relaxation length L_ϕ is the distance that an electron travels before its initial phase is destroyed. It is defined as $L_\phi = v_F * \tau_\phi$. During elastic scattering with static scatters the phase of electron wave is conserved, $\tau_\phi \rightarrow \infty$. Inelastic scattering such as electron-electron and electron-phonon interaction, also the scattering with the impurities having internal degree of freedom can randomize the phase of the electron wave. L_ϕ can be indirectly measured from weak localization experiments [3; 4]. It is around 1 μm for Au at around $T=1$ K [5].

A conductor is ohmic if l much larger than each of three characteristic length scales: (1) Fermi wave length λ_F (2) the mean free path L_m (3) the phase-relaxation length L_ϕ [4]. An ohmic conductor is characterized by Ohm's law. The conductance G of a given sample is proportional to area A orthogonal to the current direction and inverse proportional to its length L :

$$G = \frac{A}{\rho L} \quad (1.1)$$

where ρ is the local resistivity.

The simplest conductor is the point-contact. The point-contact is a constriction in a conducting medium. Electrons can pass through the point-contact diffusively, ballistically or quantum mechanically depends on the radius of the constriction. The point-contact is diffusive /ballistic /quantum when its radius is much larger than L_m /smaller than L_m /similar to λ_F . The electron transport through point-contact is best treated differently in these three regimes. The conductance of point-contact will be discussed in detail in next section.

1.1.2 Conductance of point-contact

Maxwell conductance: diffusive point-contact

The conductance of a point-contact in the diffusive regime can be calculated using the classical conductivity tensor (homogeneous local conductivity tensor). In the case of a hyperbolic constriction, this can be done analytically [6]. As a function of a and η_0 this gives the conductance ($G_M = I/V_0$) of the constriction as:

$$G_M = (2a/\rho)(1 - \sin(\eta_0)) \quad (1.2)$$

where $2a$ is the distance between the foci of ellipsoid, the surface of the constriction is defined by $\eta_0 = \text{const}$. In the limiting case of $\eta_0 = 0$ the contact is an orifice of radius a in a non-conducting plate separating two metallic half-spaces, its conductance is $G_M = 2a/\rho$, where ρ is the resistivity in the infinite plane. We insert the Drude resistivity $\rho = mv_F/ne^2L_m$ to rewrite $G_M = (2e^2/h)(K_F^2a)(2l/3\pi^2)$. It has a similar form as Sharvin's resistance derived from the quantum mechanical approach in next section. Maxwell conductance has its classical limit, for ballistic point-contact we describe a quantum mechanical analyze below.

Sharvin conductance: ballistic point-contact

When the dimensions of a contact are much smaller than the electron ballistic mean free path L_m , an electron approaching the contact is either scattered back from the boundary of the point-contact or transmit through the contact opening directly ('ballistically') (see Figure 1.2a). The conductance of such a constriction was first calculated by Sharvin [7], who used an electron analogue to the flow of a dilute gas through a small hole. The conductance can be expressed by assuming a simple orifice-like point-contact geometry, see Figure 1.2b. Due to the ballistic motion at the point-contact a right-moving electron can only come from the left-hand-side and a left-moving one only from the right-half-space. Thus $k_z > 0$, ($k_z < 0$) states

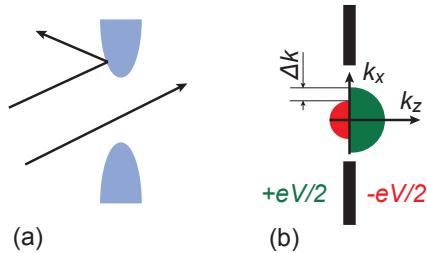


Figure 1.2: (a) In a ballistic contact electrons are specularly reflected from the contact boundary or pass through the contact. (b) An orifice-like point-contact between two metallic half-spaces. The isotropic distribution of the wave vector amplitude k at a point of the contact surface is presented. $\Delta k = 2meV/\hbar$ is the difference in wave vector amplitude between right going and left going electrons. Different colors represent the origin of the electron states.

are occupied up to the energy of $E_F + eV/2$, ($E_F - eV/2$) (see Figure 1.2b). The voltage-induced difference in the occupation of the right and left-moving states results in a net current density:

$$j(r) = \int_{E_F - eV/2}^{E_F + eV/2} dE e \langle v_z(E_F) \rangle \rho(E)/2 = e \langle v_z(E_F) \rangle \rho(E_F)/2 \cdot eV \quad (1.3)$$

where e is the electron charge, $\langle v_z(E_F) \rangle$ is the average velocity of the right-moving electrons in the z direction at the Fermi-energy (E_F), which is *const.* in the interval $[E_F - eV/2, E_F + eV/2]$. $\rho(E_F)/2$ is the density of states of the right-moving electrons at E_F . Inserting the free electron values of $\langle v_z \rangle = \hbar k_F/2m$ and $\rho(E_F) = mk_F/\pi^2 \hbar^2$, the integration of $j(r)$ over the contact area leads to the conductance (the so called Sharvin conductance):

$$G_s = \frac{2e^2}{h} \left(\frac{k_F a}{2} \right)^2 \quad (1.4)$$

where h is the Plank constant, a is the contact radius and k_F is the fermi wave number. Note that the Sharvin conductance depends only on the electron density (through k_F), and is independent of the resistivity ρ and the mean free path L_m . In Equation (1.4) the quantity $2e^2/h = G_0$ is defined as conductance quantum. The quantity $(k_F a/2)^2$ describes the number of ‘conductive channels’ [3]. For metals, $k_F \sim 13 \text{ nm}^{-1}$, the constriction radius of atomic dimensions is $\sim 0.5 \text{ nm}$, $(k_F a/2)^2 \sim 1.7$. This suggests a

single atom corresponds to a single conductance channel. It implies in atom-sized constrictions, conductance decreases in well-defined drop-steps since the number of contacting atoms decreases in one or few atoms at the time. Conductance drop-steps have indeed been observed in many experiments [3]. A more detailed calculation based on the Boltzmann equation predicts that the voltage drop occurs in the close vicinity of the contact center (on the length-scale of a) [8]. This potential gradient accelerates the transmitted electrons, but the energy is not relaxed until inelastic scattering takes place further away from the contact.

Intermediate regime

In the intermediate regime between the diffusive and a ballistic point-contact an interpolating formula can be set up by solving the Boltzmann equation for arbitrary ratio of the contact diameter and the mean free path L_m [9]:

$$R = (L_m/d) \cdot \frac{16\rho}{3\pi d} + \Gamma(L_m/d) \frac{\rho}{d} \quad (1.5)$$

where ρ is resistivity, d is the contact diameter and $\Gamma(L_m/d)$ is a monotonous function, that has to be determined numerically, with the limiting cases $\Gamma(0) = 1$; $\Gamma(\infty) = 0.694$. Note that the first term is exactly the Sharvin resistance by inserting the Drude resistivity $\rho = mv_F/L_m e^2 n$ into Equation (1.5), hence the conductance is independent of L_m . This formula allows one to estimate the contact diameter from the contact resistance.

Landauer formalism: ballistic transport in quantum wire

In atomic-sized contacts when the contact width $W \sim \lambda_F$, the wave nature of the electrons become relevant. The scattering approach pioneered by Landauer [10] is employed to describe electron transport through such a contact. It relates the transport properties (conductances) with the transmission and reflection probabilities for carriers incident on the constriction.

In an ideal ballistic wire with constant transversal confining potential along its axis, the quantum mechanical solution for the wave function of the wire gives electron's states which are plane waves along the wires axis and standing waves in the transverse direction. The energy of the electron states are $E_n(k) = E_n + \hbar^2 k^2 / 2m$, where k is the wave vector in the axis direction, n the index of the n th quantized transverse wave function (see Figure 1.3a). Each transverse wave function constitutes a so-called conductance channel. The macroscopic electrodes are introduced as ideal electron reservoirs in contact with the wire and have a well defined electrochemical potential (μ) and a temperature. The electrodes inject electrons corresponding to their

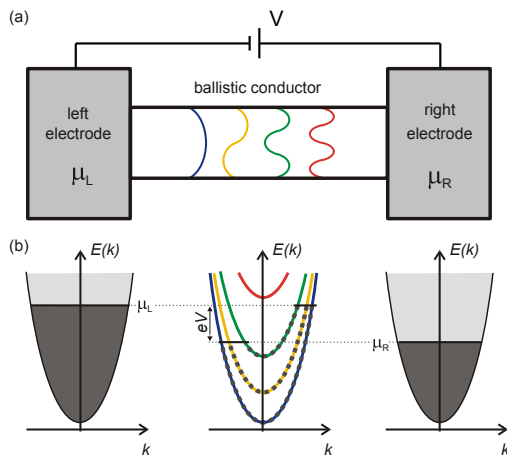


Figure 1.3: (a) Ballistic quantum wire connected to two electrodes. The electrodes emit electrons to the channel with the distribution functions corresponding to electrochemical potentials μ_L and μ_R . The wave function of the different transverse modes are represented by colors. (b) Illustration of the energy dispersion and occupation of the states. In the leads the transverse modes are filled up to their respective electrochemical potential. In the ballistic quantum wire only few transverse modes are filled up to the electrochemical potential. The $+k/-k$ (right moving / left moving electrons) states are filled differently as denoted by the bold dotted line. [4].

distribution function and are assumed to absorb the entering electrons without reflection. The applied voltage V shifts the electrochemical potential by $\mu_R - \mu_L = eV$, which leads to the change in the occupation of the electron states, as presented in Figure 1.3b. The imbalance between the occupation of the right and left moving states results in a net current in the wire, which is:

$$I = 2e \sum_{k,n} \frac{v_k}{L} [f_L(E_n(k)) - f_R(E_n(k))] = \frac{2e}{h} M \int_{\mu_L}^{\mu_R} [f_L(E) - f_R(E)] dE \quad (1.6)$$

where the $f_{L/R}$ are the Fermi distributions in the left and right electrode, n runs over the channels with occupied states, and L is the length of the wire. The sum over k is replaced by an integral over E using one-dimensional density of states $\rho(E) = 1/v_k \hbar$. M is the number of available channels as determined by the diameter of the wire. At zero temperature $f_{L/R}(E)$ are

step functions, equal to 1 below $E_F + eV/2$ and $E_F - eV/2$, respectively, and 0 above these energies. This expression leads to conductance:

$$G = \frac{I}{V} = \frac{2e^2}{h} \cdot M = G_0 \cdot M, \quad (1.7)$$

which is quantized with the unit of the conductance quantum, $G_0 = 2e^2/h \simeq (12.9k\Omega)^{-1}$. This demonstrates that an ideal (i.e. without scattering) perfect single mode conductor ($M=1$) between two electrodes has a finite conductance G_0 .

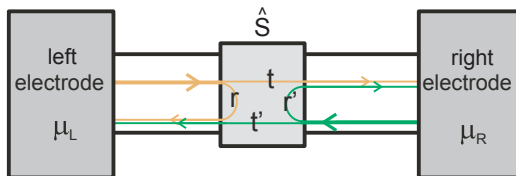


Figure 1.4: The model of arbitrary conductor with scattering unit connected to the electrodes through ballistic wires. The scattering unit transmits or reflects electrons defined by a scattering matrix.

Scattering process can be introduced by using a scattering center in the quantum wire (see Figure 1.4). At the scattering center particles incident from reservoir L (R) are reflected with probability r (r') and transmitted with probability t (t'). Different modes of the wire can be incorporated by using diagonal matrices \mathbf{t} , while there is no coupling of different modes. The scattering matrix is obtained by combining all those matrices, it gives

$$\hat{S} = \begin{pmatrix} \mathbf{r} & \mathbf{t}' \\ \mathbf{t} & \mathbf{r}' \end{pmatrix}$$

The current is then expressed as,

$$I = \frac{2e}{h} \int \text{Tr}(\mathbf{t}^\dagger \mathbf{t}) [f_L(E) - f_R(E)] dE$$

Since $\mathbf{t}^\dagger \mathbf{t}$ is hermitian, it can be diagonalized and has real eigenvalues T_i , the transmission probability of each mode with $0 < T_i < 1$. At zero temperature and $V \rightarrow 0$ the conductance can be expressed in a simple form of:

$$G = \frac{2e^2}{h} \sum_{i=1}^{N_c} T_i, \quad (1.8)$$

where N_c is the number of eigenchannels. N_c is limited by the narrowest cross section of the contact, where the number of occupied transverse modes is the smallest [11]. Equation (1.8) is known as the Landauer formula [12; 13].

1.1.3 Quantum Tunneling

If two electrodes are separated by a thin insulating film (or small gap), and the film is sufficiently thin, current can flow between the two electrodes by means of the quantum tunneling [14]. The first theoretical study of this phenomenon was brought forward by Sommerfeld and Bethe [15], while Holm and Kirschstein [16; 17] described it for different bias voltages. A compact theory for the current flow through a generalized barrier was proposed by Simmons [18] as summarized below.

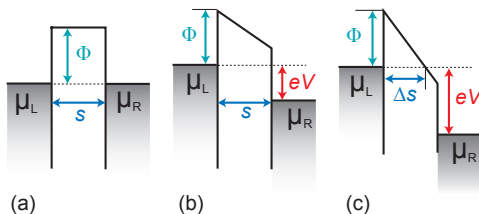


Figure 1.5: Rectangular potential barrier in insulating film between metal electrodes for (a) $V = 0$; (b) $V < \Phi/e$; (c) $V > \Phi/e$. Φ is the barrier height, μ the Fermi level of left electrode, s the width of barrier and Δs the effective barrier width at Fermi level μ .

In quantum theory, a particle can tunnel through a potential barrier larger than its kinetic energy with a finite probability. In Figure 1.5 we illustrate this process for a rectangular potential barrier between two metal electrodes. Φ is the barrier height, μ_L the Fermi level of left electrode, s the width of barrier and Δs the effective barrier width at Fermi level μ_L . The probability $D(E_x)$ that an electron can penetrate a potential barrier of height $\Phi(x)$ is given for a smooth potential by the WKB approximation [19]:

$$D(E_x) = \exp\left\{-\frac{4\pi}{h} \int_0^{\Delta s} [2m(\Phi(x) - E_x)]^{\frac{1}{2}} dx\right\}$$

where $E_x = mv_x^2/2$ is the energy component of the incident electron in the x direction. The number of the electrons tunneling through the barrier from

left to right electrode per area and per second N_L is given by

$$N_L = \int_0^{v_m} v_x n(v_x) D(E_x) dv_x = \frac{1}{m} \int_0^{E_m} n(V_x) D(E_x) dE_x, \quad (1.9)$$

where E_m is the maximum energy of the electrons in the electrode, and $n(v_x)dv_x$ is the number of electrons per unit volume with velocity between v_x and $v_x + dv_x$. Assume the electrodes have an isotropic velocity distribution, the number of electrons per unit volume with velocity between the usual infinitesimal can be related to Fermi-dirac distribution function $f(E)$ with

$$n(v)dv_x dv_y dv_z = (2m^4/h^3)f(E)dv_x dv_y dv_z$$

Consequently $n(v_x) = (4\pi m^3/h^3) \int_0^\infty f(E) dE_r$ with m the effective electron mass, h Planck's constant and E_r the energy in polar coordinates of the incident electrons. The electron current N is composed of the net number of electrons N_L tunneling from left electrode and N_R from right electrode. The tunneling current density J is then given by

$$J = e(N_L - N_R) = \int_0^{E_m} D(E_x) \xi dE_x$$

with $\xi = (4\pi m^2 e/h^3) \int_0^\infty [f(E) - f(E + eV)] dE_r$ and at zero temperature

$$\xi = \begin{cases} (4\pi m^2 e/h^3)(eV) & 0 < E_x < \mu - eV \\ (4\pi m^2 e/h^3)(\mu - E_x) & \mu - eV < E_x < \mu \\ 0 & E_x > \mu \end{cases}$$

After integration and simplification the tunneling current density J can be expressed in the following form:

$$J = J_0 \{ \bar{\phi} e^{-A\sqrt{\bar{\phi}}} - (\bar{\phi} + eV) e^{-A\sqrt{\bar{\phi} + eV}} \} \quad (1.10)$$

where $J_0 = e/2\pi h(\beta\Delta s)^2$, $A = (4\pi\Delta s/h)\sqrt{2m}$. $\bar{\phi}$ is the mean barrier height above Fermi level μ . β depends on geometrical details, for many cases $\beta = 1$ holds [18]. The Equation (1.10) can be applied to any shape of potential barrier. For a rectangular potential barrier, the mean barrier height $\bar{\phi}$ and the effective film thickness Δs depend on the voltage V , as it is illustrated in Figure 1.5:

$$\begin{cases} (a) V = 0, & \bar{\phi} = \Phi, \Delta s = s \\ (b) V < \Phi/e, & \bar{\phi} = \Phi - eV/2, \Delta s = s \\ (c) V > \Phi/e, & \bar{\phi} = \Phi/2, \Delta s = s\Phi/eV \end{cases}$$

At low-voltages ($eV \simeq 0$) the tunneling current density J is a linear dependence on V . The junction behaves Ohmic at very low voltages ($V \ll \Phi/e$). It becomes non-linear at higher voltages ($V \lesssim \Phi/e$). At voltages $V > (\Phi + \mu)/e$ only electrons from left electrode can tunnel to right electrode. This situation is analogous to that of field emission from a metal electrode. Where the first accurate description of field emission obtained by Sir Ralph Fowler and Lothar Wolfgang Nordheim in 1928.

1.2 Electromigration

In an ideal conductor, where atoms are arranged in a perfect lattice structure, the electrons moving through it would experience no collisions. In real conductors, defects in the lattice structure and the random thermal vibrations of the atoms about their positions cause electrons to collide with the atoms, impurities and grain boundaries. When an electron changes its motion due to a collision with one such scatterer of the crystal lattice, it transfers momentum to the scatterer and exerts a force on it. Normally, the amount of momentum imparted by the relatively low-mass electron is not enough to permanently displace an atom. However, if many electrons bombard the atoms with enough momentum transfer, this can cause the scatterer to move out of its original equilibrium position. The frequency of these relocation events increases with current density. This mass transport process caused by a large electric current density ('electron wind') is called electromigration (EM).

The phenomenon of EM has been known for over 100 years. It was first discovered by the French scientist Gerardin. The topic first became of practical interest in 1966 when the first integrated circuits were commercially available. EM posed a serious problem since it caused interconnecting lines to fail. Understanding and suppressing EM in the ever denser circuitry became one of the major efforts in the semiconductor industry. The intriguing question of the exact force acting on a scatterer in a metal in the presence of an electric field has led to fundamental research of many well-known theorists, such as Friedel, Landauer and Peierls.

1.2.1 Electron wind force

We introduce a macroscopic description of EM with the theory of irreversible thermodynamics [20]. This general framework relates the occurrence of fluxes \mathbf{J}_i (e.g. fluxes of atoms, electrons, or heat) to the presence of macroscopic 'forces' \mathbf{X}_j (e.g. gradients of the chemical potential, electric potential or temperature) in a system. It states that all forces \mathbf{X}_j together determine

each flux \mathbf{J}_i according to [20]:

$$\mathbf{J}_i = \sum_{j=1}^n L_{ij} \mathbf{X}_j, \quad i = 1, \dots, n \quad (1.11)$$

Here the L_{ij} represent phenomenological coefficients which do not depend on the \mathbf{X}_j , i.e. this is a linear response theory. A theorem concerning the coefficients L_{ij} was derived by Onsager [21]. If \mathbf{J}_i and \mathbf{X}_j can be chosen such that the total entropy production rate $\dot{s} \geq 0$ equals

$$\dot{s} = \frac{1}{T} \sum_{i=1}^n \mathbf{J}_i \cdot \mathbf{X}_i,$$

the Onsager reciprocal relations hold: $L_{ij} = L_{ji}$.

In the EM case we are mainly interested in the electron particle flux (\mathbf{J}_e) and the flux of metal atoms (\mathbf{J}_m). These fluxes are induced by a set of ‘forces’ (or potential gradients), \mathbf{X}_j . For the particle forces, we can write $\mathbf{X}_j = -\nabla \mu_{ec}^j$. Here, $\mu_{ec} = \mu + Ze\varphi$ is the electrochemical potential, with φ , μ and Z , the electrostatic potential, the chemical potential and particle charge ($Z=-1$ for electrons). If we look at only the flux of metal atoms \mathbf{J}_m , we have:

$$\mathbf{J}_m = -L_{m,m} \nabla \left(\frac{\mu_{ec}^m}{T} \right) - L_{me} \nabla \left(\frac{\mu_{ec}^e}{T} \right). \quad (1.12)$$

For materials with a high conductivity, the electrons are evenly distributed in the material, and we can ignore $\nabla \mu^e$. Because all charge current is due to electron flux, we have $-\nabla \varphi = \mathbf{E} = \rho \cdot \mathbf{j}$ (with ρ the electrical resistivity). Hence we obtain:

$$\mathbf{J}_m = -L_{mm}^* (\nabla \mu^m - Z^* e \rho \mathbf{j}), \quad (1.13)$$

where we define $L_{ij}^* = L_{ij}/T$, and introduce an effective charge Z^* :

$$Z^* = Z - \frac{L_{me}^*}{L_{mm}^*}. \quad (1.14)$$

The atoms behave as if they have a charge Z^* [20; 22; 23] in an electric field \mathbf{E} . This effective charge is due to momentum transfer from electrons to atoms. Often we describe the force acting on atoms as the net force $\mathbf{F} = Z^* e \mathbf{E}$ of wind force \mathbf{F}_w and direct force \mathbf{F}_d (see Figure 2.2). We write $\mathbf{F}_w = Z_w e \mathbf{E}$ and $\mathbf{F}_d = Z_d e \mathbf{E}$. By comparing two expressions for Z^* : $Z - L_{me}^*/L_{mm}^* = Z^* = Z_d + Z_w$ we found that, it is equivalent to write ‘ $Z_d = Z$ ’ and ‘ $Z_w = -L_{me}^*/L_{mm}^*$ ’, identifying the bare ion charge as Z_d and $-L_{me}^*/L_{mm}^*$ as the wind force contribution [24; 25]. Generally, $L_{me}/L_{mm} \gg Z_d$, so the net force acting on the gold atoms will be in the

direction of the electron flow.

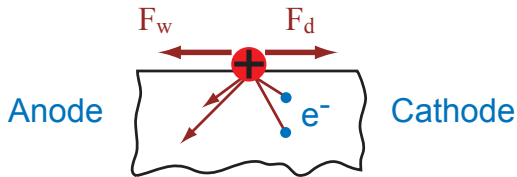


Figure 1.6: The force acting on atoms is the net force of the wind force \mathbf{F}_w and the direct force \mathbf{F}_d . F_d is the electrostatic interaction of the atom with the electric field. \mathbf{F}_w is the momentum transfer from the electrons.

To understand the electron-atom interaction term $-L_{me}/L_{mm}$ we consider a ballistic model suggested by Fiks [24] and Huntington and Grone [25]. In their approach, the wind force \mathbf{F}_w is calculated from the net momentum transfer of incident electrons to a scattering center. Suppose we have free electrons in a metal with Fermi velocity v_F and relaxation time τ . If an electric field \mathbf{E} is applied, the electrons gain an average momentum $\Delta p = -\tau eE$ before the next scattering event. Those electrons within a distance $l = v_F\tau$ are able to reach the scatter within a time τ . The wind force F_w is then determined by summing the momentum transfer over the total number of electrons off scattering the scatterer. Furthermore, the number of scattering events at the scattering center is decided by the scattering cross section σ_x . Assuming an electron density n , we then have $nl\sigma_x$ incident electrons, each transferring a momentum Δp . The wind force follows: $\mathbf{F}_w = \frac{1}{\tau} \sum \Delta p = -nl\sigma_x e\mathbf{E}$. Note that $\mathbf{F}_w = Z_w e\mathbf{E}$, hence we have

$$Z_w = -nl\sigma_x, \quad (1.15)$$

this expresses the wind force dependence on the number of electrons in a cylinder of volume $l\sigma_x$. Normally in a good metal $l\sigma_x$ is much larger than the unit cell volume Σ_c . Furthermore we have $Z_w = -nl\sigma_x$ whereas $Z \approx n\Omega_c$. Therefore we can conclude that in a good conductor, Z_w dominates over Z_d because $|Z_w| \gg |Z| \gtrsim |Z_d|$. Another way to see that Z_w is larger in a good conductor is to rewrite $Z_w = K/\rho$, where K is some constant and ρ the resistivity. This can be obtained from the fact that momentum is transferred from electrons, hence the electron wind will rather be proportional to the electron flux $J_e = j(-/e)$ than to the electrical field $E = \rho j$. Writing $F_w = Z_w eE \sim j$ implies $Z_w = K/\rho$. Consequently Z_w is large in good conductors.

To find out the atom-atom interaction L_{mm}^* , we use the Einstein relation

$D = L_{mm}^* d\mu/dc$, where D is the diffusion coefficient and c the concentration. For the chemical potential we have $\mu = kT \ln(c)$ [23]. The diffusion constant can be expressed as $D = D_0 e^{-E_a/kT}$ [26], where E_a is the activation energy of gold diffusion on the surface, which is 0.12 eV [27], k the Boltzmann's constant, and T is the absolute temperature. We obtain $L_{mm}^* = \frac{D_0}{kT} c e^{-E_a/kT}$. The term $\nabla\mu^m = \Omega \frac{d\sigma}{dx} = \Omega \Delta\sigma/L$ is the driving force due to stress σ [26; 28; 29], where Ω is a constant and $\Delta\sigma/L$ is the stress gradient on a length scale L . This compressive stress (as well as the atom concentration) is built up at the anode side because EM flux transports atoms towards it. This build up increases the chemical potential of the metal as well. Hence, we rewrite the atom flux as:

$$J_m = \frac{D_0 c}{kT} e^{-E_a/kT} (Z^* e j \rho - \Omega \frac{\Delta\sigma}{L}). \quad (1.16)$$

In an EM experiment one always measures $Z^* = Z_d + K/\rho$ instead of the bare ion charge Z . In many cases Z^* deviates strongly from Z_d . To determine Z_d and K , one usually plots Z^* as a function of $1/\rho$ and extrapolates to $1/\rho = 0$.

1.2.2 Essential parameters in electromigration

Critical current density

From Equation (1.16) one can see that if $Z^* e j \rho < \Omega \Delta\sigma/L$, the electron wind force is balanced by the stress gradient, the atom flux is zero and no EM is present. Consequently a minimum in current density exists, at which EM first occurs. It is straightforward to define a critical current density j_c :

$$j_c = \Omega \Delta\sigma / Z^* e \rho L. \quad (1.17)$$

When $j > j_c$ EM can be triggered in a conducting wire.

Temperature

Enhanced temperature accelerates the process of EM by causing the atoms of the conductor to vibrate further from their ideal lattice positions, increasing the amount of electron scattering. Furthermore, the atom flux \mathbf{J}_m is related to temperature T through diffusion constant. At elevated temperature the metal atoms are much more mobile, and easy to move out of their equilibrium positions. At lower temperature the smaller vibration of atoms around their ideal lattice positions reduces their electron scattering cross-section. Less scattering means less momentum transfer hence smaller wind force. A critical temperature T_c is introduced to evaluate a conductor

under a certain current density to obtain an obvious irreversible resistance increase due to atom flux J_{mc} . It is observed that T_c is very similar for the environment temperature range from 4 K to 330 K [29]. This demonstrated that a critical temperature is necessary to obtain enough mass flux due to EM which results in a visible material transport.

The observation of the temperature influence on EM is reflected in the empirical Black's equation [30], which is commonly used to predict the life span of interconnects in integrated circuits against EM damage. A larger atom flux induced by EM in a conducting wire means a shorter MTTF (mean time to failure), which is expressed as:

$$MTTF = Aj^{-2} e^{\frac{E_a}{kT}} \quad (1.18)$$

Here A is a constant based on the cross-sectional area of the wire, j is the current density, E_a is the activation energy, k is the Boltzmann constant, T is the temperature. The mean time to failure caused by EM is shorter at higher temperature. The temperature is often attained by Joule heating under high current density in the metal wire.

Blech length

Note that j_c in Equation (1.17) is temperature independent, since $Z^* \rho = const.$ does not depend on temperature. In various experiments j_c is found to be inversely proportional to the length of the wire. The product of the wire length L and the critical current density j_c is approximately constant (1260 A/cm in an Al stripe at 350°C) [26]. But the $j_c L \propto 1/\rho$ product increases with decreasing temperature. According to Equation (1.17) if the length L is very small, j_c will be very large. It is possible that j_c can not be reached for a certain length L of the wire. This length is the so called Blech Length, below which EM will not start in the conducting wire.

Crystalline structure

Besides temperature the grain size of the metal crystalline has a large influence on EM too. EM occurs often first on the grain boundaries, because the inhomogeneity of the crystalline structure at the grain boundaries causes vigorous scattering and momentum transfer to metal atoms there. The grain boundaries provide a pathway for easy diffusion too, therefore EM propagates along them. j_c is smaller in a metal wire of same geometry if it consists of smaller grains. In a very narrow wire where the grain size is similar than the wire width, 'bamboo' like appearance (Figure 1.7) is formed where most of the grains span the line width. There j_c is found to be much more en-

hanced. Heat treatment may fuse the small grains and increase the grain size.

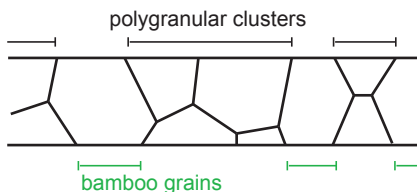


Figure 1.7: Illustration of ‘bamboo’ grains and polygranular clusters in a conducting wire. Electromigration (EM) is likely to be suppressed in metal wire with ‘bamboo’ like crystalline structure.

1.2.3 Electromigration in molecular electronics

Single-molecule electronics has been the focus of substantial worldwide research [31; 32; 33; 34; 35]. Direct measurement of electron flow through a single molecule promises a better understanding of the electron transfer processes in molecules. To measure a single molecule (or a few molecules), nano-sized metallic junctions are needed that ideally have both small and well controlled junction areas and narrow gaps of only a few nanometers in size. The molecules are ‘trapped’ within these gaps and can then be electrically measured.

Various methods have been developed to define and measure such molecular junctions [36; 37], such as the scanning probe method [38], mechanically controlled break junctions [39; 40], crossed-wire junctions [41], molecular layers sandwiched between mercury droplets [42], and EM induced nano-gaps [43]. Among these methods, EM-induced nano-gaps have successfully been employed for a broad range of molecules, revealing various transport phenomena [44; 45; 46; 2; 47]. For example, Coulomb blockade and vibration-assisted electron tunneling was studied in C_{60} [44] and C_{140} [45], and the Kondo effect was observed in an organo-metallic molecule [46; 2]. EM-junctions can be very stable as recently demonstrated by measurements of the gate-controlled charging of a single molecule and its temperature dependence [47]. Moreover, magnetic molecules have been studied [48], and in these measurements the signatures of the magnetic state and the associated anisotropy could be determined. EM-junctions have the advantage that gates with a decent gate-to-molecule coupling can be fabricated [46]. However at the same time they have the disadvantage that nano-particles can

form out of the electrode material (during the EM-process) through which electric transport may occur subsequently. Because transport through small metallic particles may show ‘molecular’ features, e.g. Coulomb blockade and the Kondo effect [49; 50; 51], the distinction is not straightforward [52]. A better control of EM may yield nano-gaps with fewer particles [53; 54]. The development of refined EM processes is therefore highly desirable.

In Section 1.2 we introduced that EM is the directed migration of atoms caused by a large electric current density. EM proceeds by momentum transfer from electrons to atoms and requires sufficient atom mobility to occur. The latter increases at higher temperatures, so that local Joule heating is an important parameter in addition to current density [30]. The formation

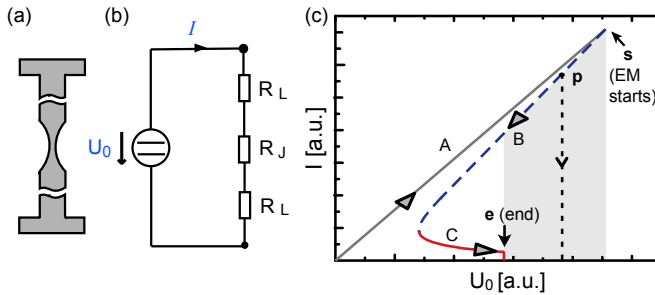


Figure 1.8: (a) Schematics of the constriction forming the junction with attached leads. (b) The equivalent circuit diagram with bias voltage U_0 applied over a two-terminal junction. R_L , R_J are the lead and junction resistances, respectively. (c) Schematic characteristic of the current I versus bias voltage U_0 during software controlled 2-terminal electromigration (EM) [55; 56]. EM starts at point s and the junction breaks open at point e .

of an EM nano-gap starts with the lithographic definition of a metallic wire with a constriction (junction, see Figure 1.8a) where the EM process will be effective. EM narrows the junction down, until a gap forms and the process self-terminates. In such lithographically defined wires, the bonding pads are far away from the constriction, yielding long leads with comparatively large lead resistances R_L . Typically, R_L is much larger than the resistance of the junction R_J (Figure 1.8b). Although a voltage U_0 is applied, the junction is effectively current-biased through the large series resistance [47; 29]. Consequently, as EM starts shrinking the junction and R_J increases, the power dissipated on the junction grows proportionally to R_J , causing a thermal run-away like in a fuse. When this happens, the resulting gaps are larger than 10 nm and cannot be used for the trapping of molecules. A closer

view on this instability is schematically shown in Figure 1.8c. There are three regimes, A-C. Along A the current-voltage characteristics $I - U_0$ is reversible. EM sets in at point **s** and the system crosses-over to the unstable branch B (dashed curve). In the final and again stable branch C, R_J dominates over the R_L and EM evolves until the junction breaks open at the end point **e**. Branch B is unstable, because of the multi-valued nature of the $I - U_0$ characteristics in this regime. In the shaded region, the junction can rapidly be destroyed. If the junction is at point **p**, for example, and U_0 is maintained constant, the junction will switch to the open state, well above the breaking point **e**. Because this happens at much larger power dissipation than would be the case at point **e**, the junction is ‘burnt’ off by a thermal run-away. In order not to destroy the junction, one therefore has to ensure that the junction follows branch B. This can be done manually, or better by software control [55; 56; 57]. If the resistance is seen to increase as a function of time more than 5 %, the software immediately switches back the applied voltage U_0 to lower values to stop EM. U_0 is then gradually increased again to start EM process. The gap formation consists of hundreds of very short EM processes. This approach is quite slow, as U_0 needs to be set back and slowly ramped up repetitively. A much better approach is to remove the destructive region (shaded in Figure 1.8c) altogether. Point **s** occurs at larger U_0 values than point **e** because $R_L \gg R_J$. Hence, designing devices with low lead resistances will solve the problem, since then the junction is voltage-biased [47; 29]. This was demonstrated by Trouwborst *et al.* who used much wider and thicker leads [29].

In this thesis (Section 2.2) we introduce another approach which does not need thick contact layers. We eliminate the lead resistances by lithographically defining four terminals to each junction and by using a novel and fast electronic feedback scheme.

1.3 Introduction to noise

In this section we introduce some basic definitions in noise spectra. In our experiments we measure the thermal noise and $1/f$ noise. We explain the deviation of the thermal noise in conductor. Finally we discuss $1/f$ noise and few models to describe it.

1.3.1 Correlation function and spectral density of noise

Noise is the dynamical random fluctuations of a measured quantity around its mean value. The theory of fluctuations is based on mathematical theory of random processes. Let $x(t)$ be a quantity that randomly varies in time t and let $\langle x \rangle$ be its mean value. The time dependent fluctuation is defined

as $\delta x(t) = x(t) - \langle x \rangle$. The correlation function shows how the fluctuations evolve in time on average. It is a non-random characteristics of the kinetics of these random fluctuations. The correlation function ψ_x can be determined by averaging over a long enough measurement time t_m of $x(t)$ in one system if the system is ergodic. The condition of the ergodicity of the system (in equilibrium) is the measurement time $t_m \ll \tau$, where τ the characteristic times of passing through all groups of representative states. The correlation function of a variable $x(t)$ determines how strongly two measurements at $t = t_1$ and $t = t_2$ are related on average:

$$\psi_x(t_1 - t_2) \equiv \langle \delta x(t_1) \delta x(t_2) \rangle = \lim_{t_m \rightarrow \infty} \frac{1}{t_m} \int_{-t_m/2}^{t_m/2} dt \delta x(t_1 + t) \delta x(t_2 + t)$$

The correlation function of several correlated random quantities $x_\alpha(t)$ ($\alpha = 1, \dots, M$) can be written as a matrix:

$$\psi_{\alpha\beta}(t_1, t_2) = \langle \delta x_\alpha(t_1) \delta x_\beta(t_2) \rangle$$

The functions with $\alpha = \beta$ are called auto-correlation function, those with $\alpha \neq \beta$ cross-correlation functions.

In praxis, time dependent fluctuations are often measured with a spectrum analyzer. The input signal is passed through a bandpass filter of width Δf and central frequency f_0 . The measured quantity $P_x(f_0, \Delta f)$ is the noise power in a frequency window Δf . $P_x(f_0, \Delta f)$ is time independent, proportional to the bandwidth Δf and a function of f_0 . Therefore noise can be characterized by power spectral density (PSD), which is the mean-squared fluctuations per unit frequency bandwidth. The noise power spectral density (PSD) $S_x(f)$ is defined by the following equation:

$$P_x(f_0, \Delta f) = 2 \int_{f_0 - \Delta f/2}^{f_0 + \Delta f/2} df \psi_x(\omega) \approx S_x(f_0) \Delta f$$

Because we discuss noise in frequency space, we make the Fourier transform of $\psi_x(t)$ into $\psi_x(\omega)$, where $\psi_x(t)$ the auto-correlation function of $\delta_x(t)$. Hence we obtain:

$$S_x(f) = 2 \int_{-\infty}^{+\infty} dt e^{i\omega t} \psi_x(t) \equiv 2\psi_x(\omega) \quad (1.19)$$

This relation is called Wiener-Khintchine theorem (Wiener, 1930; Khintchine, 1934). It states that the power spectral density is twice the Fourier transform of the correlation function.

1.3.2 Thermal noise

Thermal noise is always present in any conductor at temperatures $T > 0$. It is the intrinsic current noise due to thermal motion of electrons. Thus thermal noise present even without an extrinsic net current.

Let us look at a model [58; 59] of thermal noise in a short-circuited classical resistor R of length L and cross-section area A in thermal equilibrium. The Drude conductance is $G = (A/L)(ne^2\tau/m)$, where n is the conduction electron density, τ the relaxation time and m the electron mass. The average kinetic energy of an electron moving in length direction 'x' is $m\langle v_x^2 \rangle / 2 = k_B T / 2$. The charge transferred between two terminating electrodes by a single electron over one mean free path L_m during the collision time τ is $ev_x\tau/L_m$. The current average associated with this process is i :

$$i = \frac{ev_x\tau/L_m}{\tau} = \frac{e}{L_m}v_x,$$

Because the total average current of the ensemble is $\langle i \rangle = 0$, the variance in the current i of one electron over a large number of collisions equals

$$\langle \Delta i^2 \rangle \equiv \langle i^2 \rangle - \langle i \rangle^2 = \frac{e^2 \langle v_x^2 \rangle}{L_m^2} = \frac{e^2 k_B T}{L_m^2 m}$$

The total number of conduction electrons in the resistor is $N = nLA$. We assume that these electrons are independent (no interactions) and thus exhibit identical fluctuations. Therefore the total current fluctuation is $\langle \Delta I^2 \rangle = N \langle \Delta i^2 \rangle$. Thus, it follows

$$\langle \Delta I^2 \rangle \equiv \Psi_I(t=0) = N \cdot \frac{e^2 k_B T}{L^2 m} = \frac{k_B T G}{\tau}$$

Because the ensemble events of each single electron are uncorrelated in time, the correlation function $\Psi_I(t)$ is decaying exponentially [60; 61]:

$$\Psi_I(t) = \Psi_I(0)e^{-|t|/\tau}$$

using the relation for the spectral density with correlation function from Equation (1.19), we obtain the current power spectral density

$$\begin{aligned} S_I(f) &= 2 \int_{-\infty}^{+\infty} dt e^{i2\pi ft} \frac{k_B T G}{\tau} e^{-|t|/\tau} = 4k_B T G \frac{1}{1 + (2\pi f\tau)^2} \\ &\simeq 4k_B T G \end{aligned} \quad (1.20)$$

for $f \ll \tau^{-1}$. Equation (1.20) is known as the Johnson-Nyquist relation [62; 63]. Typically the relaxation time τ is about 10^{-12} sec, hence

Equation (1.20) holds for $f \ll 10^{12}$ Hz. Normally we measure noise at much lower frequency, i.e. the upper frequency limit of our spectrum analyzer is 10 MHz $\ll 10^{12}$ Hz. Therefore we measure a white thermal noise spectrum as expressed in Equation (1.20). Thermal noise can be measured as voltage noise over the resistor R as well. In a macroscopic conductors at magnetic field $B = 0$ assuming $G = 1/R$ and $V = IR$, we obtain $S_V(f) = S_I(f) \cdot R^2 = 4k_B T R$.

1.3.3 Generation and Recombination noise

Generation and recombination (GR) noise in semiconductors originates from electron traps that randomly capture and emit charge carriers, thereby causing a fluctuation in the number of carriers available for current transport. In addition the trapping of carriers can locally change the Fermi-level, which in turn will reduce or enhance the flow of carriers in the vicinity of the trap [64]. The GR spectrum of the conduction electrons is given by

$$S_n(f) = \langle (\Delta N)^2 \rangle \frac{4\tau}{1 + (2\pi f\tau)^2} \quad (1.21)$$

where ΔN is the fluctuation in the number of carriers, f is the frequency, and τ is the time constant, which is reciprocal of the characteristic rate of capture and emit process in the system. The shape of the spectrum given by Equation (1.21) is called Lorentzian. At low frequencies ($f\tau \ll 1$) the spectrum is approximately constant, and at high frequencies ($f\tau \gg 1$) it rolls off like $1/f^2$.

A special case of GR noise is the random-telegraph-signal (RTS) noise, which is illustrated as discrete switching events in time, see Figure 1.9a. An observable RTS signature in the time-domain has a Lorentzian component in the power spectrum, due to the fact of a larger amplitude for the RTS as compared to the amplitude of the remaining noise. In quantum point-contacts where only few conducting channels are involved, the conductance can switch between two or more states, resembling a RTS wave form. This kind of fluctuation has a Lorentzian shaped spectrum as shown in Figure 1.9b.

1.3.4 $1/f$ -noise

In essentially all the noise measurements (apart from shot noise) performed on a vast number of semiconductors, semi-metals, metals, superconductors, an increase of the spectral density with decreasing frequency f approximately proportional to $1/f^\gamma$ with $\gamma \approx 1$ is observed [66; 67; 68; 69]. This type of noise is called $1/f$ -noise. This $1/f$ characteristics can be observed

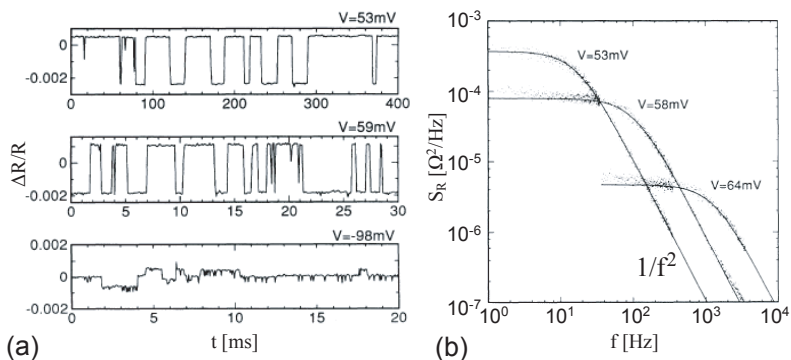


Figure 1.9: a) Two-level resistance fluctuation observed in a Au nano-bridge of 2 nm radius in cross-section. b) Lorentzian shaped spectral density of a single two-level fluctuator for three bias voltages [65].

down to the lowest experimental accessible frequencies ($\sim 10^{-6}$ Hz), and no plateau develops for $f \rightarrow 0$. At high frequencies $1/f$ -noise is generally dominated by thermal noise or shot noise. An example of a measured $1/f$ -noise spectral density in voltage noise is shown in Figure 1.10.

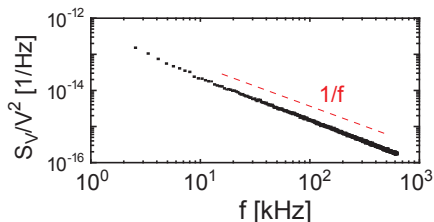


Figure 1.10: An example of a measured $1/f$ -noise spectral density in voltage noise over a MCBJ junction of 100Ω at 50 mV.

There is no general theory of $1/f$ noise in condensed matter, because there exists no universal mechanism of $1/f$ noise. Nevertheless there are models that can describe certain observations or measurements. The common agreement about the origin of the $1/f$ noise is that it comes from the fluctuation of the resistivity (ρ) which depends on both the mobility (μ) and number

(N) of charge carriers. The resistance fluctuations are generally based on the following reasoning: When a constant current I is passed through an ohmic sample, $1/f$ -noise is found in the voltage fluctuations across the sample with a spectral density proportional to I^2 . Vice versa, when the voltage is kept constant, the $1/f$ current noise is found to be proportional to V^2 . The conductance fluctuation can also be measured without current or voltage bias. Voss and Clarke [70] have measured the fluctuation of the spectral density of the equilibrium (Johnson-Nyquist) voltage fluctuations ('noise of the noise'). At low enough frequency ($10^{-2} \sim 1$ Hz) it is proportional to $1/f$, as is implied by the measurement of $S(f)$ under nonzero current. The resistance fluctuations of an ohmic homogenous sample of metals or semiconductors can be expressed by Hooge's [71; 67] empirical relation for $1/f$ -noise:

$$\frac{S_I(f)}{I^2} = \frac{S_V(f)}{V^2} = \frac{S_R(f)}{R^2} = \frac{S_G(f)}{G^2} = \frac{\alpha}{Nf} \quad (1.22)$$

where S_X is the spectral density of fluctuations in X , N is the total number of free carriers, and α is a dimensionless parameter. This expression can be understood by noting that the fluctuating resistance δR generates the fluctuating voltage $\delta V = I\delta R$ over the sample at a constant DC bias current I . The mean square fluctuation, i.e. the noise, is then proportional to I^2 therefore also to $V^2 = (IR)^2$. Similar is for the current noise measured at constant DC bias V , which is proportional to V^2 therefore also to $I^2 = (V/R)^2$. Therefore $S_V/V^2 = S_R/R^2$ at constant DC bias I , and $S_I/I^2 = S_R/R^2$ at constant DC bias V . α is also known as Hooge's constant and originally estimated to about 2×10^{-3} . The validity of Equation (3.2) was questioned because the α is found to vary between 10^{-6} to 10^{-3} [72]. It turned out that the value of α is very sensitive to material quality and processing techniques, hence it can be used as a measurement of quality and relative noise level of material and device. Hooge modified the model [73; 67] to introduce the carrier mobility fluctuation in the bulk of the material as the source of observed conductivity fluctuations. The carriers mobility fluctuations stems from the scattering of carriers by lattice phonon modes. The source of the fluctuations is the fluctuations in the phonon numbers or occupations of various modes. Hooge's constant α in Equation (3.2) is proportional to the lattice mobility (i.e. $\alpha \propto \mu_{lattice}$). In Hooge's model $1/f$ -noise is a volume effect, it scales with the volume of the material. Equation (3.2) has been extensively used for noise measurements in metals and semiconductors. Later, Hooge [72] stressed that Equation (3.2) is an empirical relation. The only assumption necessary is the independence of the involved carrier species, noise is produced as a single-particle effect.

The most accepted model for fluctuations in the number of free carriers

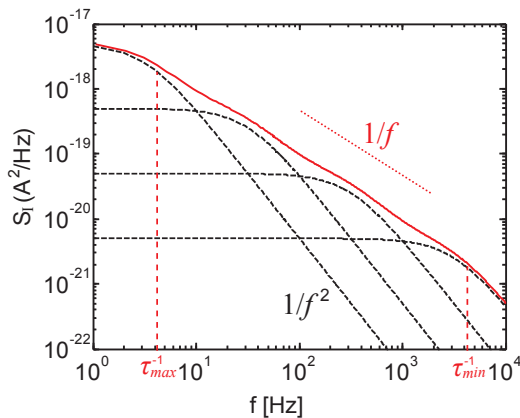


Figure 1.11: Superposition of 4 Lorentzians that gives a spectrum approximately showing a $1/f$ dependence over several decades of frequency. τ_{max} and τ_{min} are the largest and smallest life time of the traps, respectively.

as origin of $1/f$ -noise is proposed by McWhorter [74]. Here GR fluctuations of a large number of traps can produce $1/f$ -noise if the time constants of the traps are distributed as

$$g(\tau) = \frac{1}{\tau \ln(\frac{\tau_2}{\tau_1})} \quad \text{for } \tau_1 < \tau < \tau_2, \quad g(\tau) = 0 \text{ otherwise}$$

τ_1 and τ_2 are the largest and smallest life time of the traps, respectively, which limits the spectrum within the corresponding frequency range. The superposition of the GR noise (Lorentzian, see Equation (1.21)) from many traps distributed according to $g(\tau)$ yields

$$\begin{aligned} S_{tot}(f) &= \int_0^\infty g(\tau) S_{GR}(\tau) d\tau = \frac{1}{\ln(\tau_2/\tau_1)} \int_{\tau_1}^{\tau_2} \frac{4}{\tau} \frac{\langle(\Delta N)^2\rangle \tau}{1 + (2\pi f \tau)^2} d\tau \\ &= \frac{2\langle(\Delta N)^2\rangle}{\pi f \ln \tau_2/\tau_1} [\arctan(2\pi f \tau)]_{\tau_1}^{\tau_2} \\ &\approx \frac{\langle(\Delta N)^2\rangle}{\ln \tau_2/\tau_1} \frac{1}{f} \quad \text{for } 1/2\pi\tau_2 \ll f \ll 1/2\pi\tau_1 \end{aligned} \quad (1.23)$$

Thus a $1/f$ spectrum over a wide frequency range is found. We note that $\int_0^\infty S_{tot}(f) df = \langle(\Delta N)^2\rangle$. An example is given in Figure 1.11 where the GR noise of four individual traps with different time constants adds up to

a $1/f^\gamma$ spectrum with γ close to 1. Here the noise from the traps, which are not correlated with each other, can simply be added to form a $1/f$ type noise spectrum. Traps in the oxide with a uniform random distribution of distances from the oxide-semiconductor interface [75], in for example MOSFETs, yields such a distribution. Therefore $1/f$ -noise is attributed to be the surface effect in McWhorter's model in semiconductor physics. Dutta and Horn [66] explain the $1/\tau$ distribution of relaxation times to originate from a uniform distribution of activation energies. The importance of the requirement in independent traps is pointed out by Hooge [76] in recent years. The $1/f$ spectrum will not be measured if the fastest traps dominate because of the interaction between traps.

There are many other models to describe certain observations and measurements of $1/f$ noise in different systems, such as Voss and Clark's temperature fluctuations model [70], Handel's quantum mechanic model [77], Dutta-Horn model [66; 78], the Self organized Criticality model [79] or the diffusion model [80]. In these models how the dynamics of fluctuations can arise and how it can be linked to the observed power spectrum is described. The other models like the universal Conductance Fluctuation [81], or Local Interference model [82] give a physical process of generating conductivity fluctuations from defect motion but do not provide an explicit theory about the dynamics of the defects. In this thesis we analyze the measured $1/f$ noise based on the Hooge's model.

Chapter 2

Experimental techniques

Experimental techniques are the basis of correct and accurate results in scientific research. In this chapter we first introduce the lithography and metal deposition steps, which are essential for designing and fabricating the devices used for measurements. Then we present a fast, feedback controlled electro-migration (EM) technique to fabricate nano-junctions and nano-gaps. For further investigation of resistance fluctuation in nano-junctions, the setup and calibration process for noise measurements is discussed in detail.

2.1 Sample fabrication

Our devices are fabricated with two sequential lift-off processes on oxidized (400 nm) Si substrates, employing first optical and then e-beam lithography (EBL). The contact pads and the major part of the leads (Figure 2.1a) are formed by optical lithography and the deposition of a 6 nm thick Ti adhesion layer, followed by 50 nm Au. With EBL, we then fabricate the junctions (Figure 2.1b). The junctions consist only 45 nm of Au, without an adhesion layer. The typical size of such an Au junction (constriction) is 200 nm in length and 100 nm in width. The resistance of the junction R_J is around 3 – 10 Ω at room temperature whereas the overall resistance $R = R_J + 2R_L$ typically amounts to as much as 250 Ω . In one optical lithography structure we fabricate 12 EBL structures.

The procedure of sample fabrication is schematically show in Figure 2.2. Below we give the general information and the parameters we use in sample fabrication procedure. Such as substrate preparation, optical and e-beam

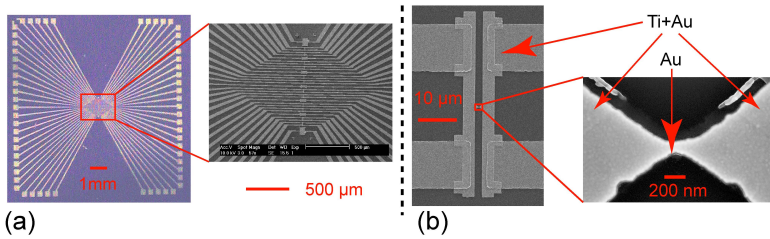


Figure 2.1: (a) Optical lithography structure. (b) EBL structure of the junction with four contact pads. In one optical lithography structure we fabricate 12 EBL structures.

lithography to finally the metal deposition steps. The working principle of optical and e-beam lithography is introduced. In our experiments two types of sample structures are used. We explain the reason and the result of the optimization in sample structure at the end.

Substrate preparation

- EM samples: we use Si wafers as substrate. The oxidized (400 nm) Si wafer was cut into $20 \times 20 \text{ mm}^2$ pieces and cleaned in acetone in an ultrasonic bath for 5 minutes, then rinsed in isopropanol and dried immediately with a nitrogen gas blower. Afterwards, it was cleaned in an ozone-cleaner for 5 minutes. This cleaning process helps to remove the inorganic and organic dust.
- MCBJs samples: we take flexible 0.3 mm thick spring steel as substrate. Because a non-conducting substrate is needed, we cover it with a multi layer of polyimide (Pyralin PI2610 HD Microsystem). The polyimide layer is spin coated (8000 rpm for 40 s) on the substrate and baked at 200°C for 40 minutes. The process is repeated 3 to 4 times in order to obtain 3 to 4 layers of polyimide. At the end it is annealed for 1 hour at 390°C in 10^{-5} bar vacuum. The polyimide layers result in a smooth surface on the steel substrate. The so prepared substrate is then cut into $23.8 \times 9 \text{ mm}^2$ pieces by laser cutting.

Fabrication of metal structures

We use optical and e-beam lithography to fabricate designed metal structures. The working principle of both lithography is similar as shown in

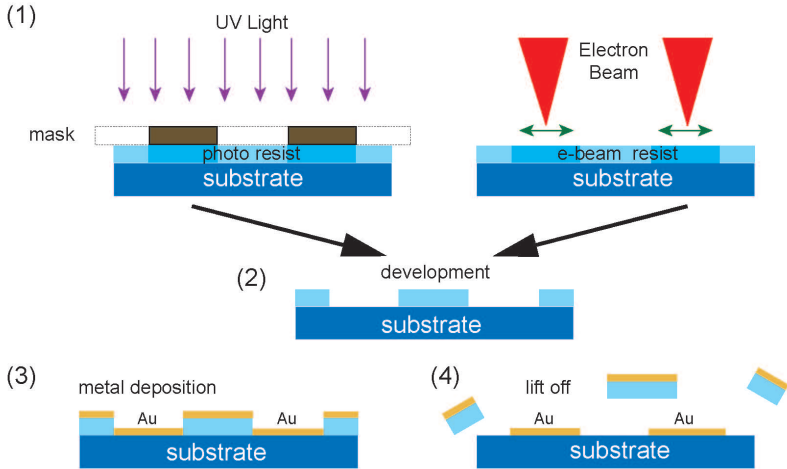


Figure 2.2: (1) Lithography step: Optical lithography and e-beam lithography. (2) Development step. (3) Metal deposition and (4) The lift off step.

Figure 2.2 (1). A resist film which is sensitive to UV light or e-beam is first applied to cover the substrate. By selectively exposing the part of the resist film under the UV light or e-beam, we are able to transfer a pattern into resist film. The feature resolution limit depends on different parameters in lithography process:

- **Optical lithography:** A clear image of a small feature onto the wafer is limited by the wavelength of the light that is used, and the ability of the reduction lens system to capture enough diffraction orders from the illuminated mask. The minimum feature size is proportional to the wavelength of the light. In 2006, features less than 30 nm were demonstrated by IBM using 193 nm light.
- **EBL:** The electron beam widths can go down to a few nm with today's electron optics. However, the feature resolution limit is determined not by the beam size but by forward scattering and back scattering in the photoresist (Proximity effect). A large enough dose of backscattered electrons can lead to complete exposure of resist over an area much larger than defined by the beam spot. The scattering is small at high

electron energy. However it's an inefficient process due to the inefficient transfer of momentum from the electron beam to the material. A line width $< 10\text{nm}$ is the smallest feature size patterned by a beam at 100 keV and 3 nm spot size (Vistec VB6 HR).

In the development process (Figure 2.2 (2)) the part of the resist film is removed and cut out the structure in it. In optical lithography we use the negative resist. This means the resist film under UV light exposure is hardened hence stays on the substrate after development. In EBL we use positive resist. The resist under exposure of e-beam is removed after development. The resist film with the structures cut out of it serves as a shadow mask for metal deposition. The metal is deposited on the substrate where it is not covered by the resist as shown in Figure 2.2 (3). Elsewhere the metal is deposited on the top of the resist and is lift off when the resist is solved into warm acetone as demonstrated in Figure 2.2 (4).

Following we give the detailed parameters, which we use for each fabrication step.

Optical lithography

A negative photo resist (ma-N-415, Micro Resist Technology, Germany) is spin-coated (4000 rpm, 40 s) on the substrate followed by baking at 90°C for 90s. A resist layer of $2\ \mu\text{m}$ thickness is obtained. An UV mask aligner (SUSS MJB3, Karl Süss KG-GmbH & Co.) with a Hg lamp (365 nm wavelength) is used for the exposure. The UV light passes through a chromium/glass mask to illuminate the resist for 25 - 30 s. The substrate is then developed in ma-D 332S for ≈ 60 s and rinsed in distilled water (Figure 2.2 (1) & (2)). The smallest structure can be sharply fabricated is 1 - $2\ \mu\text{m}$ for 365 nm light.

Electron beam lithography

JEOL JSMIC 848 scanning electron microscope is used to pattern the structure into e-beam resist. The pattern is designed with the software Elphy Quantum from Raith GmbH. Elphy Quantum communicates with JOEL and controls the movement of the electron beam. The smallest features can be written with JOEL at 35 kV acceleration voltage is ≈ 50 nm. A reduction of the acceleration voltage results in less writing time but decreased resolution.

E-beam resist (PMMA 950 K, Allresist GmbH) is diluted with additional chlorobenzene to obtain the required film thickness of 600 nm. It is spin-coated on the substrate (4000 rpm, 40s) then baked at 175°C for 30 minutes, which leads to a hard PMMA layer. The exposure with electron beam breaks

the PMMA chains, which are then dissolve into an isobutylmethylketone (MIBK) isopropanol mixture (1:3). The developing time is 45 s. The substrate is then rinsed in isopropanol to stop the development. (Figure 2.2 (1) & (2)).

Metal deposition

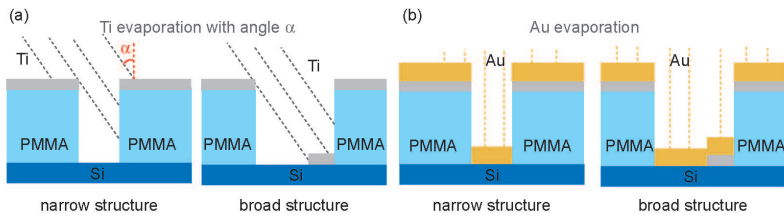


Figure 2.3: (a) The Ti layer is evaporated under an angle of $\alpha \approx 50^\circ$. Therefore no Ti is located in the narrow structure, but it is deposited on the broader structure. (b) The Au layer is evaporated perpendicular to the sample.

After lithography and development process we cut the designed structure from the resist film on the substrate. Metal deposition is done in a vacuum chamber ($\sim 10^{-6}$ mbar) with PLS 500 (Balzers-Pfeiffer GmbH). The substrate is mounted on a sample holder, which can be tilted by up to 50° . It can also be cooled to -5° C with liquid N_2 . Metal is thermally evaporated by an electron gun from a metal source then deposits on the substrate and the resist (Figure 2.2(3)). The deposited film thickness is measured by a calibrated quartz crystal close to same holder. Cooling the sample holder reducing the smearing of the resist pattern by heating due to the metal vapor. It also improves the quality of the deposited metal. In narrow structures it is possible to avoid metal deposition on the substrate by angle evaporation. When the angle is large enough, metal can not reach the substrate behind the shadow of PMMA wall as shown in Figure 2.3a. But in broad structures metal is still deposited. Without angle metal is deposited in small structure too as shown in Figure 2.3b. This way we achieve to deposit Au nano-junction without Ti layer beneath. But elsewhere we have Ti adhesion layer beneath the Au structure layer.

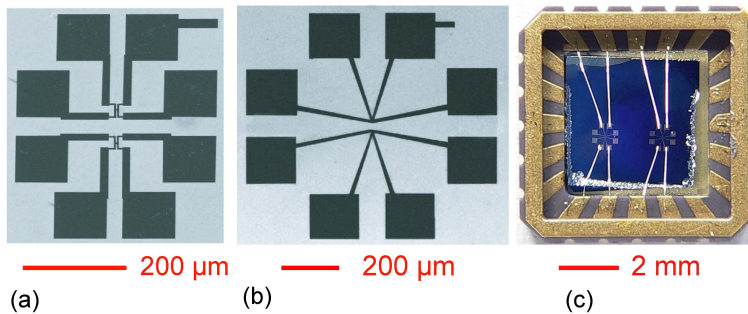


Figure 2.4: The optimized sample structure for one step E-beam lithography and metal deposition fabrication. (a) The optimized structure for EM measurement. (b) Structure with larger contact pads for convenient bonding to chip carrier. (c) The device bonded to chip carrier.

Optimization of the sample structures

In the described two-step lithography the EBL structures form only bad contacts with the UV-defined structures. Quite often one of the four leads does not connected. A possible reason could be that the Au structure defined by UV lithography does not have a sharp and well defined edge. Some remains of the photo resist may stick on the rough surface of the edge, which insulates the two structures. Another reason with the same effect could be that the 6 nm Ti layer are oxidized in the vacuum chamber during evaporation. Finally we might get a TiO isolating layer between the UV and E-beam structures. By evaporating only Au without Ti after EBL, we can improve the number of good devices, but there are still some bad devices. The low success rate in sample fabrication slow down the investigation of EM. In order to solve this problem, we propose to reduce two-step lithography to only one lithography step. The advantage of one lithography step is:

- (a) The risk of bad contacts between UV-defined and EBL structure is eliminated;
- (b) The fabrication time is shorted because the UV-lithography and following metal deposition steps are not needed.

The disadvantage can be:

- (a) The writing time of EBL is longer, because there is more structures and areas to be written with EBL;

- (b) We have to reduce the size of the contact pads to get a reasonable writing time of EBL. This can bring inconvenience to contact the sample with probe station.

After comparing the advantages and disadvantages, we decide to reduce the total structure size to $500 \times 500 \mu\text{m}^2$. The contact pads is reduced to $100 \times 100 \mu\text{m}^2$, which is still possible to be contacted with probe station (Figure 2.4a). For those samples we will bound to chip carrier, we reduce the structure size to $1 \times 1 \text{mm}^2$ and contact pads to $200 \times 200 \mu\text{m}^2$ (Figure 2.4b). The final EBL process after optimization is as following:

- 1. With magnification 250 (writing field $200 \times 200 \mu\text{m}^2$) to write the small structure of the junction to get small junction width around 100 nm. The writing time at 40 pA beam current is around 50 s.
- 2. With magnification 60 (writing field $1 \times 1 \text{mm}^2$) to write the larger structures including the contact pads. Here we use high current to speed up the writing process. The writing time at 8 nA beam current is around 8 and 15 minutes for structures in Figure 2.4a and Figure 2.4b respectively.

After optimization we have reasonable EBL writing time for the new sample structures. The contact pads are still able to be contacted by probe station or bonded to the chip carrier. In Figure 2.4c we show a such fabricated sample bonded on chip carrier. The modification increases yield in sample fabrication to 100% and saves the working time.

2.2 Fabrication of nano-gaps and nano-junctions via electromigration

We explained in Section 1.2.3, to perform EM in the two terminal junctions by simply ramping up the bias often leads to the melting of the junctions. Because the large lead resistances make the junctions effectively current-biased although a voltage is applied. By designing devices with low lead resistances (thick contact layers) or employing software controlled EM can solve the problem. But the both techniques are time consuming and not very stable. In this section we introduce a new principle to perform EM in nano-junctions. We eliminate the lead resistances by lithographically defining four terminals to each junction. By using a fast analog electronic feedback we can accurately control the voltage over the junction during the EM process. Since all instabilities are removed, EM evolves smoothly and nano-gaps are now produced at a yield approaching 100%.

2.2.1 Principle of feedback controlled electromigration in four-terminal nano-junctions

The principle of our EM procedure is illustrated in Figure 2.5a. The voltage drop over the junction U is controlled by a custom-made feedback voltage

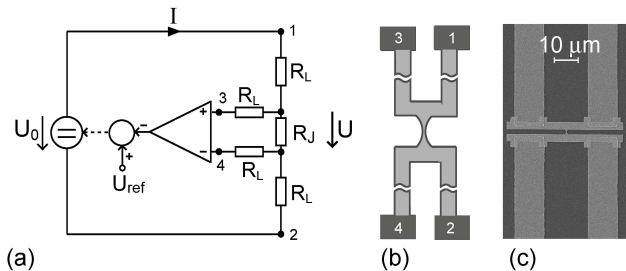


Figure 2.5: (a) The electric circuit for 4-terminal EM. The voltage drop U over the junction is maintained constant and equal to a preset reference value U_{ref} by the feedback system. (b) Schematics of a four-terminal device. (c) SEM micrograph of an actual device.

source and the use of 4-terminal devices. The four terminals are defined by two symmetric pairs of contacts, a left and a right pair (Figure 2.5b,c). On one pair, the bias voltage U_0 is supplied, on the other the voltage drop U over the junction is simultaneously measured. The feedback system compares U with the reference U_{ref} and drives U_0 in such a way that it minimizes the difference between U and U_{ref} . The response time of this feedback system is better than $0.5 \mu\text{s}$ and during operation the difference between U and U_{ref} is negligibly small. Regardless of the actual value of the junction resistance R_J , the feedback voltage source maintains U constant. This removes the thermal instability, because if $U = const$ while R_J evolves to a larger value due to electromigration, the power over the junction is reduced as well. Hence, thermal run-away is now prevented.

2.2.2 Setup

The setup to perform four-terminal electromigration is illustrated in Figure 2.6. The key part of the setup is the four-terminal feedback voltage source, whose function is described in details in Section 2.2.1. The detailed electric diagram of the voltage source can be found in Appendix A.1. In the process of EM it is required to precisely measure the junction resistance

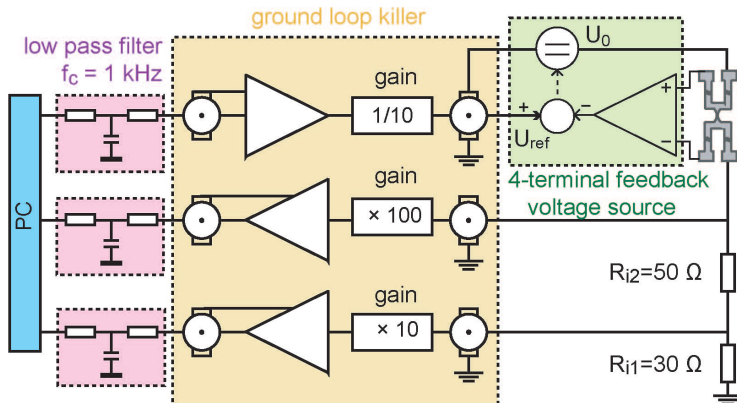


Figure 2.6: The layout of the setup to perform four-terminal EM. Data acquisition is done by a NI board connected to a PC.

value from 5Ω to $10 \text{ k}\Omega$ within 5% error. The junction resistance R_J is obtained by U/I . Hence the range of current I to be measured is between $10 \mu\text{A}$ to 40 mA , a range of more than three decades. The current I is obtained by measuring the voltage drop over the serial resistance R_i . Under the output limitation of the feedback voltage source (maximum output: 17 DCV, 150 mA), we chose $R_{i1} = 30 \Omega$ and $R_{i2} = 50 \Omega$. For large currents, we measure the voltage drop over R_{i1} amplified by a gain of 10. For small currents we measure the voltage drop over $(R_{i1} + R_{i2})$ amplified by gain 100. By using the combination of R_{i1} , R_{i2} and two input channels, we measure $10 \mu\text{A} < I < 1 \text{ mA}$ with one input channel and $1 \text{ mA} < I < 33 \text{ mA}$ with the other. For example if current $I = 10 \mu\text{A}$ we will measure a voltage drop of $100 \times 10 [\mu\text{A}] \times 80\Omega = 80 [\text{mV}]$. Using the input range of 10 V on the NI (national instrument) DAQ-board we are able to measure this signal within 5% error. At the smallest current $I = 1 \text{ mA}$ measured by the other channel, we measure a voltage drop of $10 \times 1 [\text{mA}] \times 30 [\Omega] = 0.3 [\text{V}]$. This signal can be measured in error $< 2\%$ by using an input range of 10 V on the NI board. The channel can be automatically selected by the Labview program according to measured voltage. The amplifier with gain 10 and gain 100 is integrated in the house made Ground Loop Killer (GLK). The circuit diagram of the GLK is shown in Appendix A.2. Besides its function as amplifier, it is mainly used to avoid ground loops in the setup. A ground loop may induce extra noise in the setup, hence degrade the measurement

accuracy. It can be avoided by separating the ground of the signal side from the computer side. Similarly the reference bias U_{ref} is set by PC through GLK to the input of the feedback voltage source with gain 1/10. The GLK improves the signal quality and the accuracy of measurement, especially when the signal is very small. Three low-pass filters (LPF) are used in front of the connections to data acquisition channels. The critical frequency of the LPF is designed to be 1 kHz, since the small voltage modulation (see Section 2.2.3) used in our measurement is less than 1 kHz. LPF filters out the noise generated in the setup above 1 kHz. As in any electronic devices there is a voltage offset in the GLK and the feedback voltage source. By measuring the standard resistors of value between 5 Ω to 15 k Ω with the setup, we are able to calibrate the setup and correct the offset for each input channel in our Labview program. Before each measurement, the setup was checked with standard resistors to verify the accuracy of the measurement. If the measured resistance value deviates 5% from its standard value, the setup has to be re-calibrated.

2.2.3 Resistance evolution during electromigration

With the setup explained in last section, we perform the feedback controlled EM in four-terminal nano-junctions. With our setup a nano-gap is formed by ramping up $U_{ref} = U$ until the junction switches to a high-ohmic state with $R_J > 100$ k Ω at $U \simeq 0.4 \dots 0.6$ V. This is typically performed during a few minutes, but can be done faster or slower with no observable difference. Because we would like to characterize the junction during the evolution of EM, we do not ramp U continuously but in a square-wave pattern [83; 29]. This is illustrated in Figure 2.7. We measure $R_J(U)$ at voltage U (red arrows) and subsequently switch to $U \simeq 0$ to measure the instantaneous linear-response resistance of the junction $R_J^0(t)$ with the aid of a small voltage modulation (lock-in technique). The small voltage modulation is a square wave of 1 kHz and 20 mV amplitude at its mean value of 30 mV. Although $R_J^0(t)$ is measured at $U \simeq 0$, we plot it as a function of U , enabling the comparison of $R_J(U)$ with R_J^0 . The whole process is performed at room temperature under ambient conditions.

Two representative graphs of the evolution of the junction resistance $R_J(U)$ (red) and the corresponding equilibrium resistance R_J^0 (black), measured while ramping up the junction voltage U , are shown in Figure 2.8. The top curves are shifted by three orders of magnitude for clarity. Three regimes (I-III) can be discerned: in regime I, the constant equilibrium resistance R_J^0 shows that geometrically nothing happens. Hence, no mass transport occurs and EM is absent. The sudden, but controlled increase in R_J (empty arrow in Figure 2.8) at $U = 0.15 \dots 0.2$ V signals the transition

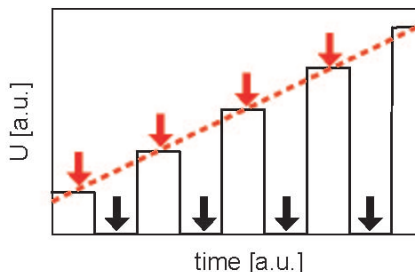


Figure 2.7: The voltage U over the junction is ramped up in a square-wave pattern. At voltage U (red arrows) $R_J(U)$ is measured. At $U \simeq 0$ (black arrow) $R_J^0(t)$ is measured with the aid of a small voltage modulation (lock-in technique). The red dashed line indicates the slope of ramping up in U .

to regime II. Because R_J^0 has increased by typically one order of magnitude, the cross-section of the junction has consequently been decreased. In regime II, R_J grows steadily with increasing junction voltage U , showing that EM is active. There is a second sudden jump (thin arrow in Figure 2.8) occurring typically between $U = 0.4$ V and 0.6 V when R_J approaches a value of ≈ 1 k Ω . In this transition to regime III, R_J grows to large values, typically > 100 k Ω . Due to the large current drop, EM stops at this point leaving the junction 'open'. In regime III, a gap has therefore been formed and the device shows tunneling behavior. SEM micrographs of the devices before EM in regime I ($R_J = 10$ Ω) and after performing EM into regime III ($R_J > 100$ k Ω) are shown in Figure 2.9. They demonstrate that EM tends to form slits of typically smaller than 30 nm in width. The slit is formed after the transition from regime I to regime II, as it is illustrated in Figure 2.9 and observed with SEM. Within these slits, there is a small part (indicated by the circle in Figure 2.9b), which is even narrower. It is here that the gap is formed. The exact gap size, however, can not be resolved by SEM. The SEM micrographs of the same junction in regime II and regime III are very similar.

More than 30 samples with different geometries have been processed with this feedback method and in more than 90% of all devices, EM proceeded smoothly in the manner described before. All characteristic features outlined in Figure 2.8 are present. The feedback method is therefore not only fast. It is very reliable and yields reproducible results. Due to thermal motion, R_J may further increase or decrease with time in the tunneling regime III, even if the bias voltage is removed. After a longer period of time (typically

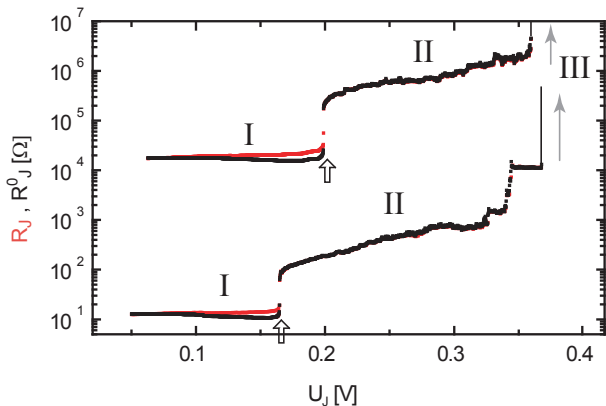


Figure 2.8: Evolution of the junction resistance as function of junction voltage U during four-terminal EM at room temperature for two devices. The upper curves are shifted by three orders of magnitude for clarity. After applying $U \neq 0$ during a short period and measuring the junction resistance $R_J(U)$ (red curve), U is switched back to zero for a similar period of time during which the equilibrium resistance R_J^0 is measured (black curve). A typical cycle lasts 0.1 s. The graph shows both $R_J(U)$ and R_J^0 during the whole process until the junctions switch open into the tunneling regime with $R_J \gtrsim 100 \text{ k}\Omega$. The arrows indicate the transition from regime I to II (empty arrow) and from II to III (thin arrow).

hours), the junctions may be found to have fused together, as proven by a low junction resistance of $R_J < 100 \Omega$. On those devices EM can easily be carried out again.

2.2.4 Controlling of the junction size with electromigration

Before the gaps are formed, EM process can be stopped at any value of junction resistance in regime II by simply removing the applied bias voltage U . The junction resistance decreased few Ω before it approaches a constant value. In Figure 2.10a we show such a time evolution measurement of junction resistance. Where the black dots represent the equilibrium resistance R_J^0 of the junction measured at $U \approx 0$, the red dots correspond to R_J measured at $U > 0$. The ramping up of U is plotted on the top of the graph as the red dots. The black dots in the graph indicates the mean value of the small voltage modulation. The voltage drop over the junction $U \approx 0$

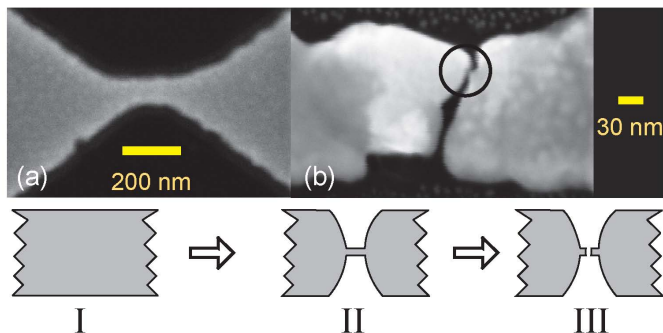


Figure 2.9: Illustration of regime I, II, III and its corresponding SEM micrographs during four-terminal feedback controlled EM. (a) The junction in regime I and (b) in regime II and III. The junctions in regime II and III can not be distinguished on SEM micrographs.

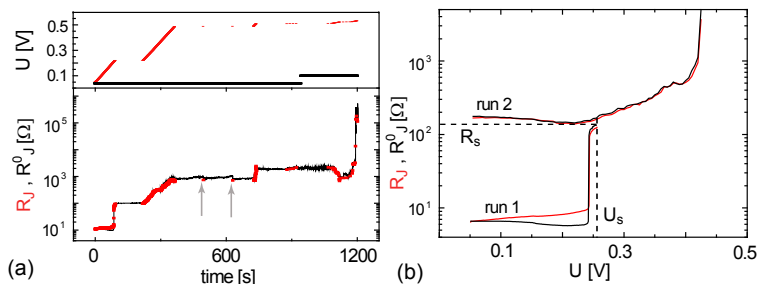


Figure 2.10: (a) The junction resistance R_J (red dots) and R_J^0 (black dots) versus time during an experiment where the ramping up of U is interrupted and set to zero for several times. Junction resistance stays unchanged when $U \approx 0$ in the region of $R_J < 2 \text{ k}\Omega$ (where only black dots are present). (b) EM is stopped shortly after the junction enters regime II. EM can be started again in the junction at the bias U_s and junction resistance R_s , where it was stopped.

is in the resistance evolution where red data points are missing (only R_J^0 is measured). The observation of constant R_J^0 at $U \approx 0$ indicates that the junction is stable for more than 5 minutes when bias is set to zero. R_J^0 tends to decrease slightly (thin arrow) if we apply a pulse (0.1 s) of $U \neq 0$. We estimate that the junctions can stay unchanged for few hours at zero bias, but we did not examine that in our experiments. EM can be started again

by ramping up U in the the junction. This process can be better seen in Figure 2.10b, where two runs of EM are carried out one after another in the same junction with 5 minutes interval. In the first run EM is stopped after it enters regime II. In the second run EM starts till U_s (dashed line) is reached by ramping up of U , where U_s is the voltage when EM was stopped in the last run. Similarly R_J starts to increase from $R_J \approx R_s$ (dashed line), where R_s is the end value of R_J^0 in the first run, where EM was interrupted. As expected R_J evolves smoothly in regime II without any sudden jump. This implies that in regime II a relation exists between the junction resistance and bias voltage, at which EM sets in. Therefore the junction size, i.e. junction resistance can be controlled by the voltage U applied over it. The stability of our EM process extends its application to the formation of nano-contacts. Any junction resistance R_J in regime II can be achieved, i.e. from 150 Ω to 1 k Ω . With the expression of Sharvin's resistance in Equation (1.4), we estimate the size of the formed nano-contacts from few nanometer to few atoms across respectively. At a junction resistance $R_J > 1$ k Ω , the junction has only few conducting channels. Because of the mobility of Au atoms at room temperature, the junction is not stable. It is very likely that the constriction continuously reconfigures, as we observed on some samples, where R_J increases to an open state even if $U \approx 0$. The same phenomenon is observed and studied by other groups. They found that the junctions formed in this way have the advantage to prevent the formation of gold cluster in the gap [54]. EM process at $U \approx 0$ in high ohmic junction is slowed down. The time to reach a junction conductance less than 1 G_0 may vary between tens of minutes to tens of hours.

2.2.5 Electromigration in Co junction

Inspired by the 'ballistic magnetoresistance' experiments [84; 85] in nano-contacts, we tried feedback controlled EM in four-terminal Co junctions. The evolution of the junction resistance R_J and R_J^0 (high bias and zero bias resistance) as a function of the applied voltage U is similar to the Au junctions. In Figure 2.11 we show data for the EM process in a Co junction. (a) shows the evolution of R_J and R_J^0 versus U and (b) is R_J and R_J^0 as a function of time t . The ramping up of voltage U was varied several times in order to observe the stability of R_J and R_J^0 under constant U . The ramping up of U as a function of time is shown in Figure 2.11b the lower panel. We observe that the EM process is slightly differently in Co junctions. Compare to EM in Au junctions the first jump of R (empty arrow in Figure 2.11), which indicates the start of EM, is much larger in Co junction. EM occurs also at slightly higher bias ($U \approx 0.25$ V) than in Au junctions (≈ 0.2 V) with similar cross sections. The possible explanation is that, Co atoms have

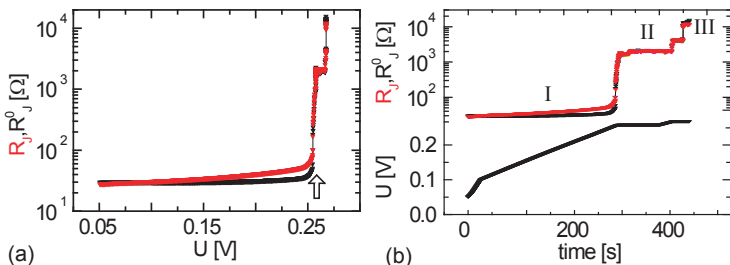


Figure 2.11: EM in Co junction. R_J and R_J^0 are junction resistance measured at high bias and zero bias (see Section 2.2.3). (a) Evolution of R_J and R_J^0 during EM as function of U . (b) The upper panel is the evolution of R_J and R_J^0 during EM as function of time t . I, II and III indicate the different regimes of the junction. The lower panel is the bias U over the junction as function of time t . At constant U the junction is stable as demonstrated by constant R_J and R_J^0 .

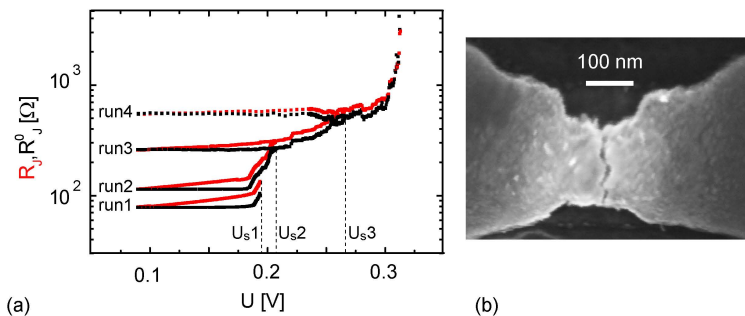


Figure 2.12: (a) EM can be stopped and started again in Co junction for several times (four ‘runs’). In the next ‘run’ R_J and R_J^0 starts at the end value of the last ‘run’, EM sets in at the bias U_s where EM stops in the last ‘run’ (b) SEM image of a Co junction after feedback controlled EM.

a lower mobility than Au atoms. Hence larger current densities (\propto electron wind force) is required to trigger EM in Co junction. When ramping up of U is interrupted several times during EM, we observe the junction is stable under constant U as indicated by constant R_J^0 . The junction resistance start to increase after U increases again as shown in Figure 2.11b. Similar to Au junctions multiple ‘runs’ of EM can be carried out in Co junction, which are shown in Figure 2.12a. The time between each ‘run’ is about 2

to 5 minutes. In the next ‘run’ R_J and R_J^0 starts at the end value of the last ‘run’, EM sets in at the bias U_s (dashed lines) where EM stops in the last ‘run’ (Section 2.2.4). An SEM image of a Co junction after feedback controlled EM is shown in Figure 2.12b. More experiments of EM in Co junctions should be done in order to gain more experience with this system.

2.2.6 Conclusions

We have developed a fast, yet highly reproducible method to fabricate metallic electrodes with nanometer separation or nano-junctions with one to few hundred conducting channels using EM under ambient conditions. We employ four-terminal, instead of two-terminal devices in combination with fast ($< 1 \mu\text{s}$) analog feedback to maintain the voltage U over the junction constant. In this way, the previously reported thermal runaway is avoided. Three regimes are observed. In regime *I* ($U \gtrsim 0.2 \text{ V}$) EM has not set in evidenced by constant R_J . In regime *II* ($0.2 \text{ V} \lesssim U \lesssim 0.6 \text{ V}$) EM processes stably with increasing junction voltage U . EM can be interrupted and start again in regime *II*. In regime *III* the gap is formed. With our procedure, a stable, electromigration-dominated formation of nano-junctions and nano-gaps is observed with a yield $> 90\%$. The smooth EM is carried out in Co junctions with similar behavior to the Au junctions.

2.3 Temperature dependence of the junction resistivity

In order to gain the temperature information during EM with measured R_J and R_J^0 , we need to know how the junction resistance responds to temperature, i.e. the temperature dependence of the junction resistivity. In a diffusive metal the resistivity $\rho(T)$ at temperature T can be expressed as $\rho(T) = \rho(T_0) + \alpha\Delta T + \beta(\Delta T)^2$. The T^2 dependence is dominant at low temperatures below the Debye temperature (170 K for Au [86]). The temperature in our junctions is much higher than 170 K, therefore we can simplify the equation and take only the term linear in ΔT . To determine α , the resistivity ρ of a homogeneous thin gold film of similar thickness to our gold junctions was measured as a function of temperature T in the vicinity of $T = 25^\circ\text{C}$ [87; 88; 83]. The gold stripe of $50 \mu\text{m}$ length, $1 \mu\text{m}$ width and 45 nm thickness is EBL fabricated (Section 2.1) on the same Si wafer as we used for EM samples. Four contact pads are designed in order to do four-terminal resistance measurement. The sample is bonded on a chip carrier, which can be installed in a chip carrier holder of a ‘dipstick’ cryogenic probe head. A dewar is filled up to one third with liquid N_2 to obtain a temperature gradient from 77 K to 300 K above the nitrogen liquid. We move the cryogenic stick to a certain height above the liquid N_2 surface

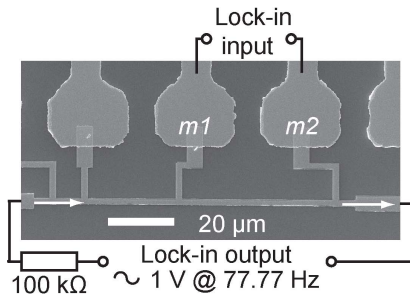


Figure 2.13: SEM image of the sample and its connection to Lock-in amplifier for low temperature resistivity measurement.

and wait for long enough time to get a thermal equilibrium of the sample and its environment. The temperature of the chip carrier is measured with a Si-diode and recorded in real time by the Labview program. The resistance of the sample (gold strip) is precisely measured with a four-terminal Lock-in technique. An AC signal of 1 V and 77.77 Hz is taken from the Lock-in output as power source. It supplies a 10 μA current passing through the sample and a serial resistance $R_i = 100 \text{ k}\Omega$. The resistance R of the gold film is around 4 Ω , which is very small compare to $R_i = 100 \text{ k}\Omega$. Hence we assume the current does not change during the measurement when R changes at different temperatures. A SEM image of the sample and its connection to Lock-in amplifier is shown in Figure 2.13. The voltage drop over the sample is measured through two contact pads (m_1 and m_2 in Figure 2.13) with the input of the Lock-in amplifier to calculate R . The measurement is repeated for 8 different temperatures between 77 K and 300 K. In order to relate the measured R_J and R_J^0 during EM, we plot $\Delta R/R_0 = (R(T) - R(T_0))/R(T_0) = (\rho(T) - \rho(T_0))/\rho(T_0)$ as a function of $\Delta T/T_0$ in Figure 2.14 the black dots. In the vicinity of $T_0 = 25^\circ\text{C}$ we estimate the slope of measured data points as red dashed line in Figure 2.14. It allows us to estimate the linear increase of $\rho(T)$ with T in the vicinity of T_0 . The slope of measured data is 0.9 ± 0.1 , which is smaller but close to the slope of 1.15 for bulk material [89]. This means the resistivity of our Au film changes slower with temperature as in bulk gold. Therefore in our Au film $\rho(T)$ increases with T according to $(\rho(T) - \rho_0)/\rho_0 = 0.9 \cdot \Delta T/T_0$. Here, ρ_0 denotes the resistivity at $T_0 = 25^\circ\text{C}$. This relation can be used to calibrate the temperature dependence of our junction resistance. Later we will use it to estimate the temperature in the junction with measured R_J

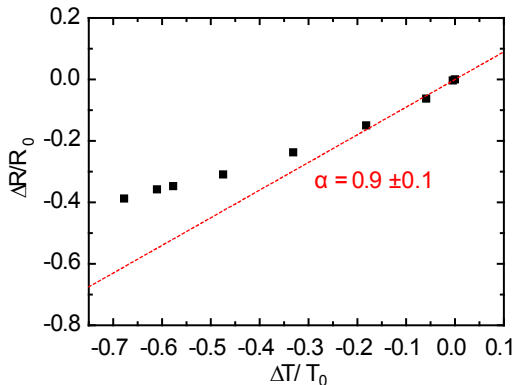


Figure 2.14: Temperature dependence of resistivity in a 45 nm thick gold film. Black dots are measured data points. The red dashed line is the slope of the data points at close to $T_0 = 25^\circ\text{C}$, i.e. $\Delta T = T - T_0 = 0$. We found the slope $\alpha = 0.9$

and R_J^0 during EM.

2.4 Noise measurement

In our experiment we investigate the resistance fluctuation (noise) in very small junctions, i.e. from 150 nm size to few atoms across. There are two types of samples used in order to compare the noise behavior in junctions fabricated with different technique. Two representative examples of EM junctions and MCBJs are shown in Figure 2.15. They are both fabricated using electron-beam lithography and metal deposition in a lift-off process (see Section 2.1). In both cases Au wires with narrow constrictions with typical dimensions of 200 nm in length and 100 nm in width are defined first. Each wire has two contacts on each side of the junction, enabling us to accurately measure the electrical resistance of the junction in a four-terminal experiment. The Au wires are fabricated on oxidized (400 nm) Si substrates for EM junctions, and for MCBJs on a flexible substrate, onto which a several μm thick insulating polyimide layer is cast [40]. To form an EM junction the four terminals are used in an automatic feedback controlled EM process which continuously shrinks the wire constriction down to few nanometer sized junctions as described in Section 2.2. In MCBJs the wire constriction is first transferred into a suspended bridge by etching the underlying polyimide layer in an oxygen plasma (Figure 2.15b). By bending the substrate the

constriction can be narrowed in a controlled manner [90; 91; 3]. The details about MCBJ setup and its working principle is described in Appendix B.1. Before narrowing the constrictions, the as-fabricated devices have a junction

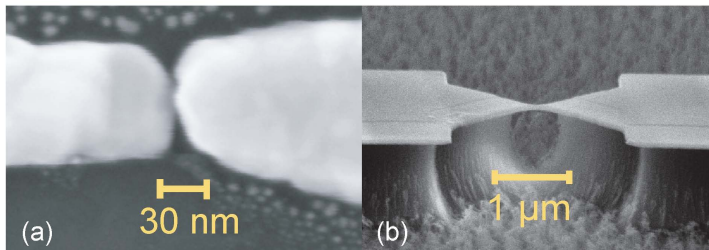


Figure 2.15: SEM images of (a) an EM junction and (b) a suspended bridge device used in the MCBJ setup.

resistance R_J of around $1 - 10 \Omega$ at room temperature as determined in a four terminal experiment. The two-terminal resistance $R = R_J + 2R_L$, which includes the lead resistance R_L on both sides, amounts to as much as 250Ω . Because $R_L \gg R_J$ in virgin devices, the feedback-controlled process is mandatory to initiate a nondestructive narrowing by EM [92]. In voltage-biased controlled EM, in which the voltage over the junction is stabilized by a fast analog feedback, a narrowing sets in at a voltage of $\gtrsim 0.2 \text{ V}$. The junction resistance R_J then rapidly evolves from a few Ohms to $\approx 100 \Omega$. EM is stopped as soon as $R_J \approx 100 \Omega$. The sample is moved to the noise measurement setup to measure the noise. In this regime of active EM, R_J can further be increased into the $k\Omega$ -regime by increasing the junction voltage with a two terminal low noise voltage source. We emphasize that we do not measure the noise while EM proceeds. After narrowing the constriction at a ‘large’ voltage we switch the applied voltage back to values $\lesssim 0.2 \text{ V}$ in measurement. There we perform the noise measurements, during which the junctions remain unchanged. In contrast to EM junctions, MCBJs have the advantage that the junction size can be changed with an independent control parameter by mechanical bending. This allows us to change the junction diameter while monitoring noise simultaneously. In EM junctions noise is measured for $100 \Omega < R_J < 12.9 \text{ k}\Omega$. In MCBJs the junction size can be changed reversible and repeated many times. A large amount of noise data can be collected in a wide resistance range from 10Ω to $10 \text{ k}\Omega$.

2.4.1 Measurement setup

We perform noise measurements at room temperature in a four-terminal setup schematically shown in Figure 2.16. An adjustable low noise *DC* volt-

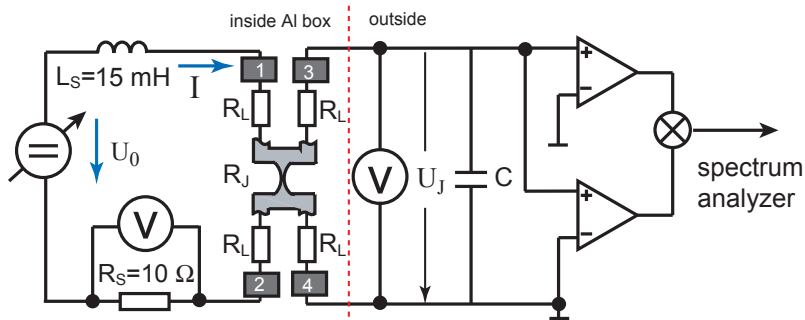


Figure 2.16: The schematics of the electric circuit used to measure the noise. R_L denotes the resistance of each lead in the four-terminal setup and C summarizes the total capacitance of the preamplifier and the connecting cables. The inductor L_S is used to separate the *AC*-noise measurement on the right from the *DC*-biasing on the left.

age source U_0 is connected via a series inductor L_S and a series resistor R_S to contacts 1 and 2 on the left side, driving a *DC* bias current I through the junction. $R_S = 10 \Omega$ is used to measure I , while $L_S = 15 \text{ mH}$ serves to decouple *AC* from *DC*. The impedance of the inductor prohibits the shunting of the *AC* voltage fluctuations (noise). This only works for $\omega L_S > R_J$ (ω is the angular frequency $= 2\pi f$), defining a lower cut-off frequency for the useful frequency window. The frequency-dependent voltage noise is simultaneously measured on the terminals 3 and 4 and fed into two low-noise preamplifiers (EG&G 5184) and a spectrum analyzer (HP89410A). Here, the effective input capacitance C is diminishing the signal at high frequencies defining an upper cut-off for the frequency window through the relation $1/\omega C > R_J$. For a typical junction resistance R_J of 100Ω and effective capacitance $C \approx 1 \text{ nF}$, the useful frequency window spans approximately three orders of magnitude, i.e. $1 \text{ kHz} < f < 1 \text{ MHz}$. We describe the f -dependence of the circuit analytically in Section 2.4.2 and use this model to fit the total capacitance which contains parts of the Si chip, the connecting wires and the amplifiers. When measuring noise, the two preamplifiers measure the same fluctuating signal in parallel. The spectrum analyzer is operated in the cross-spectrum mode and determines the Fourier transform

of the cross-correlation (see Section 1.3.1) signal from the two amplifiers:

$$S_V(f) := 2 \int_{-\infty}^{\infty} e^{i2\pi ft} \langle \delta U_1(t + \tau) \delta U_2(\tau) \rangle_{\tau} dt \quad (2.1)$$

where $\delta U_{1,2}(t)$ denotes the time dependent deviations from the average value of the junction voltage U_J measured on amplifier 1 and 2. $\langle \dots \rangle$ refers to averaging over the time interval τ . This signal is equivalent to the voltage noise-power spectral density. The correlation techniques can eliminate the voltage noise originating from the two amplifiers because the two amplifiers are independent. The current noise from the amplifiers, however, can not be eliminated. But they are very small of the order of $80 \text{ fA}/\sqrt{\text{Hz}}$ for our low-noise preamplifiers (EG&G 5184) [58].

The voltage fluctuations which we want to measure are small signals, in the $\approx nV/\sqrt{\text{Hz}}$ range. A low noise DC voltage source was especially build in-house to power the junction. The noise of our voltage source is below $100 \text{ pV}/\sqrt{\text{Hz}}$ at 10 kHz. The details of the low-noise voltage source is presented in Appendix A.3. All the elements on the left side of the circuit in Figure 2.16, including the junctions are enclosed in a grounded aluminum box to prevent electromagnetic pick-up from the environment. To measure the voltage drop over R_s and R_J , we use a multimeter and a DC voltage preamplifier. These instruments induce extra noise to the noise signal, which we want to measure. In order to avoid the noise from those instruments, we build up switches in front of each instrument. The switches are switched off to disconnect the instruments including the ground for 30 s when the noise is measured. During this 30 s interval R_J is not able to be monitored. But before and after the 30 s interval we measure R_J and compare the values. If the junction is stable during the 30 s interval, we should have the same value of R_J before and after the noise measurement. We consider the noise data measured in a stable junction is valid, and will be taken for further analyze. If the before and after values of R_J are not same due to EM or thermal diffusion in the junction, the measured noise data will not be used for analyze.

2.4.2 Setup calibration

We discussed in last section , in our setup there is cut-off of signal at low and high frequency ends. To calibrate the setup we measure the thermal noise of a commercial metal thin film resistor at room temperature. In Section 1.3.2 we introduced the thermal noise, which is the intrinsic current noise and exists in any conductors. The thermal voltage noise of a resistor of value R is given by $S_V = 4k_BTR$ (see Equation (1.20)), which is white

in a frequency range where we calibrate our setup. Due to the frequency dependent elements in the circuit and the preamplifiers, the noise signal is attenuated. The attenuation factor A has two components, $A = A_1 \cdot A_2$. A_1 is determined by the two circuits in Figure 2.16 parallel to R_J , the one with the inductor L_s on the left and the one with the capacitor C on the right. We redraw the equivalent circuit of the setup in Figure 2.17 with

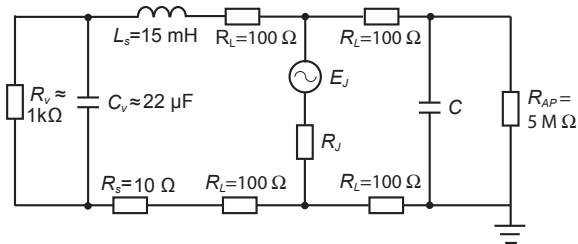


Figure 2.17: The equivalent circuit of noise measurement setup. We consider only the voltage noise in the junction as noise source E_J . Here R_V and C_V are internal resistance and capacitance of low-noise DC voltage source. R_{AP} is the input resistance of the preamplifier. Other symbols have the same meaning as in Figure 2.16

noise source E_J , which represents the voltage noise over R_J . The low-noise DC voltage source has an internal impedance of less than 5Ω ($R_V // C_V$), hence we can ignore it and replace it with a conducting wire. The input resistance of the preamplifier R_{AP} is very large compared to $1/\omega C$, and can therefore be treated as open. We assume that $R_L \ll 1/\omega C$, so that we can write $2R_L + j\omega C \approx j\omega C$. We obtain for this attenuation factor A_1 :

$$A_1 = \left| \frac{1}{1 + i\omega C R_J + 1/(i\omega L_s/R_J + R_\Sigma/R_J)} \right|^2 \quad (2.2)$$

where $R_\Sigma = 2R_L + R_s$. The second part A_2 is due to the frequency-dependent gain of the amplifiers. We have carefully measured this dependence between $f = 1\text{Hz}$ and 1MHz and found that the high-frequency roll-off can accurately be modeled by a first-order low-pass filter with a cut-off frequency of $f_c = 840\text{kHz}$ as shown in Figure 2.18a. Hence, A_2 is given by:

$$A_2 = \left| \frac{1}{1 + i2\pi f/f_c} \right|^2 \quad (2.3)$$

The inductance L_s is measured in the frequency widow of 1kHz to 1

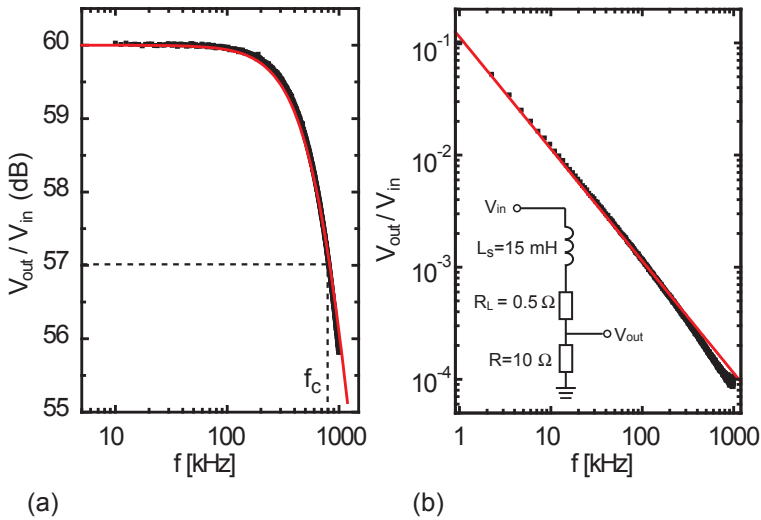


Figure 2.18: (a) Frequency dependence gain of the amplifier (black curve). The red curve is the modulation of a first-order low-pass filter with a cut-off frequency of $f_c = 840$ kHz. The cut-off frequency is indicated by dashed lines. (b) Inductance L_s measured in frequency window of 1 kHz to 1 MHz (black curve). The red curve is the modulation with $L_s = 15$ mH. In the inset is the circuit used to measure it, where R_L is the DC resistance of the inductor L_s .

MHz with spectrum analyzer as shown in Figure 2.18b. The circuit used to measure it is shown in the inset. The red curve is the simulation with $L_s = 15$ mH. Now all parameters L_s , R_L , R_s and the overall gain are accurately measured except C . We therefore determine the capacitance C by fitting the frequency dependence of the measured thermal noise $S_V(f)$ to the expected value $4kTRA_1(f)A_2(f)$. A consistent single value of $C = 270$ pF has been found for different junction resistances. This calibration procedure is shown in Figure 2.19. In Figure 2.19a the frequency dependence of the measured thermal noise is shown for different calibration resistances R ranging between 10Ω to $10 \text{ k}\Omega$ which were used instead of a real junction. One can see that the f -dependence is very strong for large junction resistance values, whereas a flat f -independent part is clearly visible in the opposite case. The expected noise according to $4kTRA_1(f)A_2(f)$ is plotted as dashed black curves in Figure 2.19a. A very good agreement with the measured data is obtained. In Figure 2.19b we display the corrected data, i.e. the measured

noise divided by the attenuation factor A . This procedure works very well in the shaded frequency window over the whole resistance range as evidenced by the flat noise plateaus that coincide with the expected thermal noise (horizontal lines). For the $1/f$ noise study we will therefore restrict the frequency window to the shaded region of $30 \text{ kHz} < f < 400 \text{ kHz}$.

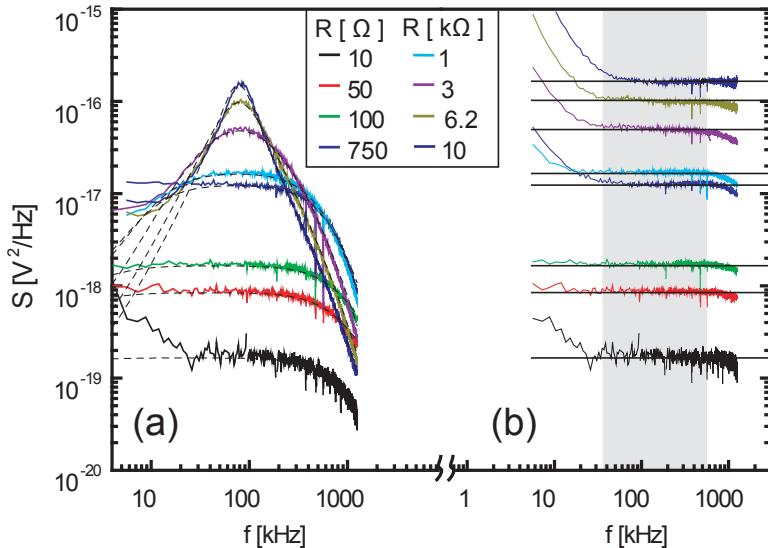


Figure 2.19: (a) Calibration of the setup by measuring the thermal noise of eight commercial metal-film resistors with resistance ranging from $10 \text{ } \Omega$ to $10 \text{ k}\Omega$. The dashed curves are calculated taking the frequency dependence of the circuit and gain of the amplifiers into account. In (b) the measured thermal noise is corrected for the known frequency dependence of the circuit and amplifier gain. The horizontal lines mark the theoretical thermal noise of $4kTR$. In the shaded region the corrected noise is frequency independent and coincide with the expected thermal noise values. This frequency interval is used to measure the $1/f$ noise in nano-junctions.

Chapter 3

Physical properties of nano-junctions

During a well controlled EM process, some physical properties related to EM can be studied, such as the temperature evolution in the junction during EM. This is important, because EM induced nano-gaps have been employed for research on single-molecule electronics. In many experiments molecules are first assembled on the nano-bridge, EM is then performed to form the nanometer sized gap and trap the molecule [44; 46; 45; 48; 93; 94]. Since some molecules are sensitive to temperature, if the temperature in the junction is too high during EM, the molecules deposited on it may get damaged. Furthermore, we take advantage of the stable, feedback controlled four-terminal EM to continually reduce the junction size by EM (Section 2.2.4). This offers the possibility to study the physical properties of nano-junctions, such as electron transport mechanism and resistance fluctuations (noise), scaling with junction size and junction resistance. In this chapter the results of our investigations in nano-junctions will be discussed.

3.1 Temperature in nano-junctions during electromigration

In order to gain the temperature information in the junction, we use the junction resistances $R_J(U)$ and R_J^0 [29; 83]. As we mentioned in Section 2.2.1, R_J^0 is measured in the linear-response regime, it depends on the junction geometry and the resistivity, which is a material parameter. The difference between $R_J(U)$ and R_J^0 can be related to a temperature difference ΔT alone if two conditions hold:

- i) the geometry does not change in between subsequent measurements of $R_J(U)$ and R_J^0 (small time delay);
- ii) the elastic scattering length L_m is much smaller than the length of the junction L (diffusive regime, see Section 1.1.1).

In this case, we may write $R_J(U) = R_J^0 \cdot (1 + \alpha\Delta T)$, where α is a constant which has been measured independently. This we have done in Section 2.3. With the measured temperature dependence of the junction resistivity (Section 2.3), we will estimate the temperature in the junction during EM with measured R_J and R_J^0 . In Figure 3.1 we present two typical measurement curves of R_J and R_J^0 during EM. I, II and III denotes three different regimes in the junction when EM is going on (see Section 2.2.3). The dashed lines are reference lines for constant power value dissipated in the junction through Joule heating, i.e. $P = U^2/R_J = \text{const}$. The different power dissipation values are represented with colors. From the same data we plot $(R_J - R_J^0)/R_J^0$ as a function of the applied junction voltage U in Figure 3.2. We clearly see that R_J increases above R_J^0 in regime I, but remains similar to R_J^0 in regime II. Next we discuss regime I and regime II separately.

3.1.1 Temperature in regime I

In regime I the junction dimension is much larger than the electron elastic scattering length L_m (typical 50 nm at 25°C [86]). The junction is in the diffusive regime. The time delay between R_J and R_J^0 measurements is very small, typically 0.5 s. In this regime EM has not yet set in as evidenced by a constant R_J^0 . The geometry of the junction stays unchanged in regime I. Therefore we can relate the difference between $R_J(U)$ and R_J^0 to a temperature difference ΔT . Using our calibration, which is $(R_J - R_J^0)/R_J^0 = (\rho(T) - \rho_0)/\rho_0 = 0.9 \cdot \Delta T/T_0$ (see Section 2.3), we now convert the pronounced increase of $R_J(U)$ in regime I (see Figure 3.2a) into temperature T . This is shown in Figure 3.2b. The upper and lower temperature plots are corresponds to the upper and lower data sets in (a). We see that ΔT reaches maximum values of 180 °C and 90 °C respectively, the former being clearly ‘unhealthy’ for molecules if they are already present during the junction formation. We emphasize that, in regime I, EM has not yet set in. This indeed proves that a substantial temperature increase is required for EM to be initiated. This has been anticipated before [56; 55; 29; 57] and is confirmed here.

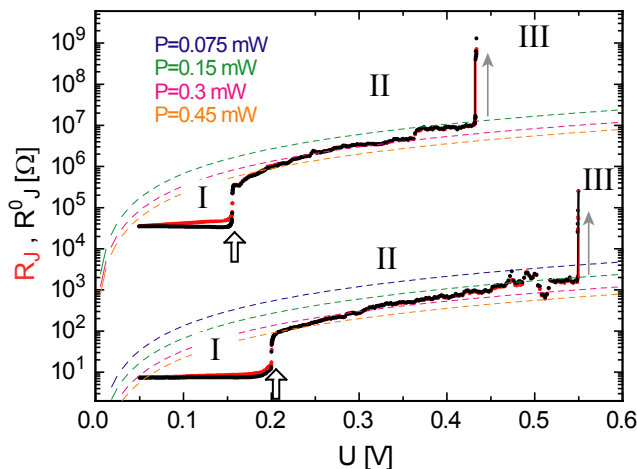


Figure 3.1: Evolution of the junction resistance as function of junction voltage U during four-terminal EM at room temperature for two devices. The upper curves are shifted by four orders of magnitude for clarity. The graph shows both $R_J(U)$ and R_J^0 in regime I and II until the junctions switch open into regime III. The dashed curves are drawn as reference lines and correspond to constant power values, i.e. $P = U^2/R_J = \text{const.}$ P decreases from bottom (0.45 mW) to top (75 μW).

3.1.2 Temperature in regime II

Once regime II is entered, the difference between R_J and R_J^0 becomes very small (see Figure 3.2a). However EM still takes place as evidenced by an increase in both R_J and R_J^0 (Figure 3.1). At first sight, this suggests that EM proceeds close to room temperature. While this conclusion is tempting, it rests on the assumption that the elastic scattering length L_m remains shorter than the effective junction length l in regime II as well. However, after entering regime II, the junction has narrowed and effectively shortened. In fact, SEM images such as in Figure 2.9 indicate that the size of the slit is smaller than 30 nm, a value close to the electron mean free path in gold (We estimate a mean-free path of 20 nm from the measured sheet resistance $R_{\square} \sim 1 \Omega$ of similar Au films using Durde's formula). This would then imply that a cross-over in the transport regime has taken place, from diffusive, with $L_m \ll l$, to quasi-ballistic, with $L_m \simeq l$. In a quasi-ballistic regime, the resistance depends only slightly on temperature. To elaborate on this, it is interesting to compare absolute numbers for dissipation. Let us focus on

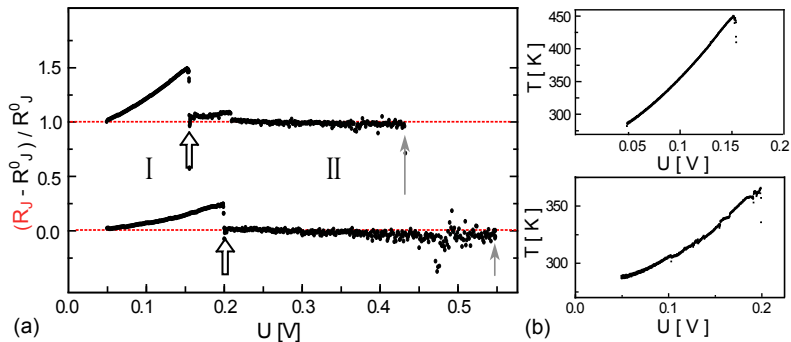


Figure 3.2: (a) The difference of the junction resistance $R(U)$ and R_0 ($U = 0$). The two curves correspond to the same process as in Figure 3.1. The upper curve is shifted by 1 for clarity. (b) The development of local temperature in the junction before EM begins. The temperature plots are correspond to the measurement in (a). The procedure is carried out at room temperature.

the upper set of data in Figure 3.1. In regime I, the power over the junction increases to a maximum value of 8 mW, yielding a large temperature increase of up to 150 °C. At the transition to regime II, the power P jumps back by an order of magnitude to < 1 mW, while the electrical resistance increases by an order of magnitude as well. Interestingly, with the increase in the electrical resistance R_j^0 , the thermal resistance (related to electrical resistance through Wiedemann-Fanz law) increases as well. Because both effects (P decrease and R_j^0 increase) are of similar amplitude, it is likely that T is still enhanced compared to room temperature in regime II. However the temperature may decrease due to the cross-over to the quasi-ballistic regime. In the very small constriction where the gap is formed (Section 2.2.3), the electron pass through the junction ballistically, the power is dissipated at both ends of the small constriction instead of in the constriction itself as shown in Figure 3.3b. If this is the case, we can assemble the molecules in the junction after EM enters regime II, then process EM to open a gap and trap the molecules. In such a way the molecules are ‘safe’ and can be contacted and measured properly. To measure the temperature in regime II more accurately, we need to employ some other methods or ideas. Now we can at least understand why our ‘thermometer’ ceases to work in regime II, because the resistance depends only slightly on temperature in the quasi-ballistic regime. The resistance of a quasi-ballistic constriction is independent of the resistivity ρ and the mean free path L_m , which are temperature dependent. Only the

size of the constriction define the number of the electron transport channels in the constriction (see Section 1.1.2).

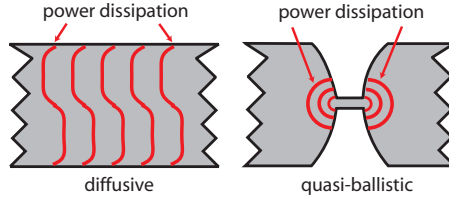


Figure 3.3: Illustration of power dissipation in diffusive and quasi-ballistic wires. In diffusive wires the power is evenly dissipated in the whole volume of the wire. In quasi-ballistic wires the power is dissipated at both end of the constriction where the scattering takes place.

3.1.3 Comparison of electromigration in two types of samples

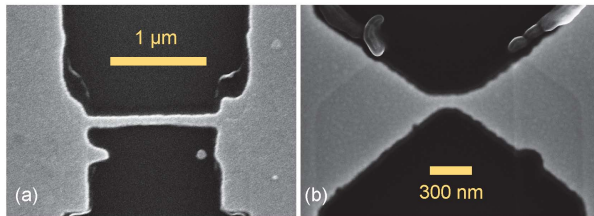


Figure 3.4: SEM image of (a) ‘straight wire’ and (b) ‘bow tie’ type samples used for EM measurement.

EM is carried out on two types of samples, ‘straight wire’ and ‘bow tie’ types (SEM image in Figure 3.4). We use type *A* for ‘straight wire’ and type *B* for ‘bow tie’ type samples. The size of the junction varies in width from 80 nm to 200 nm and thickness from 20 nm to 45 nm. We write the critical temperature and critical current density as T_c and j_c . Note the definition of j_c is not same as j_c defined in Section 1.2.2. Here they are defined as the temperature and current density in the junction, at which EM induced atom flux starts to be visible in the change of junction resistance R_J . In

Figure 3.5a we illustrate the definition of U_c in the graph of R_J and R_J^0 as function of U in regime I. We define U_c as the critical bias voltage, at

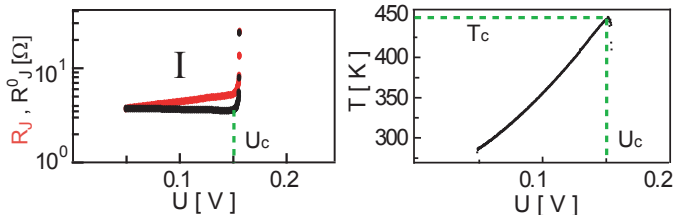


Figure 3.5: (a) U_c is defined as the bias voltage at which EM sets in and results in visible increase in R_J and R_J^0 . j_c is the current density at U_c . (b) T_c is the temperature in the junction at U_c .

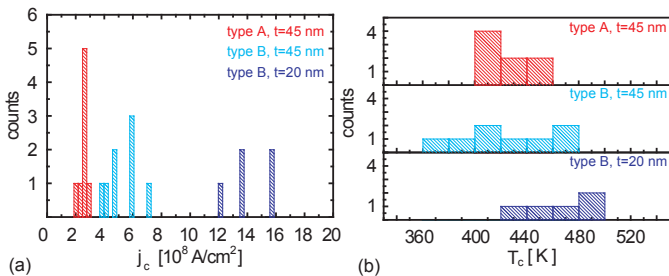


Figure 3.6: (a) Histogram of measured j_c . (b) Histogram of measured T_c . The red bins are for type A, light blue and blue bins are for type B samples.

which R_J and R_J^0 start to increase. j_c is then the current density and T_c (Figure 3.5b) the temperature at U_c . The cross section of the junctions are estimated from the SEM images. The histogram of measured j_c and T_c in 21 junctions are shown in Figure 3.6. The red bins are for type A samples, the light blue and blue bins are for type B samples. The values and the dimensions of the junctions are listed in Appendix D. We observe in type A junctions j_c is lower than in type B junctions. In type B samples j_c is lower in 45 nm thick junctions than in 20 nm thick junctions. However there is no significant difference in T_c observed between different samples. This indicates that EM starts at a certain T_c regardless of the dimensions and shapes of the junctions. To explain the difference in j_c , we consider

the thermal conduction in the junctions. In type *B* junctions the thermal conduction is better because of its shorter distance to large contacts. Hence j_c is larger in type *B* to heat up the junctions to same T_c as type *A*. In same type of samples the difference in j_c may come from the different crystalline structures in the junctions. The junctions with smaller thickness is easier to form grains which expand over the whole thickness. This makes the gold atoms difficult to diffusion through, because less grain boundaries are available. Hence larger j_c , i.e. larger electron wind force, is required to trigger EM.

In EM formed gaps we observe that the gaps are not formed in the middle, but shifted towards cathode side. In type *A* of samples, the gaps are formed in the junctions. In type *B* of samples the gaps are formed at the end of the junctions even in the contacts. If we look at SEM images of two formed gaps shown in Figure 3.7, we see enlarged grains, few are spanned

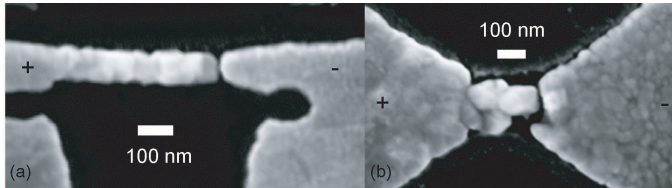


Figure 3.7: SEM images of the gaps formed in ‘straight wire’ and ‘bow tie’ type junctions. The gaps are shifted to the anode side. (a) The gap is in the junction if the junction is long. (b) The gap is at the end of the junction if the junction is short.

over the whole width, in the middle of the both junctions. We know grains enlarge at enhanced temperature. The grain size in the junctions indicate the temperature distribution there. As we expected the maximum temperature is in the middle where largest grains are. If there were no large grains forming, EM would occur there and form the gap in the middle. Because of large grains formed in the middle, the gaps are shifted to the cathode (upstream) side, where temperature is enhanced and grain boundaries are still available for gold atoms to diffusion through. In the middle of the junctions EM induced gold atom flux is slowed down and deposited there. In Figure 3.7 we can see the pile up of materials in the middle of the junctions as bright color in the SEM images. In type *B* samples the grains are large in the junctions and also the nearby area in the contacts. The grain boundaries are only available at the end of the junction. Therefore in type *B* samples gaps are often formed at the end of the junctions (Figure 3.7b). In type *A*

samples small grains are available in the junction. Therefore the gaps are located in the junctions (Figure 3.7a). In order to get a better defined gap location we should use long junctions like type *A*. In type *b* there can be a shortcoming of the gaps formed in the contacts. Because of the long slits formed, the chance to get multi-junctions in parallel is high. In both types of samples we have well controlled nano-gap formation via EM.

3.1.4 Conclusions

Using the junction resistances $R_J(U)$ and R_J^0 together with our calibration for the dependence of the junction resistivity on temperature, we estimated the local temperature during EM. In regime I before the onset of EM the junction T increases by 80 - 180°C. In regime II our ‘thermometer’ ceases to work, because the junction enters a ‘quasi-ballistic’ regime and where the resistance depends only slightly on temperature. By comparing the power dissipated in the junction with the increase of R_J^0 , it seems that T is still increased above room T . But in the very small constriction where the gap is formed, T is close to room temperature. Because electrons pass through the junction quasi-ballistically, there is much less scattering in the small constriction.

3.2 Transition from classical to ballistic regime in nano-junctions

We mentioned in the Section 3.1.2, that a crossover in the transport regime from diffusive to quasi-ballistic has taken place, as suggested by the SEM image shown in Figure 2.9. In this section we present more evidence for this statement. The possible mechanism for the fast transition from regime I to regime II is discussed as well.

3.2.1 Evidence from the transport mechanism

The picture of a crossover from diffusive to quasi ballistic becomes more plausible, if we closely look at the data of Figure 3.2 in regime II. The junction resistance $R_J(U)$, measured at voltage U even slightly decreases compared to its equilibrium value R_J^0 as EM evolves, as if the temperature would decrease. This effect is very weak in the upper data set, but much more pronounced in the lower. It has been observed in 80% of electromigrated devices. This lowering can easily be understood if we assume that the current-voltage ($I - U$) characteristics becomes non-linear. This is the case when only a few (elastic) scattering centers remain along the length of the junction. In the extreme case of a single scattering center (a

tunnel barrier), $I(U)$ is not linear and increases stronger than linear above a characteristic energy scale, determined by the strength of the scattering center. This is the picture of a scattering unit connected to the electrodes through ballistic wires as we discussed in Section 1.1.2. Here the scattering unit is energy dependent. This proves again that, in regime II, the effective junction length becomes shorter than the elastic scattering length, turning diffusive electron motion into a quasi-ballistic one. Finally, this picture allows us to explain why the fast transition from regime I to regime II flattens off (see Figure 3.1). EM is usually considered in the diffusive regime only, i.e., if there is little scattering, there is little EM. It is therefore reasonable to expect that the step from regime I to II is limited by the transition to the quasi-ballistic regime, in good agreement with the behavior of R_J and R_J^0 discussed above. It may be considered surprising that EM proceeds at all in the quasi-ballistic regime. It implies there is still enough scattering at the constriction to induce narrowing. However, since scattering is limited, the narrowing process in regime II is rather slow. One needs to increase the bias by almost a factor of 3 to finally create a gap. During this process, the total dissipation is not constant, as conjectured by two groups [49; 55], but decreases (Figure 3.1).

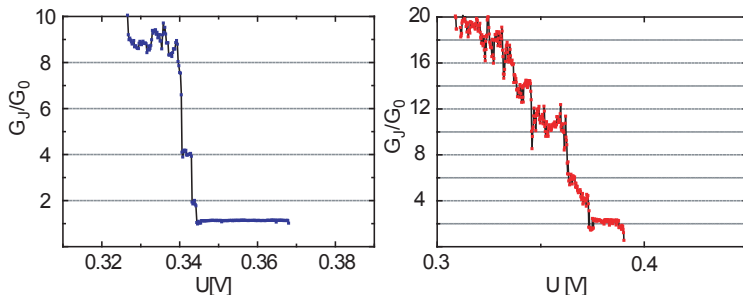


Figure 3.8: Quantized steps of the junction conductance in regime II as EM processes to shrink the junction size.

Quasi-ballistical electron transport in regime II is confirmed also by the observation of quantized steps of conductance during EM. The conduction becomes ballistic only when the constriction gets smaller than the elastic scattering length. We indeed observed at low junction conductance (below $20 G_0$) in regime II, that the junction conductance G_J decreases stepwise as EM processes. The measured G_J shows plateau at integer values of the conductance quantum $G_0 = 2e^2/h$ as shown in Figure 3.8. In one sample the

plateau at G_0 is very stable for more than 5 minutes at room temperature. From the statistics of our experiment, it's not obvious that a favorite value of nG_0 (n is integer) exists, where G_J stays more. We explain this with the different atomic arrangements in the contact region. G_J can have any nG_0 value as observed in many other experiments([95; 96; 97; 98]).

3.2.2 The fast transition from regime I to regime II

The sudden increase of R_J and R_J^0 , which indicates the transition from regime I to regime II, is observed in all samples. To understand this fast increase in junction resistance, we refer to the critical current density j_c and critical temperature T_c , which are defined in Section 3.1.3. We write J_{m1} as the atom flux due to EM under j_c and T_c . In our system j_c is reached by increasing the voltage drop over the junction U . T_c is attained by joule heating in the junction. In Section 1.2 we discussed the relation between EM induced atom flux J_m and current density j as well as temperature T (see Equation (1.16)). We let J_m and those parameters, which depend only on material and conductor geometry, to be constant. A relation between j_c and T_c , at which EM presents and results in a constant atom flux J_m , can be obtained. It can be expressed as $j_c \propto kT_c \cdot e^{E_a/kT_c}$, where E_a is the activation energy of gold diffusion on the surface, k the Boltzmann's constant. We draw this relation for atom flux J_{m1} and J_{m2} as two red curves in Figure 3.9a, where $J_{m1} < J_{m2}$. R_J starts to change when J_{m1} is obtained and changes faster when J_{m2} is obtained. Each pair of j_c and T_c value in curve J_{m1} can trigger EM in the system and induce atom flux J_{m1} . j_c and T_c relation demonstrates that at higher junction temperature lower j_c is required to induce same atom flux. This is indeed observed in EM experiments, where lower j_c is measured at enhanced environment temperature [99; 100]. However our junction is heated up only by Joule heating with $\Delta T \propto j^2$. We draw it as the green curve $j(T)$, T is the temperature in the junction at current density j due to Joule heating. $T = T_0 + \Delta T$ with $\Delta T \propto j^2$ and T_0 the junction temperature before applying the current. In such a system EM occurs at the cross point of red curve J_{m1} and green curve $j(T)$, which is indicated as j_c and T_c . Further increase of Δj over j_c increases the temperature in the junction to T_2 . At $j + \Delta j$ and T_2 a larger atom flux J_{m2} is obtained. EM is therefore sped up and leads to a faster increase of the junction resistance. Let us take a close look at the measured R_J , R_J^0 and T before the fast transition, which is shown in Figure 3.9b. We do observe that T increases slightly after EM occurs at T_c . The increase of R_J and R_J^0 is sped up after EM starts at U_c . Therefore we can adjust the speed of our 'fast transition' by adjusting j . If we want a slow transition at the end of the regime I, we should keep j constant as soon

as EM starts in the junction. Otherwise the fast increase in the junction resistance can be stopped only when the system is changed, so that the relations of J_m to j_c and T_c does not hold. This is what happened in our junctions. The jump is flattened off by the transition to the quasi-ballistic regime, where smaller atom flux is induced by EM under the same value of j and T as before the jump. The smaller atom flux is due to less scattering hence smaller electron wind force in the quasi-ballistic junctions. Note in Figure 3.9b the measured T decreases when R_J^0 fast increases. We suggest, the larger atom flux due to EM changes the junction cross section between R_J and R_J^0 are measured. The second condition to relate $R_J - R_J^0$ with the temperature (see Section 3.1) does not hold. Because the fast transition happens in a very short time, the current density j does not increase much further after EM occurs. Therefore the maximum temperature, which we estimated for regime I, can be considered as correct with the error around ± 20 K.

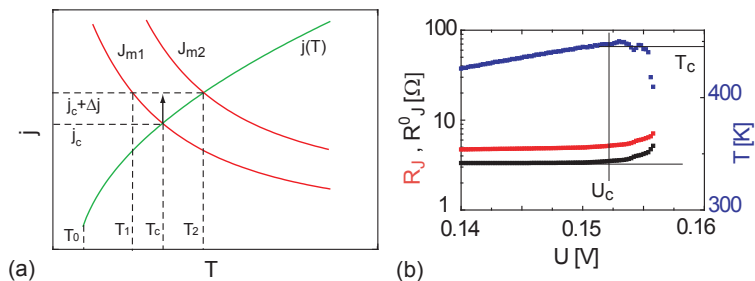


Figure 3.9: (a) Illustration of fast transition with j_c and T_c in the junction. Two red curves are j_c as function of T_c ($j_c \propto kT_c \cdot e^{E_a/kT_c}$, see Equation (1.16)) to obtain constant atom flux J_{m1} or J_{m2} ($J_{m1} < J_{m2}$) in the junction. The green curve $j(T)$ is j as function of T due to Joule heating. T is the temperature in the junction when j is applied. $T = T_0 + \Delta T$ with $\Delta T \propto j^2$. T_0 is the temperature at $j = 0$. The black arrow indicates the increase of j from j_c to $j_c + \Delta j$. (b) The measured R_J , R_J^0 and T in regime I before the fast transition to regime II.

3.2.3 I-V characteristics of formed gap

In order to characterize the formed gap, we do $I-V$ measurements after EM stops in regime III. By ramping up the bias voltage V to a maximum value of 0.5 V over the formed gap, we indeed measure non-linear $I(U)$ characteristics following the expected Simmons theoretical model (see Section 1.1.3) quite

well. This suggests that the junction is in the tunneling regime. Because we applied 0.5 V over the two electrodes, we take the function of tunneling current density at intermediate voltage range ($V < \Phi/e$) for rectangular barrier with Φ the barrier height. For convenience of numerical calculations, Equation (1.10) is often expressed in practical units by inserting the values for all physics constants. When units are taken for J in [A/cm^2], Φ in [V] and s in [\AA], the current density J is given by,

$$J = (6.2 \times 10^{10} / s^2) \{ (\Phi - V/2) e^{-1.025s\sqrt{\Phi - V/2}} - (\Phi + V/2) e^{-1.025s\sqrt{\Phi + V/2}} \} \quad (3.1)$$

One measured $I(U)$ characteristics is presented in Figure 3.10 (black dots). In principle Φ is determined by the work function of the metal electrodes. The work function of Au in vacuum is ≈ 5 eV [89]. However, the energy barrier can be significantly altered if there are gases, water or other adsorbates present. For example, the effective interelectrode barrier can be as high as twice the vacuum work function when He is present on the electrode surfaces [101]. A practical value for the effective barrier height between two gold electrodes is $\Phi \approx 1$ eV [102; 103] for our measurements in air. Because the junction surface is a parameter we can not measure, we write Equation (1.10) in the term of tunneling current by multiplying the current density with the junction surface A . Now we have three parameters to fit our measured $I - V$ data. We take $\Phi = 1$ eV and calculate the current density with Equation (3.1), we found the gap size $s = 2$ nm (red curve) fits our data best. This allows us to estimate that the approximate gap size is around 2 nm.

3.2.4 Conclusions

Once the atomic mobility is sufficient at the end of regime I, EM starts and the wire shrinks locally. The continuous increase in j speeds up EM and result in the fast increase of the junction resistance. This quickly leads to a transition from a strongly diffusive regime, with $L_m \ll L$ to a quasi-ballistic regime with $L_m \simeq L$. This transition explains the flattening of the fast increase in the junction resistance from regime I to II. The ‘strange’ behavior of $R_J < R_J^0$ in regime II agrees well with the electron transport in quasi-ballistic regime. The quantized decrease of conductance at the end of regime II proves that the junction is in the ballistic regime. To our knowledge, little work has been done on EM-induced narrowing of quasi-ballistic constrictions [104; 65]. Understanding this paradoxical situation will be advantageous for our full understanding of EM. This may prove beneficial for semiconductor industry, which uses thinner and thinner interconnects between devices.

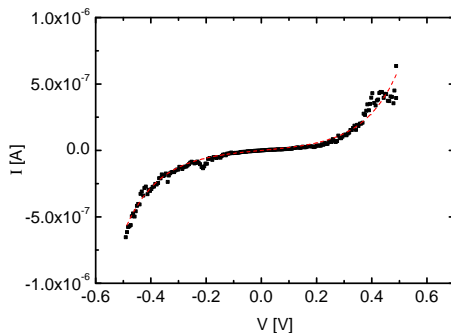


Figure 3.10: Measured I-V characteristics of an EM formed gap (black dots) at room temperature. V is ramped up and down between ± 0.5 V. The dashed red curve is the calculation of Simmons's tunneling equation (see Equation (3.1)).

3.3 Scaling of $1/f$ noise in tunable break-junctions

The study of fluctuations (noise) in physical properties of condensed matter has been an active area of research for decades and has led to profound insights into time-dependent physical phenomena [79; 68; 105; 106; 107]. In the case of charge transport, the noise shows up as a fluctuating time-dependent AC -voltage δV over the device with resistance R (see Section 1.3). The most generic noise contributions stem from equilibrium thermal fluctuations of the electron-bath (Johnson-Nyquist noise) [62; 63], non-equilibrium shot noise caused by the quantization of the electric charge [108], and resistance fluctuations [71; 70; 109; 67; 66; 110; 111; 112; 69; 113]. Whereas thermal and shot noise are frequency independent, resistance fluctuations display a strong dependence which often closely follows a $1/f$ relation over a large frequency range, even down to very low frequencies in the Hz-regime. This $1/f$ -noise has intensively been studied for bulk and thin film conductors [71; 70; 109; 67; 66; 110; 111; 112; 69; 113], in particular as a diagnostic tool for the technologically relevant electromigration mechanism [114; 113; 115; 116].

More recently, noise has also been studied in small constrictions [117; 118; 119; 65], nano-electronic devices [120; 121], quantum point-contacts [122], sub-micron interconnects [123; 124], quantum coherent, quasi-ballistic and ballistic nano-wires [125; 126; 127; 128; 129; 130; 131; 132], as well as

tunneling contacts [133; 134].

The power-spectral density of resistance fluctuations S_R can phenomenologically be described by Hooge's law (see Section 1.3.4):

$$S_R(f)/R^2 = \frac{\alpha}{Nf} \quad (3.2)$$

expressing proportionality of S_R with a $1/f$ frequency dependence. The proportionality factor α/N is ascribed to a material parameter α containing the strength of elastic and inelastic scattering, on the one hand, and to an extensive variable N , on the other hand. The constant N denotes the number of statistically independent fluctuators in the volume and thus scales with the system size. It is straightforward to derive this N dependence by assuming a resistance network with N resistors in series (or in parallel), all fluctuating independently. The total square fluctuation is then inversely proportional to N . In bulk conductors, the total number of electrons has been used for the variable N [67; 111; 135]. Partial support for this view comes from semiconductors in which the carrier density can be changed over many orders of magnitude [135; 136; 137]. Hooge's law therefore states that $1/f$ -noise is a bulk phenomenon, originating homogeneously over the whole volume. In structures of reduced dimensionality, such as thin films and nano-wires, where surface effects may dominate over bulk effect, the leading contribution to $1/f$ -noise may stem from surface roughness and its fluctuations [71; 138; 139; 140]. Which suggests that S_R does not scale with the volume. However, there are no quantitative studies on the scaling behavior of $1/f$ -noise in nano-contacts with tunable cross sections in which this dependence could be explored.

We investigate $1/f$ -noise in tunable metallic nano-constrictions obtained through electromigration [43] and mechanically controlled break-junctions (MCBJs) [90; 91; 3]. In the first type, EM occurring at large current densities is used to change the constriction of the junction. At smaller currents the junctions remain stable allowing for noise measurements. In the second type, the junction geometry is mechanically controlled allowing a gradual narrowing of the constriction down to the single-atom regime. The details to prepare electromigrated junctions and MCBJ is described in Section 2.16. Our emphasis is on the role of the scaling parameter N in nano-contacts in the regime of few transport channels where the transition from diffusive to ballistic transport takes place.

3.3.1 Characteristics of the measured noise spectra

The noise spectrum is measured with the setup then calibrated as described in Section 2.16. Figure 3.11 shows the f -dependence of $S_V(f)$ for a single

MCBJ junction in the ‘low’-ohmic regime with $R_J = 10..65\Omega$ together with a curve for $R_J = 1\text{ k}\Omega$ (shifted down one magnitude). The lowest curve corresponds to 10Ω . To measure $1/f$ -noise we drive the device out of equilibrium by applying a DC voltage $U_J > kT/e$. In the opposite limit $U_J \ll kT/e$, thermal noise would dominate. However, the voltage should not be too large so that EM does not change the junction geometry during the noise measurement. In Figure 3.11 $U_J = 50\text{ mV}$ has been applied, but we can use voltages up to $\sim 0.2\text{ V}$. Except for the lowest curve, the spectra show that $S_V(f)$ decays in a power-law fashion, but this decay is not exactly inversely proportional to f . This fact has often been noted before: $S_V \propto 1/f^\gamma$ with γ ranging between 1 and 2. The latter is expected for a single two-level fluctuator [65] (see Section 1.3.3). In our case, the exponent γ is close to 1 with an average of $\gamma \approx 1.1$, taking all data with $R_J > 20\Omega$. What is remarkable, however, are the sample-to-sample fluctuations in the slope of the spectra, which we observe universally in all devices. In addition to the

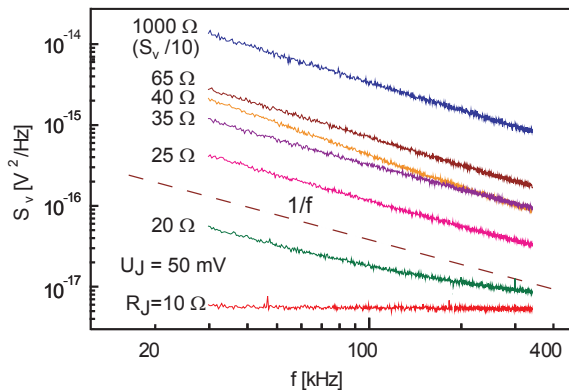


Figure 3.11: Noise spectra of a single MCBJ junction, measured at $U_J = 50\text{ mV}$ and for relatively low junction resistances R_J ranging from 10 to 65Ω (from bottom to top). We also show $S_V(f)$ for $R_J = 1\text{ k}\Omega$ shifted one magnitude down.

sample-to-sample fluctuation of the slope around a mean value of $\gamma \approx 1.1$, we also see that the bottom curve for the smallest junction resistance of $R_J = 10\Omega$ is flat and displays no $1/f$ -noise. This is also true for all devices: $1/f$ -noise only shows up for a sufficiently large junction resistance R_J and finite DC -bias U_J . This is because the thermal noise of the series connection $R_J + 2R_L$, which dominates at a small bias U_J and small R_J . After increasing

R_J at constant U_J , the f -dependence of S_V sets in. The $1/f$ dependence shows up first on the low frequency side. At higher frequency the thermal noise still dominates. This leads to the impression that the spectrum is flatter than $1/f$ in this transition regime from ‘low ’to ‘large ’ R_J values. To demonstrate this more clearly we show a simulated spectrum of $R_J = 20 \Omega$ in Figure 3.11 with the superposition of $1/f$ noise and the white thermal noise of $R_J + 2R_L$ (black dashed lines) in Figure 3.12. The superposition (red curve) matches very well with the measured spectrum (blue line).

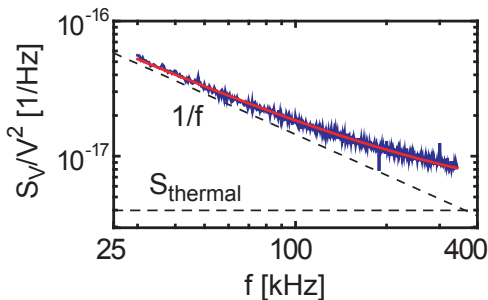


Figure 3.12: The red curve is the superposition of a $1/f$ and the thermal noise of $R_J + 2R_L$ (black dashed lines). The blue data point is the measured spectrum of $R_J = 20 \Omega$ at $U_J = 50$ mV. The simulation matches well with the data points.

Experimentally we deduce power γ in $S_V \propto 1/f^\gamma$ directly from the measured spectra by linear fitting the spectra in the log-log plot. The extracted γ as a function of R_J is shown in Figure 3.13. The open symbols belong to junctions with too low R_J . Only the filled symbols correspond to junctions displaying full $1/f$ -noise. There is quite some scatter in γ , but all values stay close to $\gamma = 1$. In order to shed light on the origin of the $1/f$ -noise, the voltage dependence of S_V has been analyzed. The MCBJ and voltage source is adjusted to achieve various R_J and U_J for a systematic measurement of $S_V \sim U_J$ relation. In Figure 3.14a we show the pattern of U_J and R_J , where S_V is measured. Figure 3.14b shows S_V taken at a fixed frequency of 100 kHz as a function of U_J . The different symbols refer to three junction values with $R_J = 50, 300$ and 500Ω . We find a strong increase of S_V with U_J which is in quite good agreement with a quadratic dependence, i.e. $S_V \propto U_J^2$, for not too large voltages ($\lesssim 0.2$ V). We apply $U_J < 0.2$ V in our measurement, because for $U_J \approx 0.2$ V in the junction of $R_J \approx 50 \Omega$, EM starts and results in a slightly increase of the resistance of the junction. At $U_J \approx 0.15$ V there

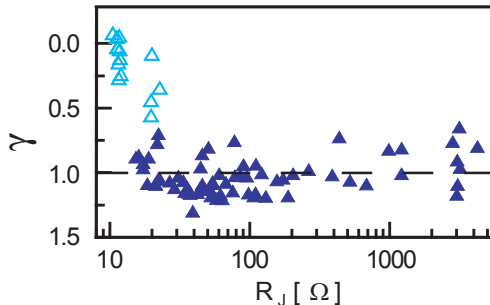


Figure 3.13: The exponent γ of the frequency dependence deduced from the noise spectrum of many junctions with a large range of junction resistances R_J and bias voltages U_J . The open symbols correspond to devices with small R_J and measurements at small bias voltage U_J , displaying only white noise originating from the lead resistances. The average value of γ for the filled symbols is equal to 1.1 and therefore close to the expected value for $1/f$ noise.

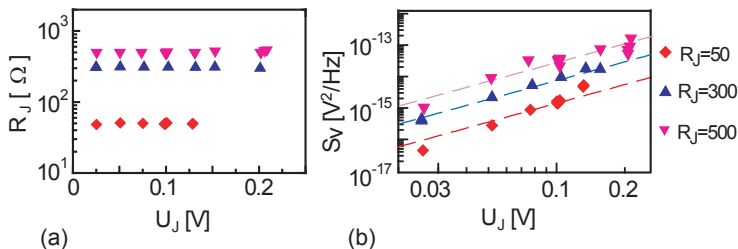


Figure 3.14: (a) The MCBJ and voltage source is adjusted to achieve R_J and U_J at wanted value. At those value S_V is measured. (b) The bias voltage dependence of S_V at a fixed frequency of $f_0 = 100$ kHz and for three different R_J values. The dashed lines are reference lines with $S_V \propto U_J^2$.

is no visible change in junction resistance, but the measured noise deviates from the quadratic dependence $S_V \propto U_J^2$. It can be a weak atom flux due to EM in the junction. The flux is not large enough to produce fast increase in R_J , but can influence the measured $1/f$ -noise [115; 141]. At larger R_J EM sets in at higher U_J as we found in our EM experiments (Section 3.2). Furthermore we want to avoid Joule heating induced temperature increases in the junction, which would also effect the measured spectrum, even though

$1/f$ -noise in Au film depends slightly on temperature [78]. Therefore for $R_J < 100 \Omega$, we measure S_V at $U_J \leq 0.1$ V and for $R_J > 100 \Omega$, we measure S_V at $U_J < 0.2$ V. The quadratic dependence of $S_V \propto U_J^2$ agrees with our expectation for resistance fluctuations as the source of $1/f$ -noise (see Section 1.3.4).

3.3.2 Transition from diffusive to ballistic transport regime

Having established the $1/f$ dependence and confirmed resistance fluctuations as its origin, we consider next the pre-factor α/N introduced in Equation (3.2). Because α is considered as constant, hence α/N is the scaling factor, which we are looking for. Hundreds spectra of S_V on more than 15 samples have been measured as function of the junction cross-section, i.e. as a function of R_J , and the $1/f$ contribution was extracted within the frequency interval 30 - 400 kHz following the procedure described in Section 2.16. To compare the magnitude of S_V for different samples and different junctions, we now take the normalized noise $S_V(f)/V^2$ at a fixed frequency of $f = f_0 = 100$ kHz. In Figure 3.15 we show a scatter plot of

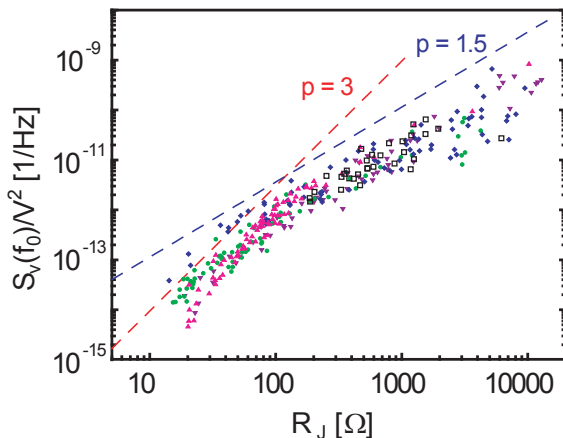


Figure 3.15: Magnitude of the $1/f$ -noise, shown as a log-log scatter plot of $S_V(f_0)/V^2$ with $f_0 = 100$ kHz for four MCBJ samples and one EM sample (open squares) as a function of junction resistance R_J . $1/f$ -noise in EM sample has same magnitude and the same scaling exponents as MCBJs in ballistic regime.

$S_V(f_0)/V^2$ as a function of R_J for several samples in a double-logarithmic

representation. Four sets were obtained with MCBJ samples and one with an EM sample (open squares). We note that EM samples typically cover only the regime $R_J > 100 \Omega$, because when EM sets in, there is a relatively fast transition from the low-ohmic regime (I) to the intermediate resistance regime (II) (see Section 2.2.3). The noise measurement is carried out after the transition in the range of $100 \Omega < R_J < 10k\Omega$. R_J is then increased in several steps by short EM processes in the junction. The noise is measured at $U_J < 0.2$ V when EM is stopped. The scatter plot clearly displays a cross-over from a power law dependence $S_V(f0)/V^2 \propto R_J^p$ with a large power at low R_J and a smaller one at large R_J . The dashed lines are exponent $p=3$ in red and $p=1.5$ in blue to guide the eyes. This cross-over is better seen in Figure 3.17. Although there is some sample to sample variation, we always observe a cross-over in all of our samples in the vicinity of $R_J \approx 100 \Omega$. The deduced powers are consistent with $p = 1.5$ and $p = 3$ for large and low R_J , respectively. The transition and the deduced values are in agreement with $1/f$ -noise generated in the bulk together with a transition from the diffusive to the ballistic transport regime with increasing R_J as we will outline in the following. It has been pointed out by Hooge [135], that $1/f$ -noise is a bulk phenomenon, whose scaling parameter N should grow like the volume Θ . Although this has been disputed and was discussed many times over the last two decades, we will assume scaling with volume and compare to scaling with the surface afterwards. Let us denote a characteristic length of the junction by l . In order to refer to size-scaling, we use the terminology length $\sim l$, which reads ‘length scales with l ’. Obviously, $\Theta \sim l^3$. In a diffusive wire of length L and cross-section A , the resistance R is given by $R = \rho L/A$, where ρ is the specific resistance. Hence, $R \sim l^{-1}$. Because $S_V/V^2 \propto 1/N \sim l^{-3}$ (Equation (3.2)), we expect $S_V/V^2 \propto R^3$ in this transport regime. If the characteristic length of the junction becomes shorter than the momentum scattering mean-free path L_m (see Section 1.1.1), the sample is in the ballistic regime. In this regime, the conductance is determined by the number of transport channels, which is proportional to the junction area. The corresponding junction resistance is the so called Sharvin’s resistance [7] (see Section 1.1.2). Hence, $R \propto A^{-1} \sim l^{-2}$. Consequently, $S_V/V^2 \propto R^{1.5}$. The data in Figure 3.15 shows a crossover which agrees with these derived exponents. Note that the cross-over takes place at $R_J \approx 100 \Omega$. This is also in good agreement with our observation in EM measurement, where a transition from diffusive (regime I) to ballistic (regime II) presents. At $R_J > 100 \Omega$ the junction shows quasi-ballistic transport behavior (see Section 3.2).

3.3.3 Hooge's constant α

We introduced in Section 1.3.4, that Hooge's constant α in Equation (3.2) can vary between 10^{-6} to 10^{-3} in different materials. Even for a given metal smaller α is measured in metal films with lower defect and impurity scattering [142]. It is therefore interesting to check Hooge's constant α in our Au junctions.

From the $S_V(f_0)/V^2$ versus R_J plot we can estimate Hooge's constant α . This parameter corresponds to the noise value for $N = 1$ at $f = 1$ Hz

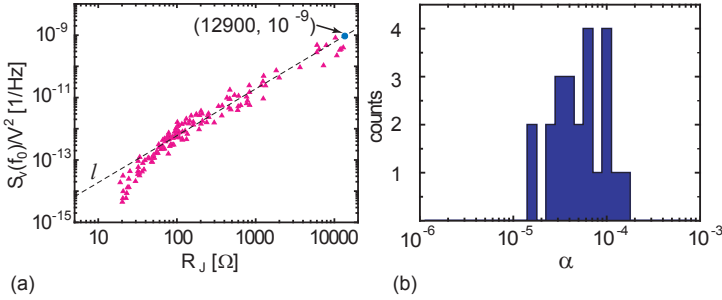


Figure 3.16: (a) Extrapolation data set to get α . The black dashed line is function l which fits best the $S_V(f_0)/V^2$ dependence on $R_J^{1.5}$. The blue point is on l at $R_J = 12900 \Omega$. (b) Histogram of α -values deduced from S_V for the single-atom contact when $R_J = h/2e^2$.

(Equation (3.2)). If we associate N with the number of electrons (which for Au is the same as the number of atoms), we have to look at the S_V/V^2 value for the single atom contact. Because the single atom formed junction is not stable, therefore we are not able to measure the noise for all devices at single atom contact. From the previous discussion, we expect $S_V/V^2 \propto R^{1.5}$ in ballistic regime. We fit the measured $S_V(f_0)/V^2$ data in log-log plot with the linear slope close to 1.5, i.e. $S_V(f_0)/V^2 = b \cdot R^p$ with $p \approx 1.5$. Then we extrapolate the value for $S_V(f_0)/V^2$ at $R_J = h/2e^2 \approx 12.9k\Omega$ from the linear fit. In Figure 3.16a we show an example of noise measured on one of the devices. A linear function $l = 6 \times 10^{-16} \times R_J^{1.5}$ (black dashed lines), which fits the data best, is chosen to describe the $S_V(f_0)/V^2 \sim R_J^{1.5}$ dependence in the ballistic regime. To get α , we normalize the value of function l at $R_J = 12900 \Omega$ for $f_0 = 100kHz$. For this device we find $S_V(f_0)/V^2 \approx 10^{-9}$ and $\alpha = 6 \times 10^{-4}$. In all measured data sets we find typically $S_V(f_0)/V^2 \approx 10^{-10} - 10^{-9} Hz^{-1}$ thus $\alpha \approx 10^{-5} - 10^{-4}$. Some deviation in p from 1.4 to 1.7 is observed during the linear fit for all samples.

But we can find the mean value of $p \approx 1.5$. α values deduced in this way are shown as a histogram in Figure 3.16b. This range of α -values compares very well with parameters reported in the literature [65; 142]. It is lower than reported α measured in bulk which is $\approx 5.6 \times 10^{-3}$. This implies that we have less defects and impurities in our Au junctions. However we have to note that, we measure α in the junctions in ballistic regime, whereas others in bulk material in diffusive regime.

3.3.4 Bulk origin of $1/f$ -noise in nano-contacts

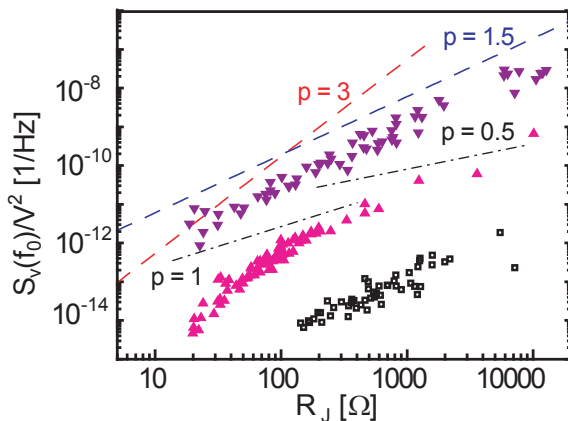


Figure 3.17: Data from two MCBJs and one EM sample (open squares) where the upper (triangles) and lower (black squares) sets are vertically shifted by two-orders of magnitude for clarity. Dashed lines are guides to the eyes for the expected power-law dependencies $S_V(f_0)/V^2 \propto R_J^p$ in the diffusive ($p = 3$) and ballistic ($p = 1.5$) regime. The dashed-dotted line has slopes $p = 1$ in the diffusive and $p = 0.5$ in the ballistic regime when surface effect is assumed.

Whether $1/f$ -noise origins from bulk or surface is a matter of debate since two decades. Both statements are supported by various experimental studies. In structures with reduced dimensionality, such as thin film and nano-wires, there is more evidence of surface effect contribution to $1/f$ -noise. We argue here that the $1/f$ -noise we measured in our nano-contacts is a bulk effect. The evidence is provided by good agreement of the measured data with our model, where we assumed the $1/f$ -noise to originate from bulk properties and its behavior scales with the volume of the constriction

. For comparison, we derive here the expected power law, for the case that transport is ballistic and the fluctuators leading to $1/f$ -noise are only present at the surface. All transport channels in the interior of the junction are assumed to be noiseless: In this case S_V/V^2 will be inversely proportional to N_S , where N_S stands for the number of transport channels at the surface. This number scales as the circumference of the nano-contacts, and therefore $N_S \sim l$. Using Ohm's law for a diffusive wire $R \propto L/A^{-1} \sim l^{-1}$ we obtain $S_V/V^2 \propto R$. Using the Sharvin's resistance for a ballistic contact $R \propto A^{-1} \sim l^{-2}$ we arrive at $S_V/V^2 \propto R^{0.5}$. $p = 1$ and $p = 0.5$ is much different than $p = 3$ and $p = 1.5$. We are able to distinguish between the two pairs of values very well. In Figure 3.17 we present data from two MCBJs and one EM sample (open squares). The upper and lower data sets are vertically shifted by two-orders of magnitude for clarity. The expected power-law dependencies $S_V/V^2 \propto R^p$ is draw for bulk effect at $p = 3$ (diffusive) and $p = 2$ (ballistic) as dashed lines. The dash-dotted line corresponds to $p = 1$ (diffusive) and $p = 0.5$ (ballistic), if our measured $1/f$ noise is a surface effect. It is clear that the slope of the measured data points is much larger. It proves that even in small junctions, in which only a few channels carry the charge current, all of them contribute to $1/f$ -noise and not only the channels close to the surface. Furthermore, the $1/f$ -noise measured in EM junction has the same magnitude and the same scaling exponents (see Figure 3.17) as in MCBJs. This confirms the discussed effects are universal in the sense, that they do not depend on the measurement technique and sample preparation.

3.3.5 Conclusion

In conclusion, we have studied the $1/f$ voltage noise of gold nano-contacts in electromigrated and mechanically controlled break-junctions having resistance values R that can be tuned from 10Ω (many channels) to $10 \text{ k}\Omega$ (single atom contact). The noise is caused by resistance fluctuations as evidenced by the $S_V \propto V^2$ dependence of the power spectral density S_V on the applied DC voltage V . As a function of R , the normalized noise S_V/V^2 shows a pronounced cross-over from $\propto R^3$ for low-ohmic junctions to $\propto R^{1.5}$ for high-ohmic ones. The measured powers of 3 and 1.5 are in agreement with $1/f$ -noise generated in the bulk and reflect the transition from diffusive to ballistic transport. This transition appears at $R_J \approx 100\Omega$. We show that even in very small junctions and in the ballistic transport regime, $1/f$ -noise is a bulk property. $1/f$ -noise measured in MCBJs and EM junctions exhibit the same behavior in ballistic regime.

Chapter 4

Conclusions and outlook

In this thesis we presented a successful technique to implement smooth EM in gold nano-junctions. By using a fast feedback voltage source (response time $< 0.5 \mu\text{s}$) over a four-terminal nano-junction, the voltage drop over the junction can be exactly measured and controlled. Hence the current density in the junction, which is the key parameter of EM, is under control as well. This technique solves the previous problem of thermal runaway in the junction. It highly increases the speed and the success rate of nano-gaps formation. During EM we are able to evaluate the temperature in the junction. In our junctions the temperature required to trigger EM is over 100°C . If we think about molecular electronics, the usual way is to assemble the molecules on the junction surface before EM. From our estimation of temperature the molecules may get destroyed during EM. A transition from diffusive to ballistic regimes is observed while the junction cross-section is shrunk by EM. In quasi-ballistic regime we can not estimate the temperature by junction resistance measurement, because the resistance depends only slightly on temperature in quasi-ballistic regime. We expect that the temperature is still enhanced in the junction. But at the very small constriction where the gap is formed, there is no enhancement of temperature. Hence we suggest to assemble the molecules after the first transition into regime II, then open the gap by starting EM again. Very surprisingly, EM proceeds in the quasi-ballistic regime as well. However EM is much slowed down there. The decrease of conductance in quantized steps of G_0 is observed at the end of the regime II.

Due to smooth EM in nano-junctions, we are able to investigate resistance fluctuation ($1/f$ noise) in the junction as function of junction resistance. The

$1/f$ noise is measured and compared in both electromigrated junctions and MCBJ. The scaling of $1/f$ with junction resistance is very similar in both electromigrated junction and MCBJ. The cross-over from diffusive to ballistic regime is visible in measured noise magnitude. The noise magnitude scales with junction resistance in power 3 in diffusive regime and power 1.5 in ballistic regime. We are able to conclude the $1/f$ noise in the junctions is generated in Bulk, which is true even for the very small junctions where only few conduct channels available. Hooge's parameter α extracted from the noise data compares very well with parameters reported in the literature [65].

Based on our knowledge about EM in gold junctions, we expect some new experiments we can try in the future. On one hand we can extend the application of our existing setup. For example to thin the junction to only few nanometers in cross-section, then break it by MCBJ with very little bending. So that we can break the junctions fabricated on glass substrates [143]. The advantage of the glass substrate is to do in situ optical spectroscopy experiments. We can also combine EM with other techniques, such as the trapping of nano-particles [144] or field emission [145], to open and close the junctions many times like MCBJ. This will increase the efficiency of electromigrated junctions and induce a new system with the advantages of both EM junction and MCBJ. On the other hand we can explore EM in other materials. The first choice can be magnetic metals, such as Co, Ni, Fe, magnetic permalloy and even more complicated structure with multi-layers of various ferromagnetic metals. Those material are often used for magnetoresistances in magnetic nano-contacts studies. The stable electromigrated nano-contacts can be very useful in those experiments. Some novel materials such as carbon nano-tubes (CNT) [146] and single layer graphene sheet [147] can be the next candidates. We can investigate and characterize the EM process in CNT and graphenene junctions. Finally we can upscale the fabrication of nano-gaps to a large quantity with our fast EM technique, for example few hundred nano-gaps on one substrate. The fast speed and high yields ensures our EM technique an efficient method to prepare the nanometer sized electrodes for molecules measurement.

In the area of noise measurement, it is worth to redo Voss and Clarke's experiment [148] in turnable junction systems. In their experiments they could verify the spectrum of low-frequency fluctuations of the thermal noise in metal films is $1/f$ and its magnitude is same as what measured with common method under nonzero current in similar systems. This statement can be examined, if a cross-over from diffusive to ballistic regime would be observed.

List of Figures

1.1	Diffusive and ballistic conductor	2
1.2	Schematics of Sharvin resistance	4
1.3	Ballistic quantum wire connected to two wide electrodes	6
1.4	Model of arbitrary conductor with scattering unit	7
1.5	Tunneling through rectangular potential barrier	8
1.6	Illustration of wind force and direct force	12
1.7	Bamboo like crystalline structure	15
1.8	Schematic of two-terminal EM	16
1.9	Two level fluctuations and the spectrum	21
1.10	$1/f$ spectrum	21
1.11	$1/f$ -noise spectrum by superposition	23
2.1	Sample structure	26
2.2	UV and E-beam lithography	27
2.3	Angle evaporation	29
2.4	One step E-beam structure	30
2.5	Principle of feed-back controlled EM	32
2.6	Layout of EM setup	33
2.7	Ramp up of the voltage U in a square-wave pattern	35
2.8	The junction resistance $R_J(U)$ versus U during EM	36
2.9	Illustration of the slit formation and SEM images.	37
2.10	Multiple runs of EM in the same junction.	37
2.11	EM in Co junction	39
2.12	Multiple runs of EM in Co junction and SEM image	39
2.13	Schematics of low T resistivity measurement	41
2.14	Temperature dependence of resistivity	42

2.15	SEM image of noise samples	43
2.16	Setup for noise measurement	44
2.17	The equivalent circuit of noise measurement setup	46
2.18	Frequency dependent gain of amplifier and measuring inductance	47
2.19	Calibration with thermal noise	48
3.1	The junction resistance $R_J(U)$ and R_J^0 versus U	51
3.2	$\Delta R/R_J^0$ and the temperature in the junction	52
3.3	Power dissipation in diffusive and quasi-ballistic wires	53
3.4	SEM images of two types of sample	53
3.5	Definition of j_c and T_c	54
3.6	Histogram of j_c and T_c	54
3.7	Gaps formed in ‘straight wire’ and ‘bow tie’ type junctions	55
3.8	Quantized steps of the junction conductance in regime II	57
3.9	Illustration of fast transition with j_c and T_c and measured $R_J(U)$, $T(U)$	59
3.10	I-V characteristics of formed gap.	61
3.11	Noise spectra of a single MCBJ junction	63
3.12	Spectrum of superposition from a $1/f$ and thermal noise	64
3.13	The exponent γ deduced from the noise spectrum	65
3.14	The bias voltage dependence of S_V	65
3.15	Cross over in magnitude of $1/f$ -noise versus R_J	66
3.16	Histogram of α -value	68
3.17	Compare bulk effect with surface effect	69
A.1	Diagram and photo of four-terminal feedback voltage source	84
A.2	Photo of ground loop killer	85
A.3	Diagram of low noise voltage source	86
B.1	Principle of MCBJ and the setup	87
C.1	Noise measured in electromigrated junction	90

Bibliography

- [1] A. Aviram and M. Ratner, Chem. Phys. Lett. **29**, 277 (1974).
- [2] J. Park et al., Nature **417**, 722 (2002).
- [3] N. Agraït, A. L. Yeyati, and J. M. van Ruitenbeek, Phys. Rep. **377**, 81 (2003).
- [4] S. Datta, *Electronic Transport in Mesoscopic Systems*, Cambridge University Press, 2002.
- [5] S. Washburn, *Quantum Coherence in Mesoscopic Systems*, Plenum Press, New York, 1991, Resistance fluctuations in small samples: be careful when playing with ohm's law pp. 341-367.
- [6] J. Maxwell, *A Treatise on Electricity and Magnetism, Vol. 1*, Dover Publications inc., New York, 1954.
- [7] Y. V. Sharvin, Soviet Phys. JETP **21**, 655 (1965).
- [8] A. Jansen, A. van Gelder, and P. Wyder, J. Phys. C: Solid St. Phys. **13**, 6073 (1980).
- [9] G. Wexler, Proc. Phys. Soc. **89**, 927 (1966).
- [10] R. Landauer, IBM J. Res. Dev **1**, 223 (1957).
- [11] J. C. Cuevas, J. Heurich, F. Pauly, W. Wenzel, and G. Schon, Nature Nanotechnology **14**, R29 (2003).
- [12] R. Landauer, Phil. Mag. **21**, 863 (1970).

- [13] R. Landauer, Phys. Scr. **T42**, 110 (1992).
- [14] J. Fisher and I. Giaever, J. Appl. Phys. **32**, 172 (1961).
- [15] A. Sommerfeld and H. Bethe, *Handbüch der Physik von Geiger und Scheel*, volume 24/2, Julius Springer Verlag, Berlin, 1933.
- [16] R. Holm and B. Kirschstein, Z. Tech. Physik **16**, 488 (1935).
- [17] R. Holm, J. Appl. Phys. **22**, 569 (1951).
- [18] J. G. Simmons, J. Appl. Phys. **34**, 1793 (1963).
- [19] D. Bohm, *Quantum Theory*, Prentice-Hall, Inc., Englewood Cliffs, New Jersey, 1951.
- [20] S. de Groot, *Thermodynamics of irreversible processes*, North Holland publishing company, Amsterdam, The Netherlands, 1963.
- [21] L. Onsager, Physica Review **37**, 405 (1931).
- [22] S. van der Molen, M. Welling, and R. Gressen, Phys. Rev. Lett. **85**, 3882 (2000).
- [23] K.-N. Tu, J. W. Mayer, and L. C. Feldman, *Electronic Thin Film Science for Electrical Engineers and Materials Scientists*, Macmillan, New York, 1992.
- [24] V. Fiks, Sov. Phys. Solid State **1**, 14 (1959).
- [25] H. Huntington and A. Grone, J. Phys. Chem. Solids **20**, 76 (1961).
- [26] I. Blech, J. Appl. Phys. **47**, 1203 (1976).
- [27] N. Wilson, *The structure and dynamics noble metal clusters*, PhD thesis, University of Birmingham, 2000.
- [28] I. Blech and C. Herring, Appl. Phys. Lett. **29**, 131 (1976).
- [29] M. Trouwborst, S. van der Molen, and B. van Wees, J. Appl. Phys. **99**, 114316 (2006).
- [30] J. R. Black, Proc. IEEE **57**, 1587 (1969).
- [31] A. Nitzan and M. A. Ratner, Science **300**, 1384 (2003).
- [32] R. L. McCreery, Chem. Mater. **16**, 4477 (2004).

- [33] M. A. Reed, *Natural Material* **3**, 286 (2004).
- [34] N. J. Tao, *Nature Nanotechnology* **1**, 173 (2006).
- [35] S. M. Lindsay and M. A. Ratner, *Adv. Mat.* **19**, 23 (2007).
- [36] B. A. Mantooth and P. S. Weiss, *Proc. IEEE* **91**, 1785 (2003).
- [37] D. K. James and J. M. Tour, *Chem. Mater.* **16**, 4423 (2004).
- [38] B. Xu and N. Tao, *Science* **301**, 1221 (2003).
- [39] M. A. Reed, C. Zhou, C. J. Muller, T. P. Burgin, and J. M. Tour, *Science* **278**, 250 (1997).
- [40] L. Grüter, M. Gonzaleza, R. Huber, M. Calame, and C. Schönenberger, *Small* **1**, 1067 (2005).
- [41] J. G. Kushmerick et al., *Phys. Rev. Lett.* **89**, 086802 (2002).
- [42] M. Chabynyc et al., *J. AM. CHEM. SOC.* **124**, 11730 (2002).
- [43] H. Park, A. K. L. Lim, A. P. Alivisatos, J. Park, and P. L. McEuen, *Appl. Phys. Lett.* **75**, 301 (1999).
- [44] H. Park et al., *Nature* **407**, 57 (2000).
- [45] A. N. Pasupathy et al., *Nano Lett.* **5**, 203 (2005).
- [46] W. J. Liang, M. P. Shores, M. Bockrath, J. R. Long, and H. Park, *Nature* **417**, 725 (2002).
- [47] H. S. J. van der Zant, E. A. Osorio, M. Poot, and K. O'Neill, *Phys. stat. sol. (b)* **243**, 3408 (2006).
- [48] M. H. Jo et al., *Nano Lett.* **6**, 2014 (2006).
- [49] A. A. Houck, J. Labaziewicz, E. K. Chan, J. A. Folk, and I. L. Chuang, *Nano Lett.* **5**, 1685 (2005).
- [50] R. Sordan, K. Balasubramanian, M. Burghard, and K. Kern, *Appl. Phys. Lett.* **87**, 013106 (2005).
- [51] H. B. Heersche, Z. de Groot and J. A. Folk, L. P. Kouwenhoven, and H. S. J. van der Zant, *Phys. Rev. Lett.* **96**, 017205 (2006).
- [52] H. S. J. van der Zant et al., *Faraday Discuss.* **131**, 347 (2006).

- [53] D. R. Strachan et al., *Nano Lett.* **6**, 441 (2006).
- [54] K. O'Neill, E. A. Osorio, and H. S. J. van der Zant, *Appl. Phys. Lett.* **90**, 133109 (2007).
- [55] D. R. Strachan et al., *Appl. Phys. Lett.* **86**, 43109 (2005).
- [56] G. Esen and M. S. Fuhrer, *Appl. Phys. Lett.* **87**, 263101 (2005).
- [57] T. Taychatanapat, K. I. Bolotin, F. Kuemmeth, and D. C. Ralph, *Nano Lett.* **7**, 652 (2007).
- [58] S. M. Oberholzer, *Fluctuation Phenomena in Low dimensional Conductors*, PhD thesis, University Basel, 2001.
- [59] R. Landauer, *Phys. Rev. B* **47**, 16427 (1993).
- [60] L. D. Landau and E. M. Lifschitz, *Statistical Physics*, volume Part I, Nauka, Moscow, 1976.
- [61] Y. Imry, *Introduction to Mesoscopic Physics*, Oxford University Press, Oxford, 1997.
- [62] M. B. Johnson, *Phys. Rev.* **29**, 367 (1927).
- [63] H. Nyquist, *Phys. Rev.* **32**, 110 (1928).
- [64] M. von Hartmann, M. Sanden, M. Östling, and G. Bosman, *J. Appl. Phys.* **92**, 4414 (2002).
- [65] P. Holweg, J. Caro, A. Verbruggen, and S. Radelaar, *Phys. Rev. B.* **45**, 9311 (1992).
- [66] P. Dutta and P. M. Horn, *Rev. Mod. Phys.* **53**, 497 (1981).
- [67] F. N. Hooge, T. G. M. Kleinpenning, and L. K. J. Vandamme, *Rep. Prog. Phys.* **44**, 479 (1981).
- [68] A. van der Ziel, *Noise*, Prentice-Hall, Englewood Cliffs, 1954.
- [69] M. B. Weissmann, *Rev. Mod. Phys.* **60**, 537 (1988).
- [70] R. F. Voss and J. Clarke, *Phys. Rev. B* **13**, 556 (1976).
- [71] F. N. Hooge, *Phys. Lett. A* **29**, 139 (1969).
- [72] F. N. Hooge, *IEEE Trans. Electr. Dev.* **41**, 1926 (1994).

- [73] F. N. Hooge and L. K. J. Vandamme, *Phys. Lett. A* **66**, 315 (1978).
- [74] A. L. McWhorter, *Semiconductor surface physics*, University of Pennsylvania Press, Philadelphia, 1957.
- [75] A. L. McWhorter, *Physical Review* **98**, 1191 (1955).
- [76] F. N. Hooge, *Physica B: Condensed Matter* **336**, 236 (2003).
- [77] P. Handel, *Phys. Rev. A* **22**, 745 (1980).
- [78] J. Eberhard and P. Horn, *Phys. Rev. B* **18**, 6681 (1978).
- [79] P. Bak, C. Tang, and K. Wiesenfeld, *Phys. Rev. Lett.* **59**, 381 (1987).
- [80] B. Fourcade and A. Tremblay, *Phys. Rev.* **B34**, 7802 (1987).
- [81] S. Feng, P. Lee, and A. stone, *Phys. Rev. B* **56**, 1960 (1986).
- [82] J. Pelz and J. Clarke, *Phys. Rev.* **B36**, 4479 (1987).
- [83] B. Stahlmecke and G. Dumpich, *Defect and Diffusion Forum* **237-240**, 1163 (2005).
- [84] C. Yang, C. Zhang, J. Redepenning, and B. Doudin, *Appl. Phys. Lett.* **84**, 2865 (2004).
- [85] A. Sokolov, C. Zhang, E. Tsymbal, J. Redepenning, and B. Doudin, *Nature Nanotechnology* **2**, 171 (2007).
- [86] N. Ashcroft and I. Mermin, *Solid State Physics*, Harcourt College Publishers, 1976.
- [87] M. F. Lambert, M. F. Goffman, J. Bourgoïn, and P. Hesto, *Nature Nanotechnology* **14**, 772 (2003).
- [88] C. Durkan and M. Welland, *Ultramicroscopy* **82**, 125 (2000).
- [89] I. Grigoriev and E. Meilikhov, editors, *Handbook of physical quantities*, CRC Press, 1997.
- [90] J. M. van Ruitenbeek et al., *Rev. Sci. Instrum.* **67**, 108 (1996).
- [91] E. Scheer, P. Joyez, D. Esteve, C. Urbina, and M. H. Devoret, *Phys. Rev. Lett.* **78**, 3535 (1997).
- [92] Z. Wu et al., *Appl. Phys. Lett.* **91**, 053118 (2007).

- [93] Y. Selzer, M. A. Cabassi, T. S. Mayer, and D. L. Allara, *Nature Nanotechnology* **15**, 483 (2004).
- [94] L. H. Yu and D. Natelson, *Nano Lett.* **4**, 79 (2004).
- [95] J. Krans et al., *Phys. Rev. B* **48**, 14721 (1993).
- [96] C. Muller, J. van Ruitenbeek, and L. de Jongh, *Phys. Rev. Lett.* **69**, 140 (1992).
- [97] N. Agrait, J. Rodrigo, and S. Vieira, *Phys. Rev. B* **47**, 12345 (1993).
- [98] M. Brandbyge et al., *Phys. Rev. B* **52**, 8499 (1995).
- [99] Z. M. Wu, Nanogap formation by electromigration technique, Master's thesis, University Basel, 2005.
- [100] M. Austin and S. Chou, *J. Vac. Sci. Technol. B* **20**, 665 (2002).
- [101] O. Y. Kolesnychenko, O. I. Shklyarevskii, and H. van Kempen, *Phys. Rev. Lett.* **83**, 2242 (1999).
- [102] S. A. G. Vrouwe et al., *Phys. Rev. B* **71**, 035313 (2005).
- [103] C. Lebreton, PhD thesis, Université Paris, 1996.
- [104] K. S. Ralls, D. C. Ralph, and R. A. Buhrman, *Phys. Rev. B* **40**, 11561 (1989).
- [105] S. Kogan, *Electronic noise and fluctuations in solids*, Cambridge Univ. Press, 1996.
- [106] Y. M. Blanter and M. Büttiker, *Phys. Rep.* **336**, 1 (2000).
- [107] C. Beenakker and C. Schönberger, *Phys. Today* **56**, 37 (2003).
- [108] W. Schottky, *Ann. Phys.* **57**, 514 (1918).
- [109] D. A. Bell, *J. Phys. C* **13**, 4425 (1980).
- [110] M. S. Keshner, *Proc. IEEE* **70**, 212 (1982).
- [111] D. M. Fleetwood, J. T. Masden, and N. Giordano, *Phys. Rev. Lett.* **50**, 450 (1983).
- [112] N. Giordano, *Rev. Solid State Science* **3**, 27 (1989).
- [113] L. K. J. Vandamme, *IEEE Trans. Elect. Dev.* **41**, 2176 (1994).

- [114] R. S. Sorbello, *Material Reliability Issues in Microelectronics Symposium*, pages 3–13, Materials Research Society, Pittsburgh, 1991.
- [115] K. Dagge, W. Frank, A. Seeger, and H. Stoll, *Appl. Phys. Lett.* **68**, 1198 (1996).
- [116] J. Dong and B. Parviz, *Nature Nanotechnology* **17**, 5124 (2006).
- [117] I. Yanson, A. Akimenko, and A. Verkin, *Solid State Communications* **43**, 765 (1982).
- [118] A. I. Akimenko, A. B. Verkin, and I. K. Yanson, *J. Low Temp. Phys.* **54**, 1573 (1984).
- [119] K. S. Ralls and R. A. Buhrman, *Phys. Rev. B* **44**, 5800 (1991).
- [120] G. Zimmerli, T. M. Eiles, R. L. Kautz, and J. M. Martinis, *Appl. Phys. Lett.* **61**, 237 (1992).
- [121] H. Birk, M. J. M. de Jong, and C. Schönenberger, *Phys. Rev. Lett.* **75**, 1610 (1995).
- [122] F. Liefrink et al., *Phys. Rev. B* **46**, 15523 (1992).
- [123] B. Neri, C. Ciof, and V. Dattilo, *IEEE Trans. Electr. Dev.* **44**, 1454 (1997).
- [124] A. Bid, A. Bora, and A. K. Raychaudhuri, *Phys. Rev. B* **72**, 113415 (2005).
- [125] N. O. Birge, B. Golding, and W. H. Haemmerle, *Phys. Rev. Lett.* **62**, 195 (1989).
- [126] C. Strunk, M. Henny, C. Schönenberger, G. Neuttiens, and C. V. Haesendonck, *Phys. Rev. Lett.* **81**, 2982 (1998).
- [127] D. Hoadley, P. McConville, and N. O. Birge, *Phys. Rev. B* **60**, 5617 (1999).
- [128] G. Neuttiens, C. Strunk, C. V. Haesendonck, and Y. Bruynseraede, *Phys. Rev. B* **62**, 3905 (2000).
- [129] P. G. Collins, M. S. Fuhrer, and A. Zettl, *Appl. Phys. Lett.* **76**, 894 (2000).
- [130] E. S. Snow, J. P. Novak, M. D. Lay, and F. K. Perkins, *Appl. Phys. Lett.* **85**, 4172 (2004).

- [131] M. Ishigami et al., Appl. Phys. Lett. **88**, 203116 (2006).
- [132] E. Onac, F. Balestro, B. Trauzettel, C. F. J. Lodewijk, and L. P. Kouwenhoven, Phys. Rev. Lett. **96**, 026803 (2006).
- [133] R. Möller, A. Esslinger, and B. Koslowski, Appl. Phys. Lett. **55**, 2360 (1989).
- [134] X. Jiang, M. A. Dubson, and J. C. Garland, Phys. Rev. B **42**, 5427 (1990).
- [135] F. N. Hooge, Physics B **162**, 344 (1990).
- [136] M. Tacano, IEEE Trans. Electr. Dev. **40**, 2060 (1993).
- [137] E. P. Vandamme and L. K. J. Vandamme, IEEE Trans. Electr. Dev. **47**, 2146 (2000).
- [138] C. T. Sah and F. Hielscher, Phys. Rev. Lett. **17**, 956 (1966).
- [139] L. K. J. Vandamme, IEEE Trans. Electr. Dev. **36**, 987 (1989).
- [140] Y. C. C. H. Wong and G. Ruan, J. Appl. Phys. **67**, 312 (1990).
- [141] A. Bora and A. K. Raychaudhuri, J. Appl. Phys. **99**, 113701 (2006).
- [142] J. Scofield, J. MANTESE, and W. WEBB, Phys. Rev. B **32**, 736 (1985).
- [143] R. Huber, *Exporing the electrical conductance of single molecules via mechanically controllable break junctions*, PhD thesis, University Basel, 2008.
- [144] L. Bernard, M. Calame, S. J. van der Molen, J. Liao, and C. Schönenberger, Nature Nanotechnology **18**, 235202 (2007).
- [145] S. Kayashima, K. Takahashi, M. Motoyama, and J. Shirakashi, Journal of Physics: Conference Series Pages , 052022 (2008).
- [146] V. V. Deshpande et al., Nano Lett. **6**, 1092 (2006).
- [147] B. Standley et al., Nano Lett. **8**, 3345 (2008).
- [148] J. Clarke and R. F. Voss, Appl. Phys. Lett. **33**, 24 (1974).
- [149] J. Moreland and J. Ekin, J. Appl. Phys. **58**, 3888 (1985).
- [150] C. Muller, J. van Ruitenbeek, and L. de Jongh, Physica C **191**, 485 (1992).

Appendix A

Special electronic units for the measurement setup

A.1 Four-terminal feedback voltage source

The four-terminal feedback voltage source (FFVS) is essential for a successful EM process to narrow the junction or form a gap. Before we implemented the voltage source, we tried to manually increase the voltage U over the junction of a four-terminal device. With the four-terminal design the junction resistance can be measured exactly. But without the fast adjust in voltage U , EM process is still uncontrollable (see Section 2.2.1). Because EM induced increase of the junction resistance is a fast process ($< \text{ms}$). The feedback voltage control with very fast response allows us to control EM. The circuit diagram and a photo of the FFVS is shown in Figure A.1 and its function is described in Section 2.2.1. The response time can be adjusted by changing the combination of R and C . Here we use $R = 1 \text{ k}\Omega$ and $C = 270 \text{ pF}$ to obtain a response time of $0.27 \mu\text{s}$ as shown in the diagram. To assess R and C , the response time should be at least one magnitude faster than the frequency of the small AC signal for measuring R_j^0 . Otherwise the AC signal could be deformed and result in wrong measurement. The combination, which can invoke the oscillation of the feedback loop, should be avoided either. The FFVS is powered by a house made 24 VDC floating power supply. The input (V_{ref}) limit of the FFVS is 10 V. The maximum voltage output is 17 V and the current can reach maximum 150 mA. The output connector of the feedback voltage allows us to check the feedback input voltage. It should equal to V_{ref} if the FFVS works properly. Otherwise

the LED indicator lamp is off when the feedback voltage does not follow V_{ref} . To contact the sample to the FFVS, the correct sequence is: ground side (-) of voltage output, (-) of feedback input, (+) of feedback input, (+) of voltage output (see Figure 2.6). Not following this sequence could destroy the sample by a high voltage output of the FFVS. Later on it is possible to switch the FFVS to a lower output when contacting the sample. But we still suggest to follow the previously described sequence to contact the sample.

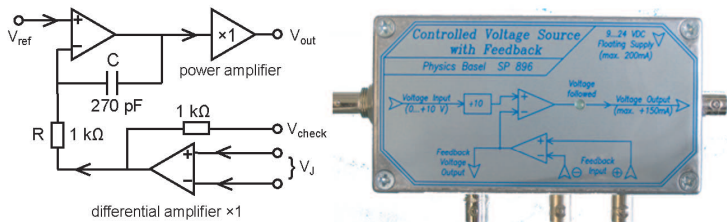


Figure A.1: (a) Circuit diagram shows the working principle of the feedback voltage source. U_J is always equals to V_{ref} regardless of V_{out} . (b) A photo of the four-terminal feedback voltage source used in our setup.

A.2 Ground loop killer

When we build up our setup, we are not always able to plug the computer and all the measurement instruments on same ground. Even when they are plugged on the same electrical outlet, the loop formed by the cables in space can pick up the electromagnetic field in the environment and induce small difference in potential between different grounds. Ground loop are unavoidable in the laboratory. The most picked up noise is the 50 Hz *AC* noise. This ground loop noise can reach as much as 100 mV. Though we want to measure the voltages as small as 1 mV, therefore we have to get rid of the noise by using a ground loop killer (GLK). Our house made GLK is very effective in interrupting the ground loop. The principle of GLK is to separate the ground of the input side from the output side by using differential receiver and driver as shown in Figure A.2. The left side in photo (normally the measurement side) of GLK has the common ground connected to the metal housing. The right side has isolated BNC to separate the ground from housing. The input voltage is read in by the differential inputs of the amplifier. The output signal is the same voltage value in respect to the ground of the amplifier in case of differential receiver, and as

differential outputs in case of differential driver. In our GLK box we have two differential receivers (two lower channels) and two differential drivers (two upper channels) as shown in the photo. The built in selectable gains are very convenient to amplify the usually small signal before it is read in by PC. The GLK itself has high input impedance ($1\text{ M}\Omega$, 15 pF) for the differential drivers and low output impedance ($200\ \Omega$) for the differential receivers.

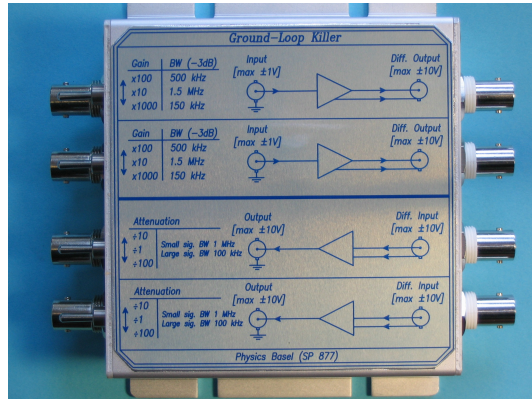


Figure A.2: Photo of the ground loop killer with circuit diagrams on top of the box. The diagrams show the principle of differential receivers (two lower channels) and drivers (two upper channels). The ground of the measurement side (left side) is separated from data acquisition (PC) side (right side).

A.3 Low noise voltage source

The best voltage source to power the sample for the noise measurements is battery, because battery is noiseless. The first setup design to measure noise in nano-contacts is a two terminal measurement powered by battery. The voltage over the sample is adjusted by a potentiometer. The R value of the potentiometer is chosen to be $50\ \Omega$ for the purpose of stable EM (see Section 2.2.1) in nano-contacts. The large R value of potentiometer can result in a rapid voltage increase over the nano-junction in case of EM induced R increase in nano-contacts. The disadvantage of this setup is that much more current flows through the potentiometer than through sample. The large current even flows when the sample is not measured but connected. The potentiometer is getting hot after several measurements. To avoid all

these shortcoming, we developed a low noise voltage source (LNVS). Its quite current is only 2 mA. A sudden increase of the output current may cause a slight ($< 20\%$) voltage decrease. But it goes back to the set value within 40 ms. The LNVS is powered by a battery (9 V 500 mAh) to avoid ground loops. The noise generated in the amplifiers and other electronics is reduced by several steps of low pass filter (< 10 Hz). The schematic of the power source is shown in Figure A.3a. The noise level of the voltage source is as low as $1.5 \text{ pV}/\sqrt{\text{Hz}}$ at 100 kHz. Its output impedance is less than 5Ω at a frequency lower than 1 Hz as shown in Figure A.3b. The voltage output can

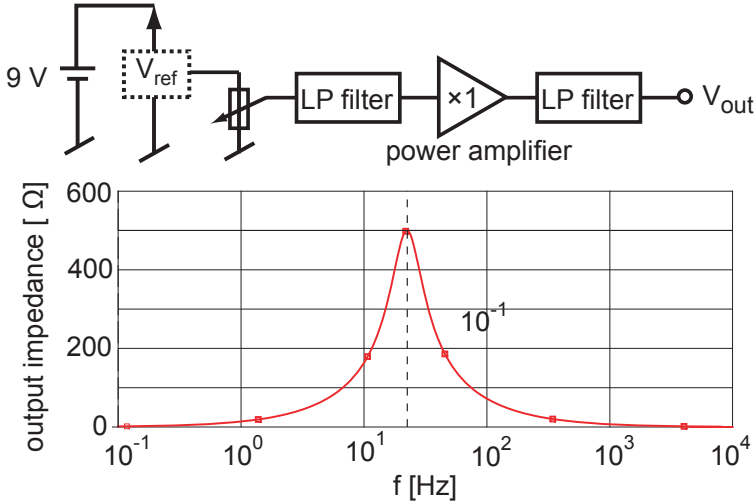


Figure A.3: (a) Diagram of low noise voltage source. A reference voltage unit sets a constant voltage regardless of the change of battery voltage. The output voltage can be set by the potentiometer. (b) Frequency response of the output impedance of LNVS .

be adjusted between 0 and 2.5 V by a potentiometer, the maximum current is 3 mA. A multimeter can be connected to a separate output to check the voltage output of LNVS. A battery powered multimeter is much better than a 220 ACV powered multimeter, because the later introduces large noise at voltage output. Therefore we use four-terminal samples, which allows us to exactly measure the voltage drop over the junction without knowing the voltage output of LNVS (see Section 2.16).

Appendix B

Mechanical controllable break junction

Break-junction was first introduced by Moreland and Ekin [149] in 1985 to study the tunneling characteristics of superconductors. Later on several extensions and modifications were made to this concept by Muller et al. [150; 96], who introduced the name MCBJ. The principle of MCBJ is illustrated in Figure B.1. The sample is a thin freestanding metal bridge with

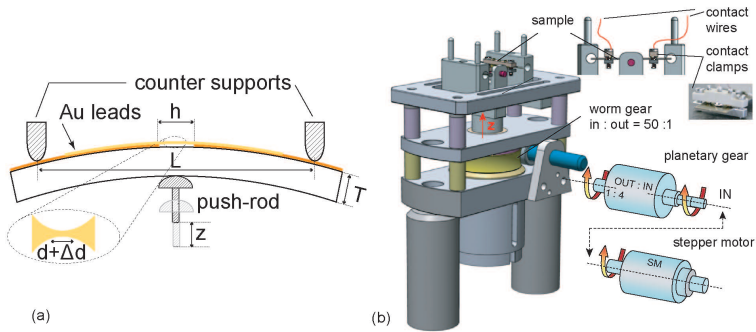


Figure B.1: (a) Principle of operation of a MCBJ. The displacement z of push rod introduces an elongation Δd of middle constriction. Meanwhile the constriction is thinned finally breaks. Δd can be tuned by z through geometrical attenuation factor. (b) The bending apparatus with mechanically induced attenuation factor.

a central lateral constriction fabricated on the top of a flexible substrate.

The sample is then mounted in a three point bending system. By pushing a rod versus the middle bottom of the substrate, the sample is bent up. This deformation exerts a lateral force on the sample and stretches the freestanding bridge. During the stretch the constriction is elongated and thinned till broken. By relaxing the substrate the bridge can be closed again. The cross-section of the constriction can be tuned by moving the rod up or down. The sample is EBL fabricated followed by Au deposition, the gold constriction in the middle can be prolonged more than $1 \mu\text{m}$ without breaking into apart. The three point bending system has the advantage to insert an geometrical attenuation ration between the push rod moving distance and the bridge elongation. For the ideal case of an elastically homogeneous bending beam with supported ends, the geometrical attenuation factor is given by [102]:

$$a_g = \frac{\Delta h}{\Delta z} = \frac{6Th}{L^2}, \quad (\text{B.1})$$

where T is the sample thickness, h the length of the freestanding bridge, and L the distance between the two counter supports. Based on our setup the distance between counter supports is $L \approx 20 \text{ mm}$, the thickness of the substrate $T = 0.3 \text{ mm}$ and the length of freestanding bridge $h \approx 0.5 \mu\text{m}$, we get $a_g \approx 2 \cdot 10^{-6}$. Furthermore the vertical displacement of the push rod is driven by a stepper motor (Phythron GLD) through a coupling gear, which consists a planetary gear (reduction 1:4) and a worm gear (reduction 1:50). The smallest movement from one sub-step turning of the motor induces a rod movement of 3.125 nm [143]. After the geometrical attenuation factor a_g the smallest elongation of constriction is 3.125 pm . The motor can be adjusted in speed between $1.56 - 31.2 \mu\text{m/s}$ by a computer. At large constriction we use high speed to get the constriction thinned fast. At point-contact with only few atoms we use the smallest speed to get the point-contact thinned continuously and stable.

Appendix C

Complementary Experiments

C.1 Electromigration in scanning electron microscope (SEM)

We observed Em by SEM (Philips XL 30 FEG) in order to better understand the EM process. EM was carried out in the vacuum chamber ($1 \times 10^{-6} \text{ mbar}$) of the SEM. The change of the junction is in situ imaged by SEM and recorded into a video file. Nano-wires around 200 nm in length and 150 nm in width are fabricated on Si substrate as described in Section 2.1. To contact the sample inside SEM we first bond the sample on a chip carrier. The chip hold has pin holes to contact the connecting cables. Those cables are then connected to our measurement setup outside the SEM through an adapter on the wall of the SEM vacuum chamber with maximum four connectors. The chip carrier is then mounted on the standard sample holder of the SEM. A very good electrical contact between substrate and SEM sample holder is important to get a stable SEM image. EM can be started in two-terminal junctions but carried out smoothly on four-terminal samples. In two-terminal EM we are able to image the EM in the junction with very good quality. We observed that the wires are immediately melted by Joule heating as soon as EM starts in the wire. This suggests that the moment immediately after the onset of EM is critical. This lead us to design the feedback controlled EM. With four-terminal feedback controlled EM (see Section 2.2) the SEM imaging is more disturbed by the feedback voltage source and the PC in the setup. The reason can be the ground loops are built between the SEM and our setup. Furthermore the feedback controlled

four-terminal EM form slits smaller than 30 nm, which are at the edge of the resolution and difficult to image by SEM Philips. The videos of EM in SEM can be found on Marc\ MingWu \ EMinSEM.

C.2 Noise during electromigration

When measuring the $1/f$ noise in electromigrated junctions, we observe that the noise is several orders of magnitudes larger in the junction when EM is active. In Figure C.1 such a noise measurement is shown. The black dots are the noise measured before EM occurs in the junction. The noise magnitude S_V/V^2 stays same at different bias voltage. The red dots are measured during EM but the change of junction resistance R is slow. If the junction resistance does not change much during the noise measurement, we can take the junction resistance before noise measurement as R_J in Figure C.1. Furthermore the noise magnitude is too large to be measured with our setup, when EM is very active and induces large increase of R in the junction. After the bias is reduced to 0.15 V and EM is stopped in the junction, the green dots are measured. A large difference in noise magnitude S_V/V^2 is observed between red (EM presents) and green (no EM) dots. This indicates that EM induces extra noise in the system. This extra noise is mainly caused by the slow diffusion of Au atoms and defects in the junction under the EM wind force [141]. The noise S_V/V^2 (green dots) measured at low bias (~ 0.15 V) scales with R as $\propto R^{1.5}$ as discussed for the junctions in ballistic regime (see Section 3.3.2).

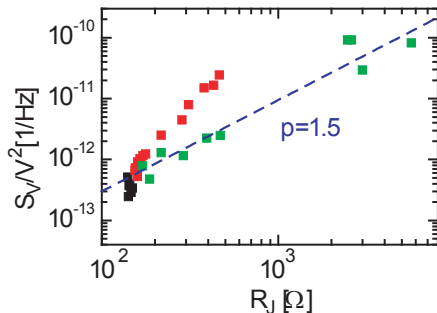


Figure C.1: $1/f$ noise magnitude S_V/V^2 measured in the electromigrated junction as function of the junction resistance. Red dots are measured when EM is active. Green and black dots are measured when EM is stopped. The dashed blue line is a guide line with $S_V/V^2 \propto R^{1.5}$.

Appendix D

Parameters during electromigration

In the table we list the measured data of critical current density j_c and critical temperature T_c at the onset of EM in 21 samples. The dimensions and types of the samples are listed as well. Sample types A = straight wire type and B = bow tie type junction. The histogram shown in Figure 3.6 is based on the values in the table.

Samples	j_c [10^8 A/cm 2]	T_c [K]	width [nm]	thickness [nm]	type
11A1	1.91	427	100	45	A
11A2	2.22	457	100	45	A
11B1	2.42	422	100	45	A
11B2	2.49	409	100	45	A
11C1	2.67	402	100	45	A
11C2	2.96	415	100	45	A
11F1	2.69	411	170	45	A
12F2	2.50	448	80	45	A
15B1	15.45	498	110	20	B
15D1	15.50	473	100	20	B
15E1	13.64	488	110	20	B
16B1	11.92	431	130	20	B
16C2	13.63	453	120	20	B
1A1	4.75	462	100	40	B
1A2	4.71	377	100	40	B

Samples	j_c [10^8 A/cm 2]	T_c [K]	width [nm]	thickness [nm]	type
4A1	6.93	419	100	40	B
4A2	5.84	462	100	40	B
8A1	5.85	435	90	40	B
8A2	5.94	407	70	40	B
14E1	4.60	449	100	45	B

Appendix E

Histogram in log scale

In Figure 3.16 (Section 3.3.3) we presented measured Hooge's parameter α as histogram in logarithm scale with evenly distributed bin size. Here we explain the method to make the graph. First we take the $\log\alpha$ and make a histogram with evenly distributed bin size. In the bin data file of this histogram, the bin start and end points value Bin_n is calculated back to linear scale with 10^{Bin_n} . It is then plotted new with correct counts from bin data file in a logarithm plot. If we do not do the transformation described above, only change the α axis to logarithm scale, the histogram will have an uneven bin width. An example is shown in the following table.

α	$\log(\alpha)$		bin	counts Y	10^{bin} X
1.5856E-5	-4.79981		-4.75	2	1.77828E-5
1.63305E-5	-4.787		-4.65	0	2.23872E-5
3.08955E-5	-4.51011		-4.55	2	2.81838E-5
...	...		-4.45	3	3.54813E-5
4.63432E-5	-4.33401		-4.35	3	4.46684E-5
4.68851E-5	-4.32897	\Rightarrow	-4.25	2	5.62341E-5
5.86063E-5	-4.23206		-4.15	4	7.07946E-5
...	...		-4.05	1	8.91251E-5
1.1673E-4	-3.93282		-3.95	4	1.12202E-4
1.17213E-4	-3.93103		-3.85	1	1.41254E-4
1.29167E-4	-3.88885		-3.75	1	1.77828E-4

Appendix **E**

Publication List

Articles

- *Is aluminum a suitable buffer layer for carbon nanotube growth?*
T. de los Arcos, Z.M. Wu, P Oelhafen, Chemical Physics Letters, **380**, 419, (2003).
- *Feedback controlled electromigration in four-terminal nano-junctions.*
Zheng Ming Wu, M. Steinacher, R. Huber, M. Calame, S. J. van der Molen and C. Schönenberger, Appl. Phys. Lett. **91**, 053118 (2007).
- *Scaling of $1/f$ noise in tunable break-junctions* ZhengMing Wu, Song-Mei Wu, S. Oberholzer, M. Steinacher, M. Calame and C. Schönenberger, submitted.

Poster contributions

- *Break Junctions in liquid for molecular electronics.*
R. Huber, Z. M. Wu, M. T. González, H. Breitenstein, P. Reimann, M. Calame and C. Schönenberger.
Poster at the NCCR Nano meeting, Gwatt, October 6th - 7th, 2005
- *Feedback controlled electromigration in four-terminal nano-junctions.*
Zheng Ming Wu, M. Steinacher, R. Huber, M. Calame, S. J. van der Molen and C. Schönenberger.
Poster at the NCCR Nano meeting, Basel, April 25th, 2007.
- *Feedback controlled electromigration in gold and cobalt nano-junctions.*
Zheng Ming Wu, M. Steinacher, R. Huber, M. Calame, S. J. van der Molen and C. Schönenberger.
Poster at the NCCR Nano meeting, Basel, April 12th, 2008.
- *Feedback controlled electromigration in gold and cobalt nano-junctions.*
Zheng Ming Wu, M. Steinacher, R. Huber, M. Calame, S. J. van der Molen and C. Schönenberger.
Poster at the i-net Basel Nano, Basel, June 24th, 2008.